Evaluating Predictability in the Community Earth System Model in Response to the Eruption of Mount Pinatubo

A Dissertation Presented for the
Doctor of Philosophy
Degree
The University of Tennessee, Knoxville

Abigail Laurel Gaddis
August 2013

Acknowledgements

I am indebted to my co-advisors, Chris Cox and John Drake, for their guidance and motivation for finishing this work. In particular, am deeply grateful to John Drake for his contributions to my understanding of climate modeling and atmospheric science, and to Chris Cox for his financial support. Without the guidance, expertise, and support of Kate Evans, the completion of this dissertation would not have been possible. I owe her many bottles of port. I wish to thank Joshua Fu for providing advice when things went wrong, as well as for serving on my committee. I am grateful to Greg Peterson for teaching me C++ and agreeing to serve on my committee. I would also like to thank my collaborators in the Climate Change Science Institute at Oak Ridge National Laboratory. I appreciate my fellow students at the University of Tennessee, particularly Lauren Raup-Plummer, Jennifer Ribbeck, and Melissa Allen, for being friends as well as colleagues, and for listening to me whine. Thank you to my family whose support has carried me through. Lastly, I am grateful to Michael Pickering for putting up with me during this process and for buying dinner when things got out of hand.

Abstract

A central goal of climate research is to determine the perceptible effects of climate change on humans; in other words, the regional and decadal scale effects of carbon dioxide forcing. Identifying the most pronounced and long-lasting responses of climate variables to forcing is important for decadal prediction since forcing terms are a source of predictability on those time scales. Powerful volcanic eruptions provide a transient forcing on the climate system, creating a test bed for climate models. In this study, the Mount Pinatubo eruption is simulated in the Community Earth System Model, CESM1.0, for three model configurations: fully coupled T85 ($\sim 1^{o}$), land -atmosphere T85, and land-atmosphere T341 ($\sim 1/3^{o}$). Ensembles of simulations with and without volcanic aerosols are compared to determine the relative sensitivity and duration of responses. The predictability is quantified using a unitless signal to noise ratio. Results from all three configurations are compared with observations to evaluate model skill. Stratospheric humidity increases predictably, with spatial analysis showing the response is centered over the tropical tropopause. The corresponding geographical pattern of the tropopause temperature increase lends credibility to attribution of the signal to tropopause flux rather than direct injection of water vapor into the stratosphere. The stratospheric water vapor response to the eruption is long-lived in comparison to other signals, providing a source of long-term predictability in the stratosphere. Novel predictable signals are identified, including a decrease in monoterpene and other volatile organic compounds, an increase in land snow depth and extent, and a decrease in lake, soil, and snow heat content. Additionally, in the fully coupled model the standard deviation of the forced ensemble is reduced 8-14% as compared to the unforced ensemble standard deviation. This implies that the model responds to the forcing in similar ways regardless of initial climate state. The Northern Hemisphere winter warming response improves in spatial distribution and strength both at higher resolution and in the fully coupled model. These results motivate the continued drive to higher resolutions and increased model complexity.

Table of Contents

List of Tables

List of Figures

Chapter 1

INTRODUCTION

1.1 Earth's Energy Budget

The Earth's climate is determined by the amount and distribution of incoming solar energy. The total incident shortwave radiation establishes the atmosphere's total accessible energy, which is then reflected and absorbed by the atmosphere, clouds, and land surface (Kiehl and Trenberth 1997). The light that reaches earth's surface is re-radiated at longer wavelengths as heat, such that the earth acts as a blackbody at 290K. Clouds and other atmospheric processes again absorb and reflect this heat so that some of it is trapped near the Earth's surface, and a portion of the outgoing longwave radiation finally exits the system to space. Figure 1-1 shows the distribution of received solar radiation in the system along with estimates of the energy involved in each process in W/m^2.

A change to the radiation balance between the different climate components is called a radiative forcing. Some examples of radiative forcing include the presence of aerosols and greenhouse gases in the atmosphere, changes to the albedo of the earth's surface, and solar fluctuations due to the 11 year solar cycle (Kiehl and Trenberth 1997). For example, land use changes modify the reflectivity of the land surface as well as removing vegetation that absorbs and sequesters CO_2. These anthropogenic effects modify the local radiation balance.

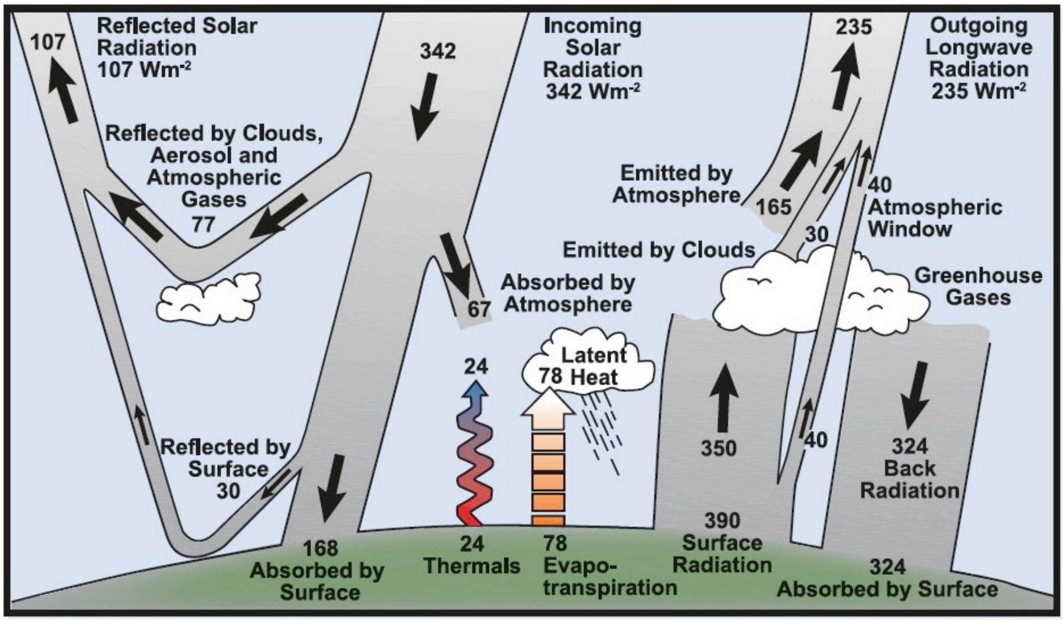

Figure 1-1. Schematic diagram of Earth's global average annual energy budget and distribution (Kiehl and Trenberth 1997).

1.2 Greenhouse Gases and Climate

Greenhouse gases absorb and emit longwave radiation while reflecting shortwave radiation. When large amounts of these types of chemicals are distributed in the atmosphere, their optical properties create a radiative forcing on Earth's climate. This is because they allow incoming light to pass through, but trap the re-radiated heat close to the Earth's surface, like the glass in a greenhouse. Increasing the amount of greenhouse gases causes an increase in global surface temperatures as well as a corresponding decrease in stratospheric temperatures. Further, chemically stable greenhouse gases, known as long-lived greenhouse gases, reside for long periods in the atmosphere after they are emitted, exacerbating this effect (IPCC 2007).

Carbon dioxide is the most important of the long-lived greenhouse gases because of the high quantity and rate at which human activities emit it. In particular, the combustion of fossil fuels has been a large source of carbon dioxide since the industrial era. Currently, anthropogenic sources of CO_2 have outnumbered natural CO_2 sinks, resulting in increasing CO_2 concentrations in the atmosphere and ocean. This perturbation to Earth's climate system by anthropogenic carbon dioxide emissions is known as climate change. Due to the stable nature of carbon dioxide in the atmosphere and the slow response of climate parameters such as oceanic heat transfer, it is predicted that with emissions stable at year 2000 levels, the global temperature would continue to increase by $0.1^{o}C$ per decade (IPCC 2007). The response time scale of the upper ocean to forcing is years to decades, while deeper ocean and ice sheet responses range from hundreds to thousands of years. The concept of "committed" change is used to describe these long-term future effects of previous radiative forcing. The study of climate change and its effects on humans has become important for policymakers and stakeholders worldwide.

1.3 Climate Modeling

Since climate experiments are impossible, global climate models have been developed to better understand the climate system and its response to forcings. As computational capabilities and scientific understanding advance, models have become more sophisticated. Climate models developed in the 1960s considered basic physics equations governing fluid dynamics influenced by the earth's rotation, gravity, pressure and temperature gradients, and frictional forces. Additionally, these models considered thermodynamic influences on energy exchange such as radiation, convection, and the transfer of energy and momentum to the planet's surface. Models eventually began to comprise more land and ocean processes. Finally, biophysical processes and chemical interactions in land, ocean, and atmosphere are represented (Sellers, Dickinson et al. 1997; IPCC 2007; Flato 2011). Evaluating the performance of these models with observable phenomena in order to quantify model uncertainty is of growing importance (IPCC 2007).

1.4 Volcanic Eruptions and Climate

1.4.1 Atmospheric Effects of Aerosols

Aerosols in the atmosphere generate a radiative forcing on the climate that has two major components, direct and indirect. Direct effects of aerosols include influence on the radiation balance by the scattering of solar radiation; for most types of aerosols, this results in the cooling of the troposphere. Additionally, aerosols serve as nuclei upon which clouds and ice can condense, resulting in indirect effects on climate. The first indirect effect refers to the impact of aerosols on cloud microphysical processes, while the second indirect effect denotes their involvement in cloud amount. There is also a semi-direct effect, in which the heating by aerosol particles due to absorption of solar radiation results in a decrease of cloud amount (IPCC 2007).

The largest eruptions of volcanoes initiate a global impulse to the Earth's climate system due to the injection of volcanic aerosols high into the atmosphere (McCormick, Thomason et al. 1995; Hansen, Sato et al. 1997; Robock 2000; IPCC 2007). Volcanic aerosols are comprised mostly of sulfur dioxide and particulate matter. The sulfur dioxide then reacts with water and hydroxyl radicals to form sulfates and sulfuric acid in 2-10 days following the eruption. The particulate matter settles out of the atmospheric column in the first few months after the eruption, so that the characteristics of sulfates dominate the plume (Rampino and Self 1984). Sulfates in the troposphere serve as sites for cloud nucleation, increasing the reflectivity of the clouds by increasing the number of cloud droplets. Sulfates in the stratosphere serve as sites for heterogeneous chemical reactions (Robock 2000). The direct and indirect effects of these aerosols in the troposphere and, especially, stratosphere, generate a large perturbation to atmospheric dynamics and chemistry (Rampino and Self 1984).

For large eruptions, the forcing has been observed to leave a distinct signature in the vertical temperature response, including warming in the stratosphere and cooling in the troposphere. This is due to the optical properties of the aerosols, which are about the same size as the wavelength of visible light, and have a high albedo (Lacis, Hansen et al.

1992). Some sunlight is scattered back into space, resulting in cooler tropospheric temperatures, while other radiation is absorbed, leaving the stratosphere warmer. Additionally, much solar radiation is scattered but makes it through the aerosol layer, resulting in a higher proportion of diffuse light on the surface (Rampino and Self 1984; Hansen, Sato et al. 1997; Robock 2000).

The response of the Earth's climate system to this transient forcing can be measured instrumentally and replicated in models (McCormick, Thomason et al. 1995). Therefore, these events serve as benchmarks for assessing aspects of climate models. For instance, many studies evaluate the predictive skill of global climate models by comparing the model response to observations of the actual response (Hansen, Lacis et al. 1992; Rozanov, Schlesinger et al. 2002; Boer, Stowasser et al. 2007; Bender, Ekman et al. 2010). Volcanic eruptions remain one of the few strong climate forcing phenomena available for model verification (Hurrell, Meehl et al. 2009).

1.4.2 Mount Pinatubo Eruption Observed Effects

The June 15, 1991 eruption of Mt. Pinatubo in the Philippines is specifically of interest for volcanic radiative forcing studies since it was the largest aerosol perturbation to the stratosphere in the twentieth century (McCormick, Thomason et al. 1995). Other volcanic eruptions produced statistically significant effects on global mean temperature, for instance at about the 1 ½ σ level for El Chichon and Agung. However, the eruption of Mount Pinatubo created a 3 σ level disturbance (Hansen, Lacis et al. 1992). The estimated peak aerosol mass loading to the stratosphere was 30 Tg, and the plume reached an altitude of more than 30km (McCormick, Thomason et al. 1995).

Furthermore, this eruption is important as the most intensely observed eruption on record since it occurred after the development of many modern climate data collection technologies. Various satellite data collection systems such as ISAMS (Improved Stratospheric and Mesospheric Sounder) and SAGE II (Stratospheric Aerosol and Gas Experiment) provided information about aerosol properties of the eruption, as well as observations of the response to the eruption (Grainger, Lambert et al. 1993; Sato, Hansen et al. 1993; McCormick, Thomason et al. 1995). Due to these detailed records, many measurements are available to use as a standard for climate models.

The stratospheric volcanic sulfates increased the planetary albedo overall due to the optical properties of the aerosol. This caused stratospheric temperatures to initially warm, but after the first two years, chemical reactions depleting stratospheric ozone led to cooling of the stratosphere. Additionally, the expected global cooling of surface air temperature was observed, an anomaly of about -0.4^{o} C (Hansen, Lacis et al. 1992; McCormick, Thomason et al. 1995). These temperature changes generated secondary responses to the eruption. For example, the equator-to-pole gradient in temperature also increased (McCormick, Thomason et al. 1995). Changes in temperature gradients affect winds, by the thermal wind equation. Therefore, the stratospheric polar jets were amplified by the temperature gradient change. The polar vortex isolates low pressure around the polar region, so that modifications to it change the distribution of high and low pressure cells in the region. These changes modify the Arctic Oscillation (Stenchikov 2006), leading to Northern Hemisphere surface winter warming anomalies in the first two winters following the eruption (Robock and Mao 1992). Ozone chemistry (Brasseur and Granier 1992; McCormick, Thomason et al. 1995) and vegetation responses (Gu, Baldocchi et al. 2003; Telford, Lathiere et al. 2010) related to the radiation and temperature changes were also recorded. The complex dynamical, chemical, and biological effects of the eruption of Mount Pinatubo generate a rich test bed for global earth system models.

1.5 Predictability

The Earth's climate is a dynamical system that is deterministic, but also demonstrates sensitive dependence on initial conditions. The internal stochastic component of such a system generates increasing differences between initially similar states as they evolve. Therefore, if the state of the climate is not exactly known, predictions of its future state become less accurate over time (Lorenz 1963; Lorenz 1969).

Predictability measures the rate at which two initially close system states separate with time due to internal chaos. Additionally, predictability may be characterized as the rate of separation of a model state from the true state, in other words, the rate of error growth (Lorenz 1969; Boer 2004). In climate modeling, predictability loss is comprised of error growth due to both chaotic variation of the system itself and inaccuracies in replicating the real system (Boer 2004; Farrell and Ioannou 2005; Hurrell, Meehl et al. 2009). Since variability in a system may be composed of both chaotic and deterministic influences, potential predictability is defined as the fraction of long-term variability that can be distinguished from the internal "noise" of the system (Hansen, Sato et al. 1997; Boer 2004). Potential predictability is often discussed in relation to climate oscillations such as the El Niño – Southern Oscillation (ENSO) (Von Storch 2008).

Predictability studies may be further classified by the presence or absence of forcing on the system studied. Predictability studies of the first kind, such as weather forecasting, seek to determine a short-term future state of the system under the assumption of constant forcing. Predictability studies of the second kind, such as climate prediction, attempt to project the future system state under changing forcing conditions (Von Storch 2008).

1.6 Objectives

The motivation of this work is to analyze the predictability of the Earth's climate system in response to volcanic forcing through simulations using the Community Earth System Model. This analysis is undertaken in order to find new predictable responses, especially on the decadal time scale, as well as to identify the spatial distribution of the predictability of these responses. A further goal is to evaluate the skill of the model in reproducing known responses to the eruption.

1.6.1 Research Hypothesis 1

Ranking the signal to noise ratios shows the relative intensity of the responses, useful for decadal prediction. Further, it provides an exploratory method to identify and attribute unexpected model responses to generate novel science.

1.6.2 Research Hypothesis 2

The ensemble of fully coupled climate simulations without volcanic forcing will have a higher standard deviation about the ensemble mean than the forced ensemble standard deviation. The climate state is constrained by the transient volcanic forcing on the system, so that natural variability is damped by the forcing.

1.6.3 Research Hypothesis 3

The El Niño – Southern Oscillation (ENSO) responds predictably to the Mt. Pinatubo eruption in the Community Earth System Model (CESM). Perturbations to the sea surface temperatures create conditions favorable for ENSO.

1.6.4 Research Hypothesis 4

Higher spatial resolution in CESM improves the predictive capabilities of the model as well as identifying regions of predictability, as shown by spatial maps of the signal to noise ratio and empirical orthogonal functions.

Chapter 2

ADDITIONAL BACKGROUND

2.1 Hypothesis 1

H1: *Ranking the signal to noise ratios shows the relative intensity of the responses, useful for decadal prediction. Further, it provides an exploratory method to identify and attribute unexpected model responses to generate novel science.*

Various methods exist for quantifying the predictability of a system. Many predictability studies seek to differentiate a predictable response or pattern from chaotic background noise (DelSole and Tippett 2007; Deremble, D'Andrea et al. 2009). More traditional definitions of the signal to noise ratio filter variations by frequency to extract a signal from background chaotic behavior in the system (Lucarini and Sarno 2011). Other methods use the variance of forced and unforced ensembles of simulations as a signal to noise ratio (Boer 2004; Meehl, Goddard et al. 2009; Koenigk, Beatty et al. 2012; Frumkin and Misra 2013). The version of the signal to noise ratio chosen for this analysis depicts the signal as the difference between ensemble means, and the noise as the spread of the control ensemble (Von Storch 2008). This definition is selected due to its consideration of the differences between the two ensemble means, and for the intuitive statistical interpretation of the resulting ratio. For instance, a signal to noise ratio of three implies that the response to the forcing is three times outside the spread of the control ensemble, 3σ. This allows for easy interpretation of a "predictable response." Further literature review and details of the framework for predictability analysis are described in the first paper, Chapter 3. The results of ranking the signal to noise ratios are described in each of the three papers in Chapters 3, 4, and 5.

2.2 Hypothesis 2

H2: *The ensemble of fully coupled climate simulations without volcanic forcing will have a higher standard deviation about the ensemble mean than the forced ensemble standard deviation. The climate state is constrained by the transient volcanic forcing on the system, so that natural variability is damped by the forcing.*

Previous studies find that the response to a climate forcing is generally unaffected by the type or distribution of the forcing. For example, Hansen et al. find that for various equal radiative forcings applied to a model, the magnitude of the forcing is an accurate predictor of climate response. However, they note some exceptions to this rule, including forcing by tropospheric aerosols and changes in ozone (Hansen, Sato et al. 1997). For most forcings, Boer argues that the geographical response to forcing depends more on the spatial pattern of feedbacks rather than the distribution of the forcing itself (Boer and Yu 2003; Boer and Yu 2003). This is corroborated by the finding that homogeneous forcings may result in non-homogeneous spatial response patterns (Von Storch 2008). Therefore, internal dynamics and feedbacks within the climate system are more important than the way the system is forced.

In this study, if the response to the volcanic aerosols in the model is similar regardless of the initial model state, the response to the eruption dominates the natural variability. The implication is that the climate state of unforced systems is more uncertain; forced systems are more predictable since they must respond to the forcing according to the internal dynamics of the climate system. This would reinforce that the signal to noise ratio should use the unforced variability as the measure of the noise in the system. This way the signal to noise ratio measures if a response is predictably different from the ensemble of possible natural states of the system. The findings related to this hypothesis are discussed in the second paper in Chapter 4.

2.3 Hypothesis 3

H3: *The El Niño – Southern Oscillation (ENSO) responds predictably to the Mt. Pinatubo eruption in the Community Earth System Model (CESM). Perturbations to the sea surface temperatures create conditions favorable for ENSO.*

2.3.1 El Niño – Southern Oscillation

The natural variability of the dynamical climate system generates preferred oscillation modes known as teleconnections. These quasi-periodic anomaly patterns may encompass large geographical areas and oscillate at various frequencies. They are characterized by a defined geographical index and by the phase and amplitude of the oscillation. Since teleconnections affect annual and regional weather strongly, the impact of radiative forcings on teleconnections is important. Examples of teleconnections are the North Atlantic Oscillation, the Northern Annular Mode, and the Pacific Decadal Oscillation. The El Niño – Southern Oscillation is an equatorial Pacific fluctuation in sea surface temperatures of irregular frequency. The positive phase of ENSO is known as "El Niño, while the negative phase is called "La Niña." One commonly used index is the Southern Ocean Index (SOI): the surface air pressure anomaly between Tahiti and Darwin, Australia. This teleconnection causes global climate anomalies, including regional climate anomalies over the United States and South America with anomalies extending as far as Europe and Asia (Latif, Anderson et al. 1998). A warm, positive phase of ENSO was beginning when the Mt. Pinatubo eruption occurred in June 1991 (Robock 2000).

2.3.2 ENSO and volcanic eruptions

The connection between ENSO and volcanic eruptions is debated. The statistical collinearity between past ENSO events and volcanic eruptions has been noted (Santer, Wigley et al. 2001). However, it is possible to predict the ENSO state without knowledge of volcanic forcing. It was recently found that larger volcanic eruptions create ENSO-favorable conditions, so that a positive phase is more statistically probable (Emile-Geay, Seager et al. 2008). The second paper in Chapter 4 highlights the results of statistical analysis to extract the effect of the eruption on the ENSO state in the model.

2.4 Hypothesis 4

H4: *Higher spatial resolution in CESM improves the predictive capabilities of the model as well as identifying regions of predictability, as shown by spatial maps of the signal to noise ratio and empirical orthogonal functions.*

2.4.1 Resolution and climate modeling

Increasing resolution in climate models should improve the accuracy of the simulation in several ways. For any numerical method, increasing the number of grid points in a numerical solution increases the accuracy of the solution approximation. Secondly, parameterizations of sub grid-scale processes can be replaced with physical equations as the spatial grid size approaches the scale of the climate process. Additionally, small-scale features can be represented more precisely, for instance, increased definition of local topology represents local weather effects more accurately. However, the degree to which increasing resolution is beneficial depends on the process being modeled as well as the method of discretization. Additionally, increasing resolution increases computational demand, but again, the amount of this computational cost varies with the numerical method.

2.4.1.1 Numerical accuracy

The dynamics components of climate models seek to solve partial differential equations (PDEs) that represent resolved processes in Earth's climate system. Spatial numerical techniques for solving PDEs include finite difference methods, finite element methods, finite volume methods, and spectral methods. Additionally, hybrid methods like the spectral element method have been used. For many of the numerical methods used in climate modeling, as the spatial resolution increases, the numerical solution approaches the analytical solution. Therefore, increasing resolution should bring increased fidelity to the representation of these processes. In the same way, addressing the temporal discretization with more accurate methods is desirable.

2.4.1.2 Resolving small scale physics

The current solution for implementing subgrid-scale phenomena in climate models is to parameterize them in terms of grid-scale variables. Synoptic weather systems, tropical instability waves, and cloud microphysics are examples of phenomena currently parameterized in global climate models due to resolution limitations (Stowasser, Hamilton et al. 2006; Hurrell, Meehl et al. 2009). The best solution is to resolve the dynamics of these processes explicitly by decreasing the grid cell size of the model.

For example, a study of precipitation over the United States using the CCM3 model found incremental improvements to the representation of precipitation, from both a seasonal mean and a daily statistics standpoint, as resolution increased (Iorio 2004). Similarly, Collier and Zhang find that higher resolution in CAM3 improves the representation of tropospheric moisture convection, although they note that even at their higher resolution it is still relatively poorly simulated (Collier 2007). Pope et al. find that increased resolution does improve the capability of the model to represent dynamics without new parameterization schemes. They note that certain variables did not perform as well, and this is due to the need for new parameterizations for variables that still are not captured at the new resolution (Pope and Stratton 2002). Some cloud microphysics variables involve processes in the millimeter range, and resolving these fully in a global model could have very high computational cost. Although increasing the resolution of the model is the best solution, this approach is limited by available computing power (Hurrell, Meehl et al. 2009). Other studies find improvements with increased resolution to Atlantic storm tracks (Caron, Jones et al. 2011), precipitation and wind speed (Varghese, Langmann et al. 2011), and winds and eddy fluxes (Boville 1991).

2.4.1.3 Depicting regional climate

In addition to improving the accuracy of the model, increasing resolution allows models to more accurately depict regional climate. The local topography affects local wind and storm track patterns, for instance. Regional realism is important for making climate change impacts relevant to policymakers, engineers, and the public. For instance, regional representation of flooding frequencies in a future climate change scenarios can inform engineering design decisions. To tell people what may happen and what they can do about it is the key motivation for climate modeling. Further, many climate processes involve interactions between dynamics on different spatial and temporal scales (Hurrell, Meehl et al. 2009). Therefore, improvements to sub-scale process representation with higher resolution is expected to additionally improve the dynamical representation of larger-scale processes.

2.4.2 Empirical Orthogonal Functions

Empirical orthogonal functions (EOFs) are a way to quantify the variance of a data set and isolate its modes of oscillation in space and time (Bretherton 1992; Borzelli 1999; Hannachi 2007). This statistical method projects the data onto uncorrelated spatial vectors representing the direction of most variation, with the first empirical orthogonal function comprising the largest percentage of variation, the second the second largest, and so on. Each of the spatial patterns has a corresponding time series, or principal component, uncorrelated to all other principal components.

Following the basic method of Hannachi (2007), given a rectangular matrix, A, the singular value decomposition theorem states that A may be expressed as

$$A_{mxn} = U_{mxm}\Sigma_{mxn}V_{nxn}^{H}$$

where H indicates the conjugate transpose and the subscripts denote the size of the matrices. U and V are unitary and orthogonal, such that

$$U^{H}U = I_{mxm}$$

and

$$V^{H}V = I_{nxn}$$

The m columns of U are the eigenvectors of AA^{H}, while the n columns of V are the eigenvectors of $A^{H}A$. Σ_{mxn} is a rectangular diagonal matrix of the same size as A. It is composed of diagonal entries that correspond to the square roots of the non-zero eigenvalues of both AA^{H} and $A^{H}A$. The amount of variance in the data captured by each pattern may be inferred from these values.

In climate studies, empirical orthogonal function analysis is often used to examine changing spatial modes of variability, especially in teleconnections such as the El Niño-Southern Oscillation (ENSO). However, physical interpretation is complicated by the fact that real processes are not necessarily orthogonal and that relationships between the temporal and spatial modes are unclear (Borzelli 1999; Schlink 2009). Furthermore, the modes are ranked by their statistical significance, which may not be related to subjective importance of the phenomenon of interest (Borzelli 1999).

The diagonal elements of Σ_{mxn} are also known as the singular values of A, while the m columns of U and the n columns of V are, respectively, the left and right singular vectors of the data matrix A. The right singular vectors are known in atmospheric sciences as the empirical orthogonal functions, which are spatial vectors of the same size as the number of grid points, n. The left singular vectors are the time series of length m of the associated EOFs.

The results of the spatial analysis of the predictability of variables are found throughout the three papers in Chapters 3, 4, and 5. The third paper, Chapter 5, particularly highlights the role of resolution in model predictability and skill.

Chapter 3

PAPER 1: EVALUATING CLIMATE PREDICTABILITY SIGNALS IN RESPONSE TO FORCING: MOUNT PINATUBO AS A CASE STUDY

A version of this chapter will be submitted to Journal of Geophysical Research: Atmospheres:

Abigail L. Gaddis, John B. Drake, Katherine J. Evans. "Evaluating Climate Predictability Signals in Response to Forcing: Mount Pinatubo as a Case Study." *Journal of Geophysical Research: Atmospheres* (2013) in prep.

Drake provided the predictability focus, conceptual guidance, and content organization for the paper. Evans generated the original parent simulations with volcanic aerosols, motivated additional analysis, provided expertise on configuring the climate model, and helped with diagnosis of model output. Gaddis chose the methodology to express predictability, configured and simulated the control runs without volcanic aerosols, programmed scripts to analyze and visualize the output, and wrote the paper.

3.1 Abstract

Decadal climate predictability is increasingly relevant for policymakers and stakeholders. Volcanic eruptions serve as a benchmark for assessing aspects of predictability because they provide a sudden global impulse to the Earth's climate system. In particular, the 1991 eruption of Mt. Pinatubo in the Philippines is of interest since it was the largest aerosol perturbation to the stratosphere in the twentieth century and the most intensely observed eruption on record. Using instrumental measurements during the eruption, the predictive skill of the model may be compared and the predictability of climate variables on seasonal to decadal time scales under forcing may be inferred. In this study, the evolution of the climate response to volcanic forcing is simulated in the Community Earth System Model, CESM1.0, using ensembles of forced and unforced global climate model runs. Ensemble averages and standard deviations for all atmospheric climate model variables are systematically calculated, with comparisons to observations to validate the accuracy of the model. The response for each variable to the eruption is evaluated using a unitless signal to noise ratio. The methodology employed in this work shows that the stratospheric water vapor response to the eruption

is both predictable and long-lived in comparison to other signals. Further, stratospheric humidity increases without any direct injection of water vapor into the stratosphere from the model. The spatial distribution of the tropopause temperature increase and corresponding specific humidity increase lend credibility to attribution of the signal to tropopause flux rather than direct injection. The response of water vapor to forcing could therefore provide a long-term source of predictability in the stratosphere.

3.2 Introduction

Decadal scale climate information is increasingly relevant for policymakers and stakeholders, as shown by the inclusion of this topic in the IPCC AR5 report. Identifying predictable variables and quantifying the duration of their predictability in response to climate forcings is important for decadal predictability studies (Meehl, Goddard et al. 2009; Taylor, Stouffer et al. 2012). The perturbation to Earth's climate from a large volcanic eruption is a short-term forcing that may be used to assess aspects of decadal predictability in global climate models. Predictability studies of volcanic eruptions differ from studies of climate change in that the evolution of the forcing is known, and they provide observations of climate response for model validation.

Volcanic eruptions can be used to analyze external forcing on the climate system because large eruptions perturb not only local weather conditions, but also the global climate. The most climatically important volcanic byproducts are sulfur species injected into the stratosphere; especially sulfur dioxide (Rampino and Self 1984). These sulfur compounds generally react within a few weeks to form sulfuric acid and sulfate aerosols. The optical properties of the sulfate aerosol cause some shortwave incoming radiation to reflect back into space, while absorbing more long wave radiation emitted from the Earth's surface (Robock 2000).

In particular, the June 15, 1991 eruption of Mt. Pinatubo in the Philippines is of interest since it was the largest aerosol perturbation to the stratosphere in the twentieth century. Furthermore, this eruption is the most intensely observed eruption on record since it occurred after the development of many modern climate data collection technologies, therefore, detailed measurements are available to use as a standard for climate models (McCormick, Thomason et al. 1995; Robock 2000). Observations show an increase in stratospheric temperature, a decrease in tropospheric temperature, and an increased equator-to-pole temperature gradient in response to the properties and distribution of the aerosol(McCormick, Thomason et al. 1995). The temperature gradient strengthened the polar vortex, causing a positive phase of the Arctic Oscillation. This led to a Northern Hemisphere winter warming pattern in the winter of 1992 (Robock and Mao 1992).

Generally, modeling studies have focused on replicating these observed effects, including hydrological (Gillett, Weaver et al. 2004), chemical (Stenke and Grewe 2005), biological (Gu, Baldocchi et al. 2003), and ocean dynamic responses (Church, White et al. 2005; Stenchikov, Delworth et al. 2009; Zanchettin, Timmreck et al. 2012). However, a comparative framework for evaluating the relative predictability of individual climate variables in response to forcing has not been developed. Identifying variables with comparatively longer predictive skill requires a more systematic approach. The objective of this study is to provide a framework for ranking the predictability of climate model variables. Furthermore, this work aims to determine less-studied variables that are highly predictable in response to volcanic forcing, and therefore, of interest for decadal climate change studies. Additionally, to provide direction for regional predictability studies and signal attribution, spatial analysis of the empirical orthogonal functions is performed.

3.3 Methodology

3.3.1 Data

3.3.1.1 Global climate model data

The model used for this study is the Community Earth System Model 1 (CESM), a coupled Earth system global climate model configured with an active atmosphere, active land model, data ocean, and prescribed sea ice (Gent, Danabasoglu et al. 2011). The atmospheric component is the Community Atmosphere Model version 4 on an Eulerian spectral T85 grid. This version of the atmosphere model contains the direct and semi-direct aerosol effects, but does not include the first or second indirect effect. While important for cloud related variables in the model, most indirect aerosol effects involve tropospheric aerosols. Since tropospheric volcanic aerosols settle out of the atmosphere in the first couple of months following the eruption, the indirect effect is not crucial to this study.

Volcanic aerosols are input to the volcanic aerosol module in CAM4 as a dataset of monthly mean masses in kg/m^3 on a meridional and vertical grid based on Ammann (2003). The aerosols are included as a single species composed of 75% sulfuric acid and 25% water. The aerosols are calculated to have a log normal size distribution, with an average effective radius of .426 micrometers and standard deviation of 1.25. Zonal variations in mass loading are not included. Simulations were conducted without volcanic aerosols as a control case ensemble. For these simulations, the monthly mean masses were set to zero from June 1991 to the end of the simulation.

The land component is the Community Land Model version 4 on a 0.9^o x 1.25^o lat/lon grid, the data ocean uses the Hadley Centre's sea surface temperature data on a 1^o grid (Rayner, Brohan et al. 2006), and the sea ice component is active, but ice extent is prescribed, matching the configuration and settings used in Evans et al (2013). All simulations were completed with the Jaguar supercomputer at Oak Ridge National Laboratory.

This configuration is widely used (Taylor, Stouffer et al. 2012) and is chosen because it provides a simplified experimental test bed to evaluate the capability of the signal to noise ratio technique to rank and quantify the relative impacts of forcing on the model. An advantage of this configuration is that simulated historical El Niño events are guaranteed to coincide with observations. This benefit is especially important for analysis of the volcanic forcing by Mount Pinatubo, given the positive El Niño phase immediately preceding the eruption (Robock 2000). Since the same El Niño state is in all model simulations, the impacts from the forcing of the eruption can be differentiated from responses to the El Niño state.

A thirty-year initial run covering the period 1975-2005 simulated one possible state of the system. Then, the initial atmospheric temperature values for the first run are randomly perturbed by a small amount to generate five additional thirty-year climate simulations. From each of these six ensemble members with observed volcanic aerosol data, a branch simulation is created a few months before the Pinatubo eruption. The volcanic aerosol mass-mixing ratio is removed following the eruption of Mt. Pinatubo for 48 months (January 1991 to December 1994). This creates an ensemble of six four-year branch runs corresponding to four years in the control simulations, but without the Pinatubo eruption.

The model response to the eruption should be closer to observations in the forced ensemble than other model configurations since the observed ocean response to the eruption is contained in the sea surface temperatures. However, the shortcoming of this configuration is that the control ensemble is still slightly forced by the data sea surface temperatures. Alternate ways to configure the data ocean for this control ensemble will all have shortcomings, since is no alternative Earth in which the true Earth's ocean state had no eruption. This model configuration provides a conservative estimate of predictability rather than an overestimate: differences between the ensembles will be damped by the slight presence of the ocean response to the eruption in the control ensemble. These simulations provide a simplified case to establish the predictability ranking framework and motivate later active ocean component simulations.

3.3.1.2 Observational and reanalysis data

Observations from two reanalysis datasets are incorporated in the global average ensemble mean graphs for certain variables to provide a comparison with global climate model data. The two reanalysis datasets are composites of instrumental records and short-term background forecasts dependent on previous data. The result is a gridded global dataset including observations as well as data from assimilation techniques and forecasts. For this study, monthly averages on a 2.5^{o} by 2.5^{o} grid were chosen from both datasets. The data were taken from January 1981 through December 1994. The ECMWF 40-year reanalysis data, known as ERA-40 (Uppala 2005), and the joint product from the National Centers for Environmental Prediction (NCEP) and the National Center for Atmospheric Research (NCAR), or NCEP reanalysis (Kalnay 1996), are both included.

Previous studies (Simmons, Jones et al. 2004; Bender, Ekman et al. 2010) contend that data from the European Centre for Medium-Range Weather Forecasts (ECMWF) for the eruption is more accurate than that provided by the joint product from the National Centers for Environmental Prediction (NCEP) and the National Center for Atmospheric Research (NCAR). It is thought that the differences between the datasets are due to the inclusion of more surface observation stations in the ERA-40 data (Bender, Ekman et al. 2010). In Simmons's comparison of the two datasets to processed station data, ERA-40 is found to have a higher correlation coefficient to the station data than the NCEP data for both hemispheres. Since the NCEP data is widely used, both data sets are included in this analysis for comparison with certain model variables of interest.

To assess radiative flux responses to volcanic aerosols, comparisons are made to observations. The NASA surface radiation budget (SRB) project (1983-2007) uses algorithms to derive a monthly 1^{o} by 1^{o} gridded dataset of radiation fluxes from satellite data. The SRB dataset relies heavily on satellite data from the International Satellite Cloud Climatology Project (ISCCP), especially in the time surrounding the eruption of Mt. Pinatubo. Flux variables monitored include shortwave and longwave radiation at the top of the atmosphere and at the Earth's surface. The SRB data is compared with model radiation flux variables for model validation.

3.3.2 Analysis methods

3.3.2.1 Global average predictability

Predictability studies of the second kind in climate change studies use an ensemble of unforced states to compare to an ensemble of forced states in order to distinguish internal climate variability from a deterministic signal (Hansen, Sato et al. 1997; Boer 2004; Van den Dool 2006; Von Storch 2008; Boer 2009). Predictability is then quantified as a signal to noise ratio between forced and unforced states of the system. For this study, this method is applied to two model ensembles: one six-member ensemble with volcanic forcing, and one six-member ensemble without volcanic forcing. The signal to noise ratio for a particular variable of the system, x, is:

$$S = \frac{\left|\bar{x}_f - \bar{x}_c\right|}{\sigma_c}$$

where $\bar{x}_f$ is the time-dependent ensemble mean of the variable in the forced ensemble, $\bar{x}_c$ is the same for the control ensemble, and σ_c is the standard deviation of the control ensemble. The numerator represents the difference of the ensemble means, an indication of the amplitude of the signal. The standard deviation of the ensemble in the denominator is a measure of the noise in the system, and therefore, S represents a measure of the signal to noise ratio over time (Von Storch 2008; Boer 2009; Meehl, Goddard et al. 2009). Since the variability may change in the forced dataset, it is important to have an ensemble of model runs for both the forced and control cases (Van den Dool 2006; Von Storch 2008). While some studies use the standard deviation of the forced ensemble, in this study the standard deviation of the ensemble without the Mt. Pinatubo eruption is used, since it should be more indicative of the unforced chaotic variability of the system.

First, the climatology of each atmospheric variable is calculated for the decade preceding the eruption from the long-term ensemble members. For variables with only one vertical level, the climatology is an average value for each month at each lat/lon grid point. For variables with more than one level, the climatology is computed at each horizontal grid point for every level. The climatology is removed from the period following the eruption (June 1991 to December 1994) in both ensembles to generate a grid of anomalies for each ensemble member. Next, the global average is calculated using weights to account for decreasing grid cell area at the poles. The ensemble average of the global average for the variable is then evaluated over time for each level. These values are plotted with the standard deviation among ensembles shown as shaded regions around the mean. The signal to noise ratio for all variables is calculated and plotted against time and the maximum values of the signal to noise ratio for each variable are compared to determine the most sensitive variables.

3.3.2.2 Spatial distribution of predictability

The spatial pattern of the predictability signals is examined by calculating the empirical orthogonal functions of the anomalies. The empirical orthogonal functions (EOFs) for each variable are computed in order to highlight the spatial response to the eruption and the evolution of the response in time. In climate studies, EOF analysis is often used to examine spatial modes of variability and how they change with time, for example, studying teleconnections such as the North Atlantic Oscillation, e.g. (Driscoll, Bozzo et al. 2012). This statistical method projects the data onto uncorrelated spatial vectors representing the direction of most variation, with the first empirical orthogonal function comprising the largest percentage of variation, the second the second largest, and so on. Each spatial pattern of variation has an associated time series. With the climatology removed, the eruption should provide the biggest source of anomaly in responsive variables. If so, the response of a particular climate variable to forcing should be in its first few EOFs.

EOF analysis is implemented on each atmospheric variable in the model. First, the decadal climatology in the form of monthly averages is removed from the data during the volcanic eruption period in each simulation for the forced and unforced ensembles. The ensemble average of the gridded anomaly for each variable is then computed for both ensembles, and the singular value decomposition of the covariance matrix is then performed. The difference between the forced and unforced ensemble EOF spatial patterns is mapped for the first three EOFs, and the corresponding EOF time series of the forced ensemble is plotted. This provides a summary of the major spatial modes in which the variable responds as well as an indication of how the variance changes over time in the forced modes.

3.4 Results

To validate the aerosol forcing simulated in the model, the modeled aerosol optical depth in the visible band is presented in Figure 3-1. The aerosol optical depth model output variable is the result of an input time series of volcanic aerosol mass mixing ratios for each vertical level in the model, which is then integrated into the active physics of the model. The signal to noise ratio is calculated as described in the methods section from the globally averaged ensemble values of the forced and unforced ensembles. The signal from this variable is positive, and is the highest of those examined, providing a benchmark of the maximum possible signal from the eruption, since it indicates the forcing on the system. As expected, the response begins in June 1991, reaching a peak around the end of 1991, slowly dropping as the aerosols settle out of the atmosphere.

Figure 3-2 shows how this influx of aerosols perturbs the balance for shortwave radiation overall, as more solar radiation is reflected out than usual by the extra aerosols in the stratosphere. Figure 3-3 displays the means for the clearsky net solar flux at the top of the atmosphere of each ensemble of model runs over time. The solid line labeled CESM1.0 FAMIP ensemble represents the ensemble mean of runs including observed volcanic aerosol data for the Pinatubo eruption, while the unforced model runs, CESM1.0 FAMIP no Pinatubo ensemble, have no volcanic aerosol input data for the Pinatubo period. The standard deviation between runs within each ensemble is shown as the shaded area around each line. This variation between runs within each ensemble is due to the internal variability of the system state. Comparing Figure 3-2 with Figure 3-3 highlights the relationship of the ensemble means and standard deviations with the signal to noise ratio. If the response is much stronger than anomalies induced by chaos, the signal to noise ratio is large, and vice versa.

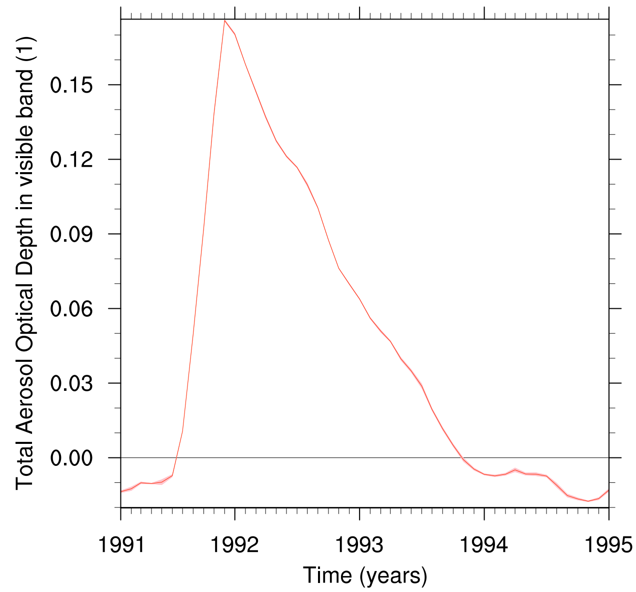

Figure 3-1. Total aerosol optical depth in visible band spatially weighted global average anomaly (forced ensemble only) from January 1991 to December 1994.

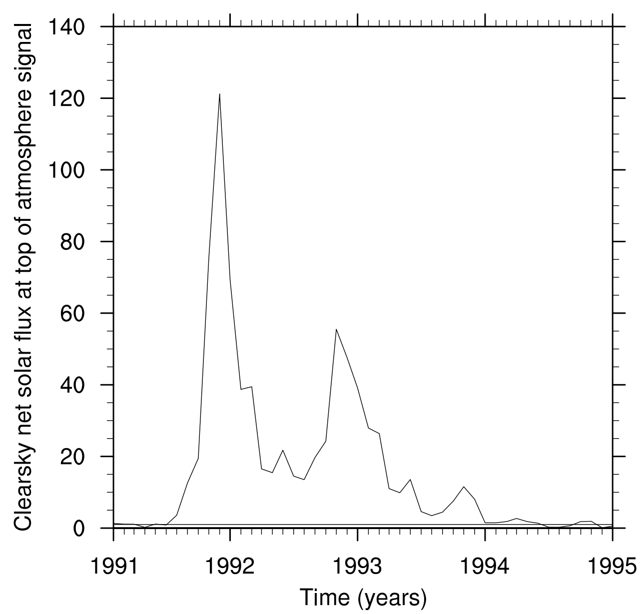

Figure 3-2. Clearsky net shortwave flux at the top of the atmosphere signal to noise ratio.

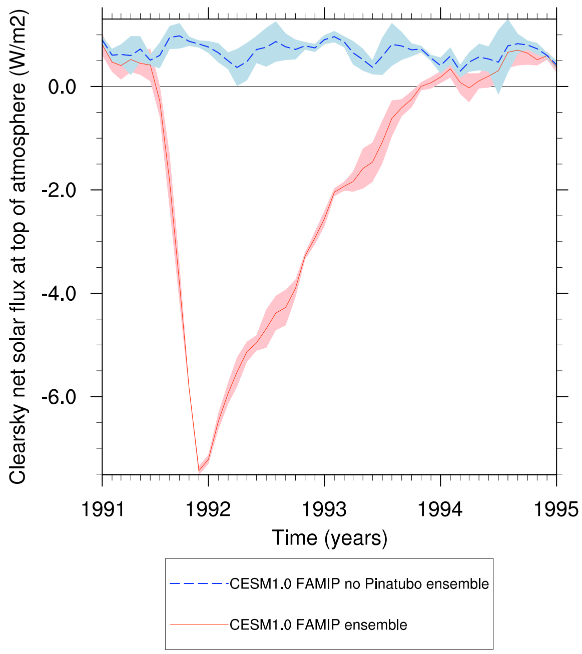

Figure 3-3. Clearsky net shortwave flux at the top of the atmosphere model ensemble mean decadal anomaly (blue and pink lines) and ensemble standard deviation (light blue and light pink shading).

The clearsky net shortwave flux response indicates the radiative imbalance caused by the aerosol forcing on the system, and since it is directly related to the forcing, the signal is strong. The radiation imbalance at the top of the atmosphere is due to the reflection and absorption of incoming radiation in the lower stratosphere, leading to the decrease in solar flux at the top of the atmosphere for 29 months seen in Figure 3-4. The radiative imbalance can also be seen in the other flux signals, especially the shortwave fluxes. A seasonal variation in the amplitude of the signal for the clearsky shortwave flux at the top of the atmosphere is noted. The seasonal peaks in the signal to noise ratio are related to a seasonal variation in the spread of the control ensemble, so that the variable is more predictable during north hemisphere winter than summer. The ensemble with the volcanic forcing also contains this seasonality in spread, although it does not contribute to the signal to noise calculation. Observations are not included in Figure 3-3 since the corresponding fluxes are not available.

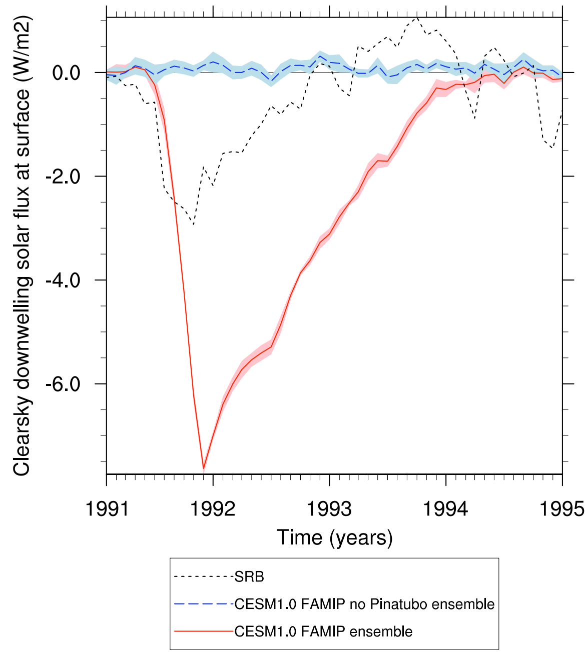

Figure 3-4. Surface clearsky shortwave downwelling flux ensemble means, standard deviations, and SRB satellite-derived data

Model upwelling and downwelling longwave and shortwave fluxes have been examined and compared with surface radiation budget (SRB) observations, as available, described in the previous section, at the surface and top of atmosphere. Radiation flux variables present in the observation dataset and the model (FLDSC, FLDS, FLNS, FLUTC, FLUT, FSDSC, FSDS, FSDTOA, FSUTOA; see appendix for abbreviation definitions) contain model anomalies in response to the eruption with the same sign as the related observations. The duration of the anomaly, 32 months in the model, is similar to that of the observations. However, the amplitude of the anomaly for the surface clearsky shortwave downwelling flux is much higher than observed. While this response is overestimated, the net longwave flux response at the surface is underestimated in the model, and the remaining flux variables show anomalies comparable to observations. As in the top of atmosphere net flux in Figure 3-3, the surface clearsky shortwave downwelling flux response in Figure 3-4 is strong due to its relationship with the forcing, with a negative maximum value of approximately 7 W/m^2. This is due to the reflection and absorption of incoming solar radiation by the stratospheric volcanic aerosol particles, so that less radiation is available to the surface than in the control ensemble.

The absorption of radiation by stratospheric volcanic aerosols results in an observed warming signal. This response is duplicated in the model, becoming predictable a few months after the eruption. Figure 3-5 demonstrates that the model temperature signal is strongest in the lower stratosphere, as expected (McCormick, Thomason et al. 1995; Robock 2000), lasting a maximum of 32 months in both the 35 and 50mb pressure levels. The model also responds to the eruption with a small negative tropospheric signal, reaching about 5.5 times the control run standard deviation at 850mb, as expected (McCormick, Thomason et al. 1995). The signal does not appear in figure 4a due to the strength of the stratospheric temperature signal.

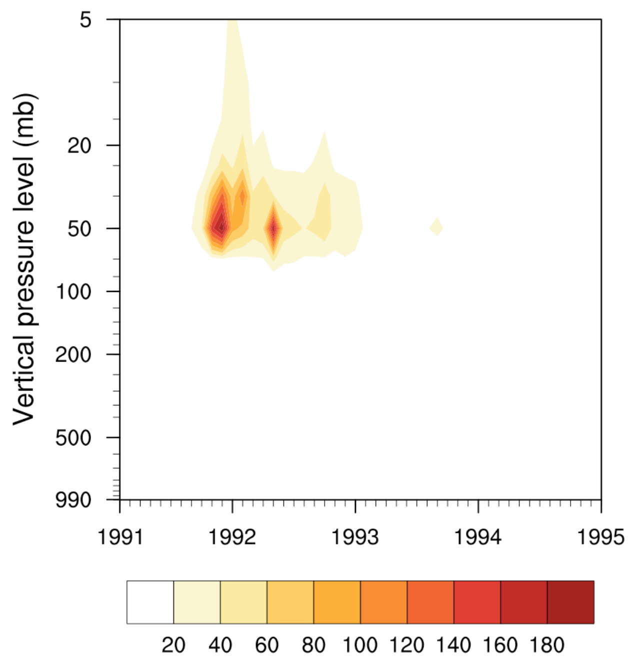

Figure 3-5. Global average temperature anomaly signal contour plot of vertical pressure level versus time from 1991 to 1995

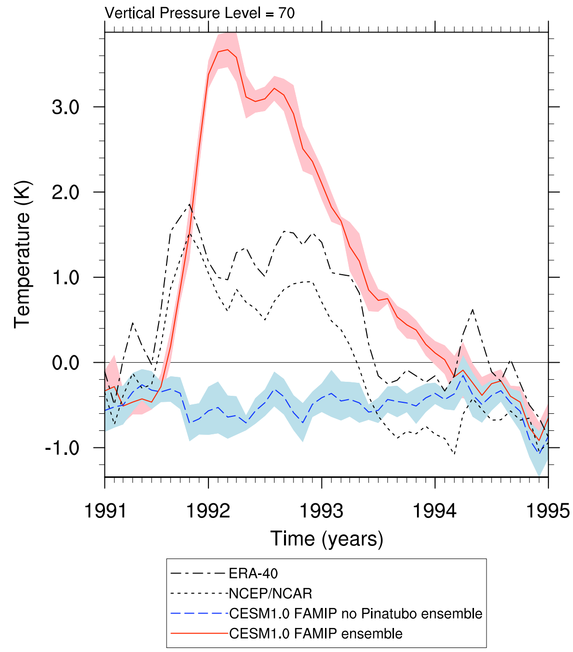

Figure 3-6. Global average temperature ensemble means, standard deviations, and ERA-40 and NCEP/NCAR reanalysis decadal anomalies for 70mb pressure level

Figure 3-6 shows the temperature ensemble averages and standard deviations as compared to ERA40 and NCEP observations at the 70mb pressure level. Like the shortwave downwelling flux shown in figure 3, the model temperature response is overestimated but of the same sign and approximate duration as the observations. The model troposphere temperature response signal to noise ratio is not significant and therefore does not appear in Figure 3-5. However, the tropopause and surface temperatures do record an anomaly from decadal climatology. This anomaly is not predictable for this model configuration, since the observed sea surface temperatures used in both ensembles decreases the difference between the ensemble means. The response of temperature to the eruption has been shown to be predictable in previous studies (Timmreck 2012), and this method correctly captures the predictability of the temperature response.

Figure 3-7 shows the difference of the first EOF of temperature in the forced and unforced ensembles at 70mb. The geographical pattern implies that the main difference between the two ensembles for the temperature at this level is a positive warming anomaly over the tropics. The EOF response pattern is confirmed with spatial plots of the signal to noise ratio at various times showing that the main signal is centered over the tropics.

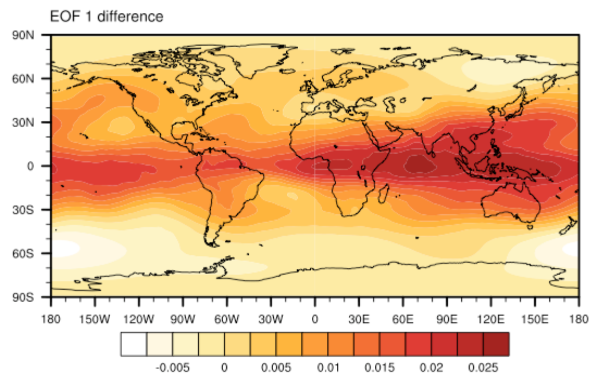

Figure 3-7. The difference of the first EOF of the global temperature anomaly for the forced and unforced ensemble averages

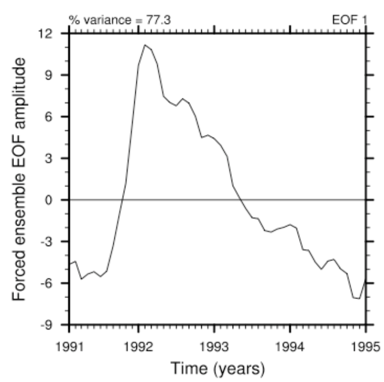

Figure 3-8. EOF time series for the first EOF of the forced ensemble average of the global temperature anomaly

Each spatial EOF pattern corresponds to a time series for each model run. The first EOF amplitude time series in the forced ensemble, Figure 3-8, evolves similarly to the forcing variable, as expected, which implies that the two are related. Additionally, the amplitude of the first mode in the forced runs is different from the amplitude of the first EOF in the unforced model runs. The percent variance explained by this first mode is

77.3% for the forced ensemble. The evolution of the EOF time series for the forced ensemble and the percent variance explained by the first EOF show that a strong mode of warming over the tropics arises due to the volcanic eruption.

The signal to noise ratio of geopotential height, shown in Figure 3-9, is significant in the stratosphere after the volcano, reaching a maximum of 28. The signal remains significant for 17-25 months, with the longest signal duration at the 10mb pressure level. The signal is the result of a positive geopotential height anomaly reaching about 200m above the control run average geopotential height. Following the eruption, positive temperature anomalies cause larger temperature gradients, leading to steeper gradients in geopotential height, especially near 50N and 50S in the stratosphere (not shown). By the thermal wind relationship, these changes in temperature and pressure gradients lead to increased stratospheric zonal winds, which can be seen in Figure 3-10.

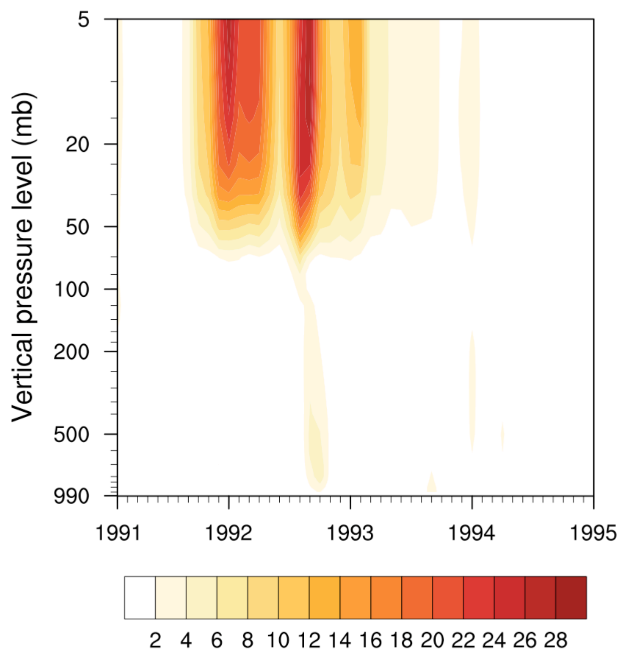

Figure 3-9. Global average geopotential height above sea level signal by level from 1991 to 1995

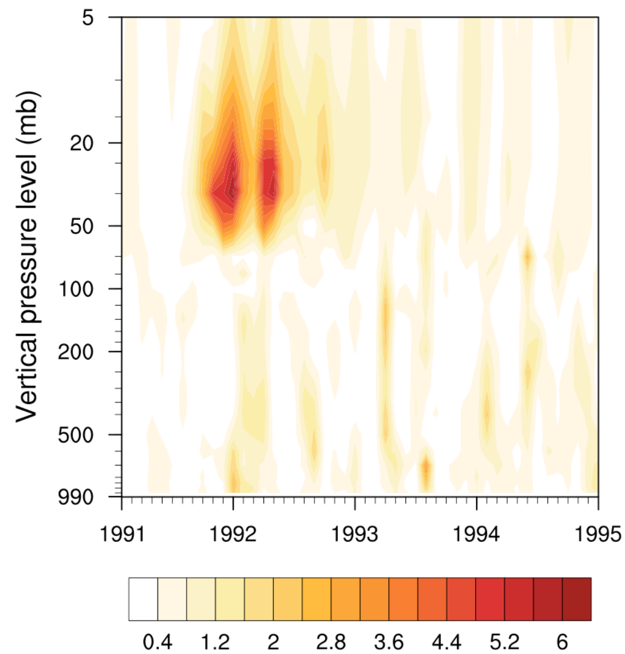

Figure 3-10. Global average zonal wind signal by level from 1991 to 1995

Figure 3-10 displays the signal to noise ratio for zonal wind following the eruption. The increase in zonal wind generated by the eruption has a two-peak distribution with maximum signals in January 1992 and May 1992, lasting about 4 months each. The maximum of the signal occurs at about 6.25 times the noise level, so structures in the plot with signals less than three are visible, which is not considered a significant level. The zonal wind anomaly in the perturbed runs is about 4 m/s at all levels, while the control runs without the eruption have little zonal wind variation. The increased signals at around 30mb occur due to lower standard deviation between the control simulations at that level.

The spatial distribution of the changes in the zonal wind indicates an increased polar night jet following the forcing to the system. The northern hemisphere reacts first and more strongly to the eruption in winter 1992, followed by a smaller signal in southern hemisphere winter, May - July 1992. This indicates a seasonal winter jet effect alternating between hemispheres. This generates the two peaks in the global zonal wind signal seen in Figure 3-11. The amplification of the polar night jets and its observed effect on the Arctic Oscillation after the eruption of Mt. Pinatubo has been described (Stenchikov 2006). This analysis confirms prior attribution of the stratospheric wind signal to temperature and pressure gradient changes, and quantifies the predictability of the response.

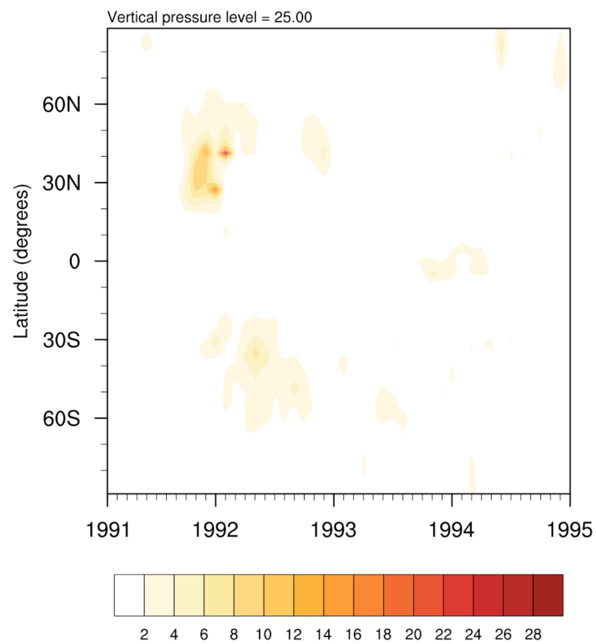

Figure 3-11. Zonal average distribution of zonal wind over the same time period

A notable effect of the simulated eruption is to increase stratospheric specific humidity in the model. In Figure 3-12, the vertical propagation of the specific humidity signal over time is shown. Stratospheric water vapor was shown to increase after the eruption in some observational measurements (Oltmans et al. 2000; Nedoluha et al. 1998), but many satellite measurements are underestimates of the response since their readings were disrupted by volcanic aerosols (Randel et al. 2004). The anomalous stratospheric water vapor following volcanic eruptions has also been noted in single simulation forced and unforced model studies (Considine, Rosenfield et al. 2001) and model studies without an unforced case (Stenke and Grewe 2005). In an attribution study linking tropopause warming and stratospheric humidity, Joshi and Shine use an ensemble of three simulations from a model of intermediate complexity, but have no control simulations (2003). The signal to noise ratio approach verifies these more limited efforts, and also quantifies the duration and magnitude of the predictability of the increase in stratospheric water vapor.

The signal to noise ratio provides evidence that the anomaly is both connected to the volcanic aerosols and statistically significant compared to the control run, with a maximum value of 11.5 times the control run spread. It is the sixth longest-lived model signal, behind temperature and radiative flux-related variables. These variables responded to the eruption earlier since they were a direct result of the forcing, and fell below 3 standard deviations of the spread before the end of the simulation. However, the specific humidity signal was still measurably different from the control ensemble at the end of the simulation. Responses of stratospheric humidity to forcing could therefore provide a long-term, near decadal predictability signal.

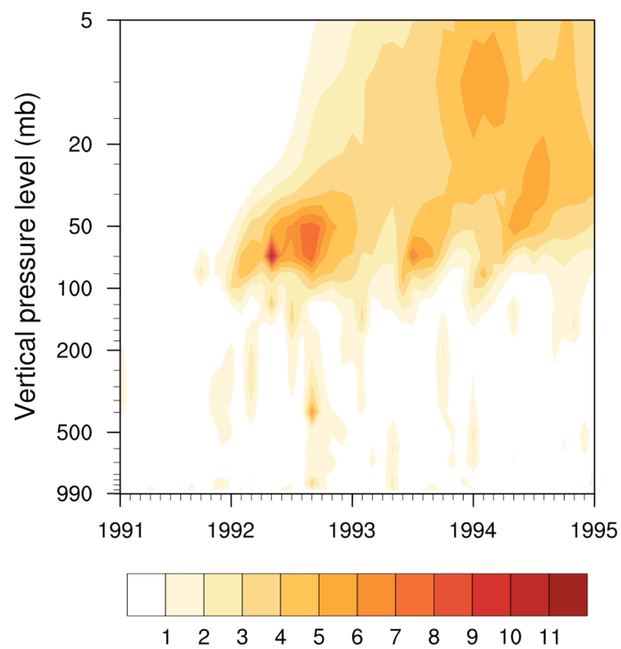

Figure 3-12. Vertical distribution of the signal to noise ratio of the global average specific humidity. The signal originates near the tropopause, spreading further into the stratosphere and gradually weakening. The signal remains significant for the rest of the simulation, with a total duration of 30 months at 35mb, and 12-27 months at other levels in the stratosphere. This signal remains significant until the end of the simulation in 1995.

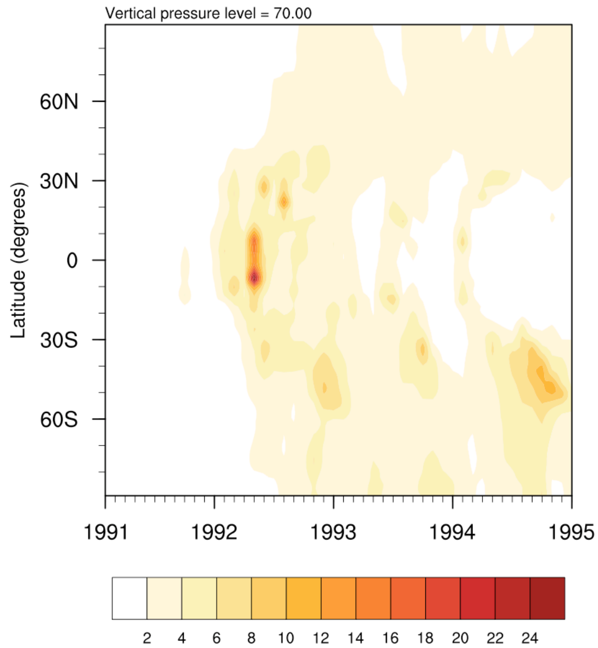

Figure 3-13. Zonal distribution of specific humidity signal for 70mb pressure level from January 1991 to December 1994. The anomaly begins as a weak signal centered over the tropics, becoming significant around February 1992. The signal then expands to higher and lower latitudes and eventually begins to fade toward the end of the simulation.

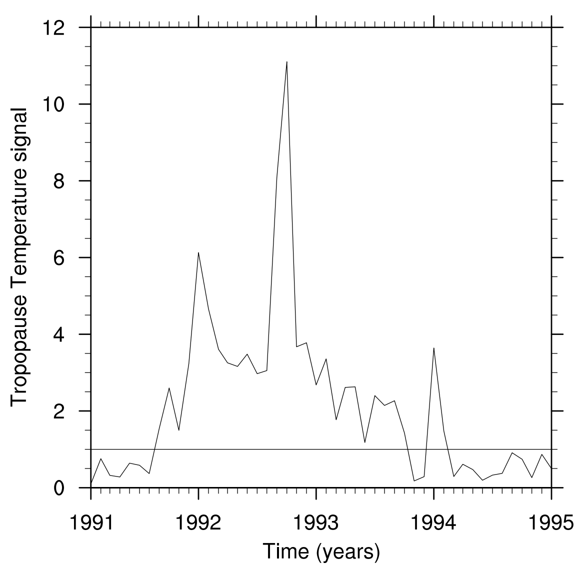

Figure 3-14. Global average temperature at the tropopause signal to noise ratio from 1991 to 1995. The warming signal in the tropopause after the eruption reaches 11 times greater than the ensemble standard deviation.

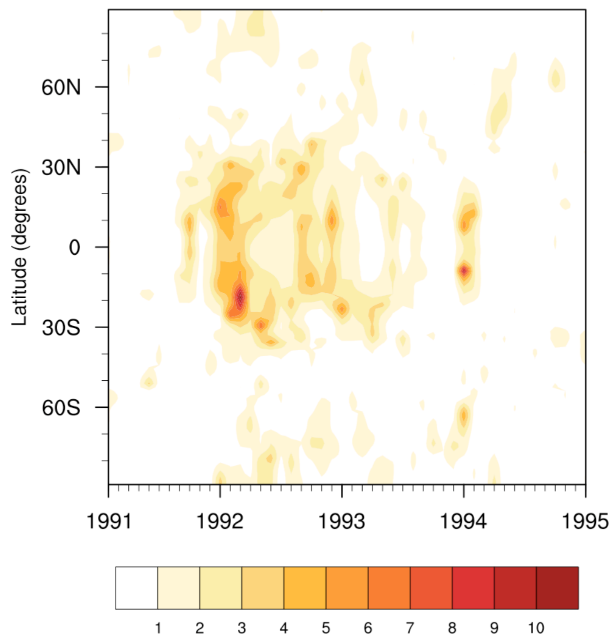

Figure 3-15. Zonal distribution of the tropopause temperature signal from January 1991 to December 1994. The spatial distribution of the warming of the tropopause indicates that the temperature increased over the tropics following the eruption before fading away by summer 1993, remaining significant for 7 months.

The mechanism behind the increase in stratospheric water vapor following the volcanic eruption is debated in the literature (Timmreck 2012). In general, air transfers from the troposphere to the stratosphere through warm air rising over the tropics. Water vapor in this air encounters the cold tropical tropopause, which freezes the liquid water out of the upwelling air. Observational correlations between stratospheric humidity and tropopause temperature exist (Mote, Rosenlof et al. 1996; Randel, Wu et al. 2004). One explanation of the increase in stratospheric humidity, then, is an increase in tropical tropopause flux due to warmer tropopause temperatures (Considine, Rosenfield et al. 2001). Another possible explanation for the increase in stratospheric water vapor is direct injection into the stratosphere from the eruption (Joshi and Jones 2009).

The results of this simulation point to a mechanism of increased cross-tropopause transport due to tropopause warming. The tropopause temperature does increase in the model, especially over the tropics, as shown in Figure 3-14 and Figure 3-15. The zonal distribution of the specific humidity near the tropopause (Figure 3-13) further lends credibility to a tropopause flux mechanism attribution, since the signal originates in the tropics region. Additionally, the specific humidity signal does not become significant until a few months after the eruption, indicating that direct injection by the eruption was not the mechanism for cross-tropopause water vapor transport.

One benefit of the unitless signal to noise ratio is that responses between variables may be compared for duration and strength. In order to visually rank the responses of model variables, Figure 3-16 plots the signals from all single level variables together. Of the 118 total variable analyzed, 74 were composed of a single vertical level, meaning that the variable is either a total column value or only evaluated at one vertical level, such as the surface or tropopause. The single level variables with maximum signal to noise ratios less than three are not included in figure 12. Energy flux related variables (FSUTOA through FLDS) have the largest signals, as expected, since they describe the radiative forcing induced on the climate system by the eruption. The tropopause related variables (TROP_Z, TROP_P, and TROP_T) are next in strength of response. Due to the experimental setup, tropospheric and surface variables show a weak response within about three standard deviations of the mean. Of the surface related variables, only the signal from the surface radiation was strong enough to appear.

While Figure 3-16 compares the signal to noise ratios over time for single level variables, Table 3-1. shows the maximum signal by level for the remaining 34 multiple level model variables. Blank values in the table represent variable levels composed of more than 30% missing values. Each row from left to right follows a variable from the stratosphere to the troposphere, as indicated by the increasing pressure values. The full names corresponding to the variable abbreviations are listed in the Appendix. As expected, the stratosphere shows the strongest response to the eruption. Temperature (T) and heat flux-related variables (DTV, DTH, QRS, QRL) consistently have the strongest signals compared to other variables, validating that these variables provide a good measure of the system's response to forcing. Particularly, the shortwave heating rate (QRS), followed by temperature, shows the largest and longest-lived anomaly relative to its control run spread. Geopotential height (Z3) is less sensitive to the eruption, responding at a maximum of about 28 times the noise. Relative humidity (RELHUM) displays a similar sensitivity to forcing, with a maximum of about 24 times the control ensemble spread for the variable. While only reaching a maximum signal value of 11.5, the specific humidity (Q) signal is the sixth longest lasting of the variables, significant for 30 of the 48 months modeled.

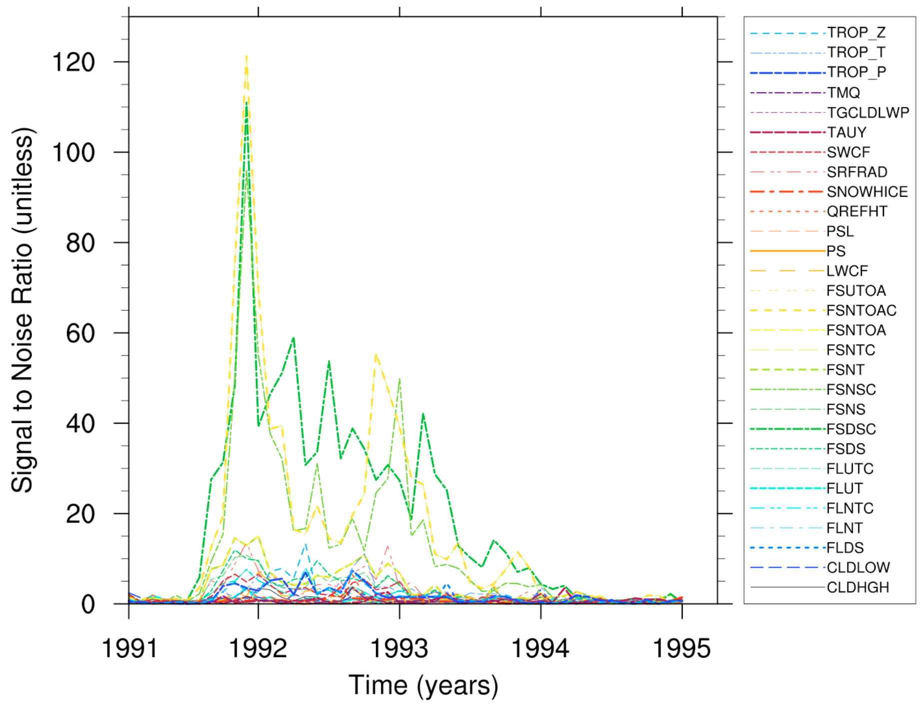

Figure 3-16. Comparison of signal to noise ratios for variables with one vertical level from 1991-1995

Near the tropopause, some cloud variables showed signals over three standard deviations, including the in-cloud ice mixing ratio, ice fraction, and cloud fraction variables. It is possible that this is generated from the effect of volcanic aerosols on cirrus cloud formation (Robock 2000). However, these signals are all comparatively short-lived, lasting 1-2 months. The cloud fraction is anomalously low around the tropopause for a brief period following the eruption, while the convective cloud cover fraction is also anomalously low in the same region over a similar period (not shown).

While the model signal radiative perturbation at the surface is clear (Figure 3-4) the tropospheric and hydrological model responses are within three to four standard deviations of the mean in this study, as can be seen from Figure 3-16 and Table 3-1.

Observations indicate the presence of tropospheric responses. For example, previous studies note an observed decrease in tropospheric temperature of 0.4°C by 1992 (McCormick, Thomason et al. 1995). Additionally, various studies note a decrease tropical precipitation, both in observations and modeling studies, following a large eruption (Gillett, Weaver et al. 2004; Schneider, Ammann et al. 2009; Gu and Adler 2011).

Table 3-1. Comparison of maximum values of signal to noise ratios for variables by vertical level in the atmosphere

Variable	Pressure (mb)												
	5	15	35	70	100	140	180	250	350	500	700	850	950
CLDICE	6.50	1.88	3.20	3.80	4.02	3.50	5.13	2.90	1.98	1.92	1.89	1.78	1.40
CLDLIQ	10.73				2.65	2.25	2.93	6.69	4.34	1.80	2.51	1.69	1.36
CLOUD				4.53	3.05	2.85	6.20	1.71	1.30	2.57	2.14	1.79	1.95
CMFDQ						2.05	2.24	1.89	1.82	1.68	1.35	1.94	2.17
CMFDQR						3.48	1.73	1.71	1.55	1.53	2.26	1.68	2.94
CMFDT				6.19	1.63	3.37	1.93	2.08	1.64	1.71	2.23	2.10	2.65
CONCLD				1.56	3.19	3.35	5.09	2.24	2.51	1.59	3.60	2.65	2.41
DCQ		1.88	3.20	5.51	2.68	2.53	4.91	4.29	2.29	1.90	1.80	1.27	1.47
DTCOND		1.73	3.13	6.24	1.62	2.36	3.20	2.87	3.96	1.82	2.21	4.87	2.45
DTH	2.85	4.06	5.74	2.36	4.46	3.98	3.14	1.80	1.62	2.12	1.70	2.68	3.29
DTV	15.64	66.15	76.23	3.82	2.59	2.24	2.35	3.68	2.11	1.86	1.82	1.72	2.41
FICE						5.22	15.38	3.18	2.55	4.36	1.68	3.70	1.92
GCLDLWP						3.51	5.44	3.77	3.55	2.07	2.14	1.52	1.42
ICIMR						1.88	2.24	4.74	1.37	1.54	2.38	2.38	3.11
ICLDIWP						2.51	2.87	3.20	2.47	3.04	2.97	2.36	2.85
ICLDTWP						2.51	2.87	2.74	2.03	2.24	3.01	1.70	2.37
ICWMR						11.27	4.15	3.86	2.29	1.63	2.27	2.26	1.30
OMEGA	2.03	4.37	5.40	3.44	1.54	2.25	3.81	1.80	1.64	2.42	1.75	1.71	2.00
OMEGAT	2.01	2.24	2.78	1.94	1.54	2.53	2.45	1.49	1.92	2.51	3.47	1.32	1.73
Q	4.89	5.27	5.61	11.46	3.92	3.50	2.05	2.86	3.93	2.30	2.12	3.36	2.31
QC				2.82	2.14	2.14	2.16	1.94	1.29	2.73	1.15	1.89	3.56
QRL	11.50	11.41	59.89	11.66	2.95	4.70	4.14	6.53	3.29	2.22	1.71	4.46	1.83
QRS	16.22	30.26	276.31	265.88	9.42	7.58	15.05	6.01	5.30	5.22	5.39	12.09	4.33
RELHUM	2.06	3.38	17.39	24.25	8.63	2.61	2.00	1.89	2.27	2.38	4.84	1.66	1.92
T	23.86	33.04	130.34	43.91	10.44	1.45	1.18	3.67	3.13	3.45	5.45	5.69	3.57
U	1.88	3.52	6.12	2.64	1.84	2.36	2.14	2.11	1.94	2.13	3.38	2.40	2.08
UU	5.08	4.89	6.76	2.36	1.16	3.42	2.01	1.70	1.65	1.70	2.98	3.44	1.49
V	1.47	1.77	2.42	1.66	2.19	1.35	2.79	1.80	1.54	1.33	6.35	1.24	2.38
VD01	5.23	5.27	9.77	2.21	2.78	2.02	2.07	2.64	1.86	1.70	2.05	1.54	2.28
VQ	2.18	1.81	3.24	1.64	2.22	1.49	2.10	1.89	2.35	2.01	1.99	1.25	2.26
VT	1.52	1.82	2.83	1.61	2.11	1.41	2.86	1.73	1.54	1.31	7.07	1.52	2.47
VU	2.72	1.76	1.44	2.02	1.60	2.42	2.32	1.58	1.86	2.44	2.70	2.63	4.02
Z3	27.86	27.17	23.02	7.45	2.54	2.77	3.47	3.93	4.00	4.55	5.52	4.38	3.22

3.5 Conclusion

Since the signal to noise ratio is unitless, comparisons between variable responses are made and quantitatively ranked relative to other model variables. The strongest model signals arise from the radiation flux variables, the second strongest signals occur in the temperature and heat flux-related variables, as is intuitively understood. This validates ranking the signal to noise ratios as a method for understanding the comparative strengths of model responses.

Most expected responses to the eruption are captured in the model, with some exceptions due to model configuration. Notably, the temperature response is positive and strongest in the stratosphere, following the temporal pattern observed after the eruption. The tropospheric temperature response is weaker than observed but is negative, as expected. Radiation fluxes also agree with observations. The zonal wind model response arises from temperature and pressure changes in the model. The increased gradients in these variables create stronger stratospheric winter jets than in unforced model cases. Some effects of the eruption that have only been recently recognized and attributed are captured by the breadth of this analysis methodology.

The methodology employed in this work shows that the stratospheric water vapor response to the eruption is both predictable and long-lived in comparison to other signals. Further, stratospheric humidity increases without any direct injection of water vapor into the stratosphere from the modeled eruption. The tropopause temperature increase in the model, especially over the tropics, corresponds to the stratospheric humidity increase. The stratospheric water vapor increases do not begin until a few months after the eruption and initially begin over the tropics. This lends credibility to attribution of the increased stratospheric water vapor following volcanic eruptions to increased tropopause water vapor flux rather than direct injection.

The choice of model configuration constrains the conclusions from this analysis. As mentioned in the results section, some tropospheric and hydrological predictability signals are not significant in this study due to observed data sea surface temperatures used in both ensembles. The observed data ocean used in this model configuration decreases differences between the control and forced runs for variables most influenced by the ocean, including those in the lower troposphere, hydrology-related variables, and cloud variables. The predictability of these variables will be calculated in future work with a fully coupled model configuration. A further bias in the response is due to the handling of aerosols in the Community Atmosphere Model version 4, the atmospheric component of CESM. While this version contains the direct and semi-direct aerosol effects, it does not include the first or second indirect aerosol effects. Most indirect aerosol effects involve tropospheric aerosols, important as a source of error in the model for cloud-related variables, rather than stratospheric aerosols. The impact to this study should be limited, especially after the first couple of months following the eruption, since the tropospheric volcanic aerosols settle out of the atmosphere more quickly than stratospheric aerosols. Comparisons with newer atmospheric models including indirect effects, such as CAM5, could serve to quantify this error, as well as providing a way to calculate the magnitude of their contribution to predictability. Additionally, since stratospheric aerosols create sites for chemical reactions, comparisons with active chemistry models could be made. However, increasing model complexity and computational expense are closely related.

The signal to noise ratio is a versatile metric that may be applied not only to global averages, but also to spatial analysis of the response of climate variables to forcing. The spatial distribution of the signal to noise ratio provides insight for attribution of responses and regional predictability analysis. While consecutive plots of the spatial distribution of the signal provide information about the evolution of the signal, EOFs provide a concise summary of the spatial pattern of the response to forcing. Applying the signal to noise ratio to rank variables and examine spatial response modes in large climate model datasets provides a rigorous way to search for and attribute predictability signals.

Acknowledgements: Gaddis is funded by the Institute for a Secure and Sustainable Environment at the University of Tennessee, Knoxville. Evans is funded through the U.S. Dept. of Energy Office of Biological and Environmental Research (BER) project, “Ultra High Resolution Global Climate Simulation to Explore and Quantify Predictive Skill for Climate Means, Variability and Extremes.” An award of computer time was provided by the Innovative and Novel Computational Impact on Theory and Experiment (INCITE) program. This research used resources of the Oak Ridge Leadership Computing Facility located in the Oak Ridge National Laboratory, which is supported by the Office of Science of the Department of Energy under Contract DE-AC05-00OR22725.

Chapter 4

PAPER 2: EFFECT OF ACTIVE OCEAN MODEL ON LAND AND ATMOSPHERE PREDICTABILITY IN RESPONSE TO THE ERUPTION OF MOUNT PINATUBO

A version of this chapter will be submitted to Journal of Geophysical Research: Atmospheres:

Abigail L. Gaddis, Katherine J. Evans, John B. Drake, Salil Mahajan. “Effect of Active Ocean Model on Land and Atmosphere Predictability in Response to the Eruption of Mount Pinatubo.” *Journal of Geophysical Research: Atmospheres* (2013) in prep.

Mahajan collaborated on analysis of sea surface temperatures. Drake helped with experimental design and theoretical framework. Evans generated long-term simulations with volcanic aerosols, helped with model configuration and experiment design, and advised on investigation of model output. Gaddis developed hypotheses, selected and implemented predictability methods, generated a control ensemble without the eruption, programmed analysis scripts, and wrote the paper.

4.1 Abstract

A central goal of climate research is to determine the perceptible effect of climate change on humans; in other words, the regional and decadal scale effects of carbon dioxide forcing. Identifying the most pronounced and long-lasting responses of climate variables to forcing is important for decadal prediction since forcing terms are one of the sources of predictability on those time scales. Volcanic eruptions provide a powerful, transient forcing on the global climate system by injecting tons of sulfur compounds into the stratosphere that react to form sulfate aerosols. The Community Earth System Model is used to explore the predictability of land and atmosphere responses to the Mount Pinatubo eruption. Predictable responses are compared to determine the relative sensitivity and duration of model responses to volcanic forcing. Novel predictable signals in response to the eruption are identified, including decreases in monoterpene and other volatile organic compounds, land snow depth and extent, and lake, soil, and snow heat content. Additionally, the standard deviation of the forced ensemble is reduced 8-14% as

compared to the unforced ensemble standard deviation. This implies that the model relative internal variability is reduced in response to the forcing.

4.2 Introduction

A central goal of climate research is to determine the perceptible effect of climate change on humans; in other words, the regional and decadal scale effects of carbon dioxide forcing. Identifying the most pronounced and long-lasting responses of climate variables to forcing is important for decadal prediction since forcing terms are one of the sources of predictability on those time scales (Meehl, Goddard et al. 2009; Taylor, Stouffer et al. 2012). Volcanic eruptions provide a powerful, transient forcing on the global climate system by injecting tons of sulfur compounds into the stratosphere that react to form sulfate aerosols. Unlike predictability studies of climate change, the full evolution of the forcing and response to a historical eruption has been observed. Therefore, eruptions may be used to assess aspects of decadal and regional predictability in global climate models.

The eruption of Mt. Pinatubo in the Philippines on June 15, 1991 is of particular interest since it was the largest aerosol perturbation to the stratosphere in the satellite observation era. Detailed measurements of the eruption using various modern techniques are available to use as a standard for climate models (McCormick, Thomason et al. 1995; Robock 2000). These observations show that atmospheric dynamics and chemistry responded to the radiative forcing and introduced by the volcanic aerosols. The temperature response to the aerosols, particularly the equator to pole temperature gradient change, introduced perturbations to the polar night jet and, consequently, surface winter warming in the Northern Hemisphere (Robock and Mao 1992). These observed atmospheric responses have been duplicated in climate model simulations, including temperature (Boer, Stowasser et al. 2007; Schneider, Ammann et al. 2009) and polar night jet (Stenchikov 2006) changes. Simulations of the response of teleconnections to the eruption (Emile-Geay, Seager et al. 2008; Wang, Ottera et al. 2012; Zanchettin, Timmreck et al. 2012) have also been completed.

Studies indicate that the Pinatubo eruption influenced Earth's surface as well as the atmosphere. For example, the eruption impacted the surface temperature (McCormick, Thomason et al. 1995; Gu and Adler 2011) and global hydrological cycle (Gillett, Weaver et al. 2004; Trenberth and Dai 2007; Gu and Adler 2011). Furthermore, vegetation growth and emissions from plants responded to the fraction of diffuse solar radiation and the decrease in temperatures following the eruption (Hansen, Lacis et al. 1992; Roderick, Farquhar et al. 2001; Gu, Baldocchi et al. 2003; Telford, Lathiere et al. 2010). Earth system model simulations of these responses have been performed to validate the representation of these individual processes in the model, especially the carbon cycle (Jones and Cox 2001; Lucht, Prentice et al. 2002; Brovkin, Lorenz et al. 2010).

Classifying the relative strength and duration of model responses is useful for diagnosis of the model representation of feedbacks, identification of variables with predictable responses to climate change, and development of novel sensitivity metrics. However, no comprehensive global climate model study on the relative predictability between land model responses to the eruption has been done to date. A previous study calibrated a framework for comparing predictability signals in climate models using atmospheric responses to the Pinatubo eruption in an atmosphere-land model (Gaddis, Drake et al. 2013). This work evaluates the relative predictability of atmosphere variables in a fully coupled global climate model to confirm and extend the previous results from a land-atmosphere model. The methodology of the previous study is extended here to investigate land model responses.

4.3 Methodology

4.3.1 Data

4.3.1.1 Global climate model data

The model used for this study is the Community Earth System Model 1 (CESM), a coupled Earth system global climate model (Gent, Danabasoglu et al. 2011), configured with interacting active atmosphere, land, sea ice, land ice, and ocean components. The atmospheric component used for all simulations in this study is the Community Atmosphere Model version 4 (CAM4) on a spectral Eulerian T85 grid. The land component is the Community Land Model version 4 on a 0.9^{o}x1.25^{o} latitude/longitude grid. The model configuration includes the POP2 ocean and CICE sea ice. The CN cycle in the land model and active ozone chemistry in the chemistry module in the model were not active for this configuration.

CAM4 contains direct and semi-direct aerosol effects, but does not include the first or second indirect effect. Indirect aerosol effects in the troposphere are important as a source of error in the model for cloud related variables. Tropospheric volcanic aerosols settle out of the atmosphere more quickly than stratospheric aerosols, for Mount Pinatubo, a few weeks after the eruption. Therefore, the impact of this simplification to this study should be limited, becoming negligible after the first couple of months following the eruption.

Volcanic aerosols are input to the volcanic aerosol module in the atmospheric model as a dataset of monthly mean masses in kg/m^3 on a zonally averaged grid with multiple vertical levels (Ammann 2003). The aerosols are estimated to be a single species composed of 75% sulfuric acid and 25% water. The aerosol size distribution is lognormal, with an average effective radius of .426μm and standard deviation of 1.25. To form a control case ensemble, these values are set to zero after the Pinatubo eruption in the control simulations.

To distinguish internal climate variability from a deterministic response to forcing, predictability studies use ensembles of forced and unforced model states (Hansen, Sato et al. 1997; Boer 2004; Van den Dool 2006; Von Storch 2008; Boer 2009). For this study, an ensemble of possible climate states with volcanic forcing is generated by perturbing ocean initial conditions. Ocean initial conditions in 1975 are set to January – May 1980 spun-up ocean settings to create a total of five ensemble members lasting from 1975-2005. Ocean initialization procedures are further outlined in McClean (2011).

In order to provide a comparable base case ensemble of five members, a branch simulation is created a few months before the Pinatubo eruption for each forced ensemble member. The volcanic aerosol mass-mixing ratio is then set to zero following the eruption of Mt. Pinatubo, June 1991 to August 1995. This creates a control ensemble of five model states without the forcing of the Pinatubo-like volcanic aerosols. The simulations were run on the Jaguar supercomputer at Oak Ridge National Laboratory.

It is important to distinguish responses to the volcanic eruption from responses to the positive El Niño phase immediately preceding it (Robock 2000). Modeled El Niño-Southern Oscillation (ENSO) states vary at the time of the eruption in the forced ensemble, providing a range of possible model states for each variable. Each simulation without volcanic aerosols branches from its forced parent simulation a few months before the eruption. In this way, the ENSO state is the same at the time of the eruption between a forced parent run and its related unforced run in the control ensemble. The unforced and forced ensembles then each comprise five identical El Niño states, and the predictability signal to noise ratio calculation is unaffected by the state of ENSO. Additionally, ENSO state was statistically regressed from the sea surface temperatures to determine the effect of the volcano on ENSO. Sea surface temperature anomalies were regressed against the ENSO index, and the residuals were computed.

4.3.1.2 Observational data

Comparisons to observations are performed for key model variables for validation. Two reanalysis datasets are used for assessment: the ECMWF 40-year reanalysis data, known as ERA-40 (Uppala 2005), and the joint product from the National Centers for Environmental Prediction (NCEP) and the National Center for Atmospheric Research (NCAR), or NCEP reanalysis (Kalnay 1996). The two reanalysis datasets are gridded global datasets including observations as well as data from assimilation techniques and forecasts. For this study, monthly averages on a 2.5^{o} by 2.5^{o} grid were selected, and seasonality was removed. The reanalysis anomalies were generated over the same period, June 1991 to August 1995, as the model anomalies.

The NASA surface radiation budget (SRB) project (1983-2007) uses algorithms to derive a monthly 1^{o} by 1^{o} gridded dataset of radiation fluxes from satellite data. The SRB dataset relies heavily on satellite data from the International Satellite Cloud Climatology Project (ISCCP), especially in the time surrounding the eruption of Mt.

Pinatubo. Flux variables monitored include shortwave and longwave radiation at the top of the atmosphere and at the Earth's surface. The SRB data is compared with model radiation flux variables for model validation.

4.4 Methods

4.4.1 Global Average Predictability

A measure of predictability is the signal to noise ratio between forced and unforced states of the model, in this case, with and without volcanic aerosols. The signal is defined as the difference of the ensemble means, while the noise is the standard deviation the ensemble about its ensemble mean, as in some previous studies (Von Storch 2008; Boer 2009). Since the ensemble mean and ensemble standard deviation are taken at each point in time, this results in a signal to noise ratio time series quantifying the evolution of the predictability of the response to the eruption for that variable. The ensemble standard deviation chosen to represent the noise is from the ensemble with Pinatubo aerosols removed, since it should be more indicative of the unforced variability of the system. The signal to noise methodology is described in more detail in the previous work (Gaddis, Drake et al. 2013).

Anomalies following the eruption are calculated for each land and atmosphere variable in ensemble member by removing the previous decade's climatology. The weighted global average of the variable anomaly is averaged over the ensemble, and for variables with a vertical component, for each pressure level. These values are plotted with the standard deviation among ensembles shown as shaded regions around the mean. Atmospheric signal to noise ratio and signal duration from the previous work (Gaddis, Drake et al. 2013) are compared with the results from the fully-coupled model configuration to show the influence of the active ocean. Land variable signal to noise ratios are additionally calculated for the fully-coupled configuration to identify predictable responses.

4.4.2 Spatial Distribution of Predictability

Two methods are used to examine the spatial pattern of the predictability in the model following the eruption: the spatial pattern of the signal to noise ratio is mapped, and the empirical orthogonal functions of the anomalies are calculated. As in the procedure above, a spatial map of the anomaly post-eruption is calculated by removing the climatology from both ensembles. The ensemble averages with and without the volcano and the ensemble standard deviations are computed at each grid point. The difference of the means divided by the standard deviation of the control ensemble is then calculated at each point, generating a map of the predictability.

For further understanding of the spatial response and how it varies over time, the empirical orthogonal functions (EOFs) for each variable are computed. The ensemble average of the gridded anomaly for each variable is computed for both ensembles, and the singular value decomposition of the covariance matrix is then performed. With the climatology removed, the eruption should provide the biggest source of anomaly in responsive variables. If so, the response of a particular climate variable to forcing should be in its first few EOFs. The forced ensemble EOF spatial patterns are mapped for the first three EOFs, and the corresponding EOF time series is plotted. This summarizes the major spatial modes of variable response to the eruption as well as how the variance changes over time in the forced modes.

In summary, two model configurations are analyzed: an atmosphere-land configuration, and a fully-coupled atmosphere-ocean-land-sea ice configuration. The two ensembles of simulations for each configuration provide a variety of states of the system in both forced and unforced modes. This is so that anomalies due to variation within the system can be differentiated from predictable responses to the eruption. The signal to noise ratio summarizes the difference between the forced and unforced ensembles statistically so that predictable changes of the forced system for that variable are quantified. Specific regions of higher predictability are identified through mapping the signal to noise ratio and the empirical orthogonal functions. The predictable responses of the system are compared for the two model configurations.

4.5 Results

For the active ocean simulations, the ensemble standard deviation of atmospheric and land variables over time is smaller, on average, with the volcano than without volcanic aerosols for most variables. The standard deviation of variables with no vertical component decreases by an average of 8%, while those with vertical atmospheric levels have a reduction of 14% (see Table A-1 for values for each variable). The forced runs have a lower standard deviation than unforced runs for almost every variable. This contrasts with results from simulations without active ocean, which had no consistent trend in the standard deviation.

4.5.1 Atmospheric responses

The expected atmospheric responses to the eruption are well represented in the model. The expected radiation flux responses occur in the stratosphere, and surface radiation fluxes are affected. The proportion of diffuse radiation at the earth's surface increases in both the visible (Figure 4-1) and infrared wavelengths, as expected from observational data.

The stratospheric specific humidity responds predictably to the eruption (Figure 4-2). The duration of the predictability for the signal is relatively long compared to the duration of other variables (see Table A-2 in appendix), but is shorter than in the land-atmosphere model configuration. In addition to the previously modeled predictable stratospheric specific humidity increase (Gaddis, Drake et al. 2013), a tropospheric decrease in humidity is also predictable for the fully coupled model. The modeled eruption does not include the direct inject of water vapor into the stratosphere, as is reflected in the lagged response to the eruption. Therefore, the alternate mechanism of increased water vapor flux across a warmed tropical tropopause is upheld in this study.

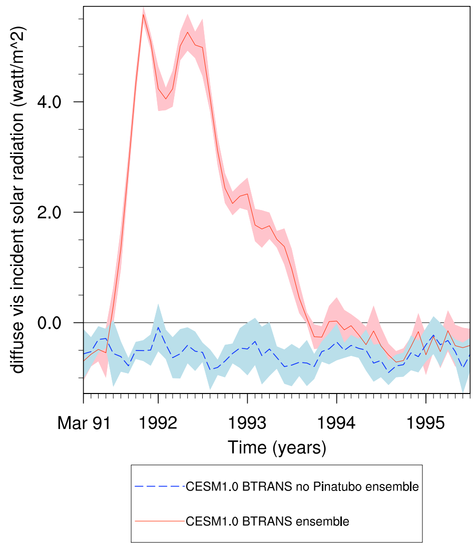

Figure 4-1. Model diffuse visible incident solar radiation anomaly from decadal climatology at the surface signal to noise ratio over time. Diffuse visible radiation increases at the surface following the eruption in June 1991 for about two years, as expected.

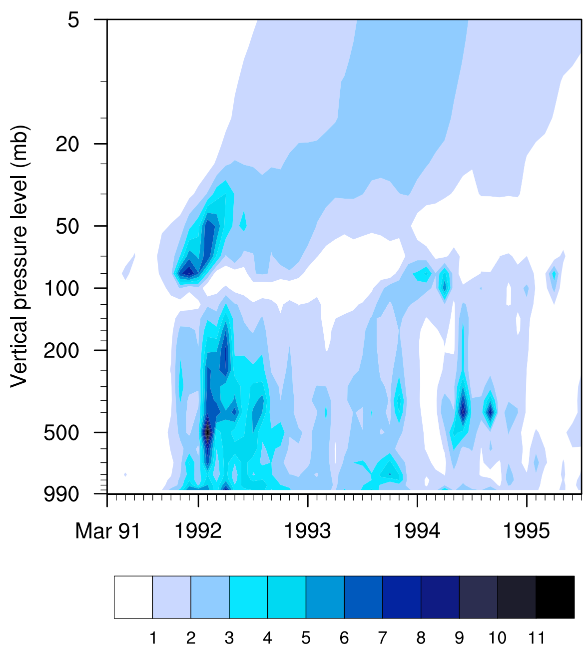

Figure 4-2. Specific humidity signal to noise ratio from March 1991 to July 1995 against log pressure in the atmosphere. The response becomes predictable in fall 1991, a few months after the eruption. It reaches a maximum predictability of 11 times the noise in the control ensemble, remaining above three times the noise for up to 10 months.

The relative humidity signal is significant only in the stratosphere, in contrast (Figure 4-3). Taken along with the temperature decrease in the troposphere (not shown), this implies that the negative signal of specific humidity in the troposphere is due to temperature-related effects. Cooler air holds less humidity, so the humidity in the troposphere decreases proportionately. The stratospheric anomalies of both the specific humidity and relative humidity together confirm that there is more water vapor in the stratosphere following the eruption.

Figure 4-4 shows that the model configuration with active ocean captures the warming signal in the stratosphere. As before as with the previous model configuration, the warming signal in the stratosphere is so strong that it does not allow the tropospheric cooling signal to be seen. However, for the fully coupled model, the tropospheric cooling signal peaks around 11 times the noise, much stronger than the atmosphere-land configuration, which peaks around 5 times the noise.

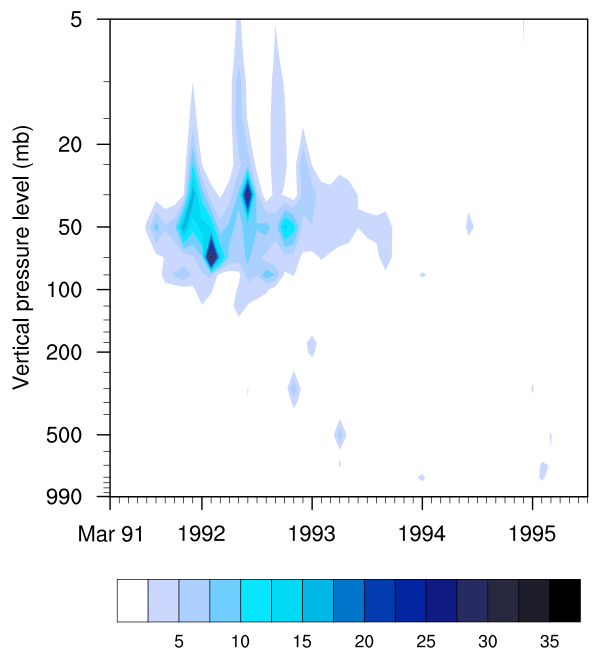

Figure 4-3. Relative humidity signal to noise ratio from March 1991 to July 1995 for each vertical pressure level in the atmosphere. Relative humidity increases only in the lower stratosphere following the eruption. The signal remains significant until 1994.

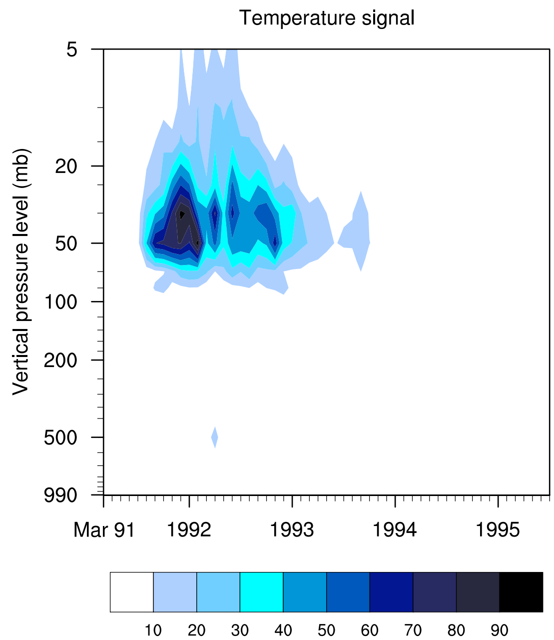

Figure 4-4. Temperature signal to noise ratio from March 1991 to July 1995 for each vertical pressure level in the atmosphere. The warming signal in the stratosphere is so large that not much of the weaker tropospheric cooling response is shown in this plot.

Including an active ocean component allows the response of the geopotential height to differ between control and forced ensembles in the troposphere (Figure 4-5). The response of the geopotential height to the eruption in the stratosphere is similar in vertical distribution and timing to the data ocean response, but the signal is less predictable. This is a result of increased standard deviation as well as a slightly smaller difference between the control run mean and the perturbed run mean. Additionally, the effect of the volcanic aerosols on the geopotential height is now shown in troposphere as well. The tropospheric response is predictable for a longer duration than the stratospheric response.

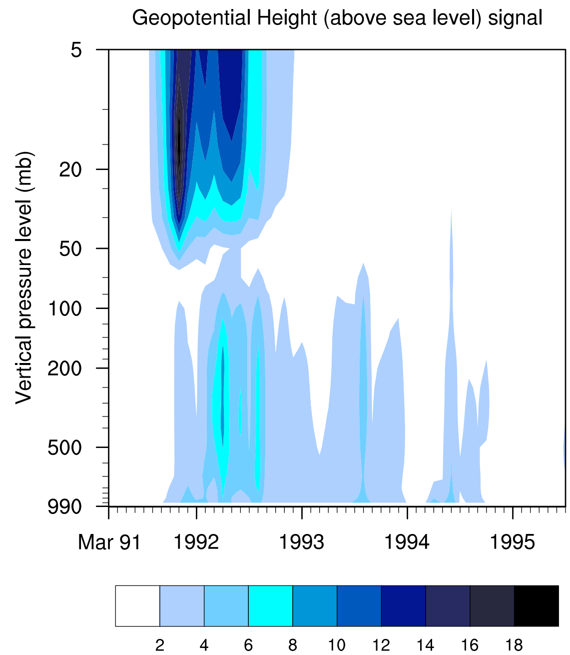

Figure 4-5. Geopotential height signal to noise ratio from March 1991 to July 1995 for each vertical pressure level in the atmosphere. The signal reaches 18 times the noise in the stratosphere, while a weaker response occurs for a longer duration in the troposphere.

With the atmosphere-land model configuration, the zonal wind signal was clearly a polar night jet response oscillating between hemispheres. The timing and spatial distribution of the responses are less defined in the fully-coupled simulations due to decreased signal strength relative to the FAMIP configuration. However, the fully coupled simulations still indicate a polar night jet response in the northern hemisphere winter in 1991, as shown in Figure 4-6. This agrees with many previous observational records and model studies that show increased polar jets leading to an enhanced positive phase of the Arctic Oscillation in NH winter 1991 and 1992 (Robock and Mao 1992; Stenchikov 2006).

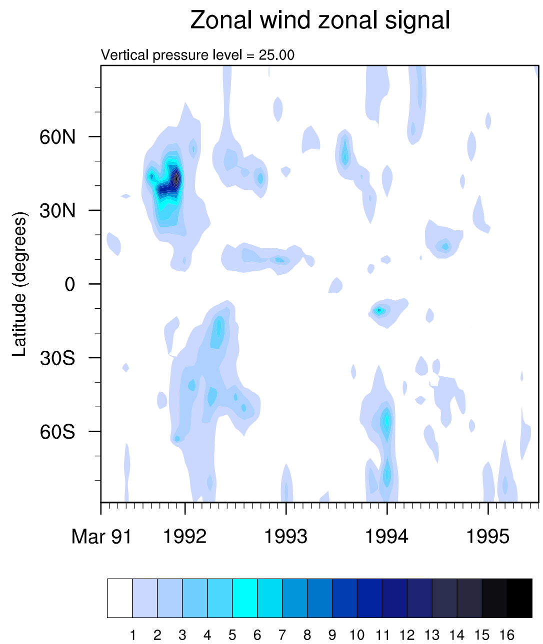

Figure 4-6. Zonal wind signal to noise ratio zonal average from March 1991 to July 1995. The response in the NH zonal wind is present in winter 1991, but the observed winter 1992 anomaly is not predictable for this model configuration.

For the fully coupled model configuration, cloud and precipitation variables are seen to predictably respond to the eruption. Convective cloud cover decreased in the model following the eruption, with a signal to noise ratio above 3 in the 160-250 mb pressure levels for about two months (Figure 4-7). The total cloud amount also responds to the volcanic aerosols in the model, decreasing in the forced ensemble to about four times the noise. The signal to noise ratio remains significant only for one month (Figure 4-8).

The total precipitable water signal is not significant in the data ocean model configuration. However, Figure 4-9 shows that this signal reaches over eight times the noise level for the active ocean model configuration ensembles. This increase in precipitable water is above three times the noise level for eight months, and indicates a hydrological cycle response to the volcano that is not seen in the previous configuration. From the meridional average spatial distribution of the signal to noise ratio (not shown), the response mainly occurs over the 50^{o} to 150^{o} longitude region.

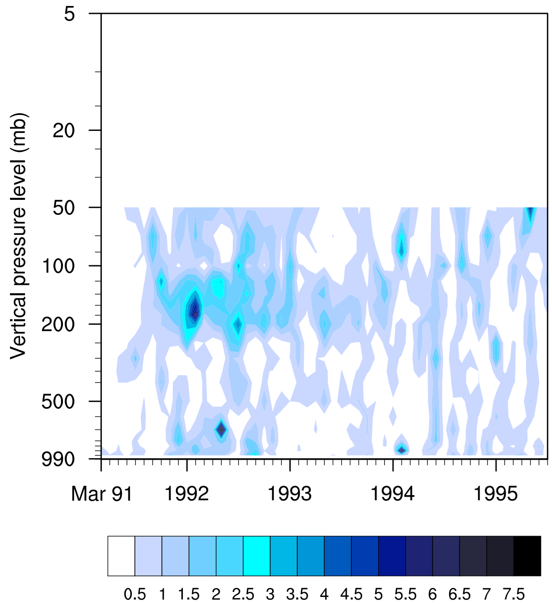

Figure 4-7. Convective cloud cover signal to noise ratio from March 1991 to July 1995 for each vertical pressure level in the atmosphere. Above 50 mb, few clouds occur. The response occurs in winter 1991 and remains significant until 1992. Values of the SNR below 1 are considered noise.

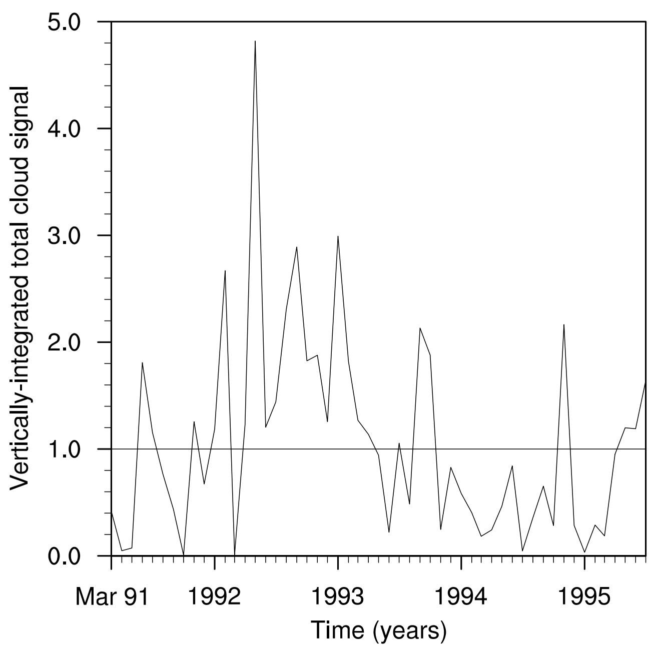

Figure 4-8. Model vertically-integrated total cloud signal to noise ratio from March 1991 to July 1995.

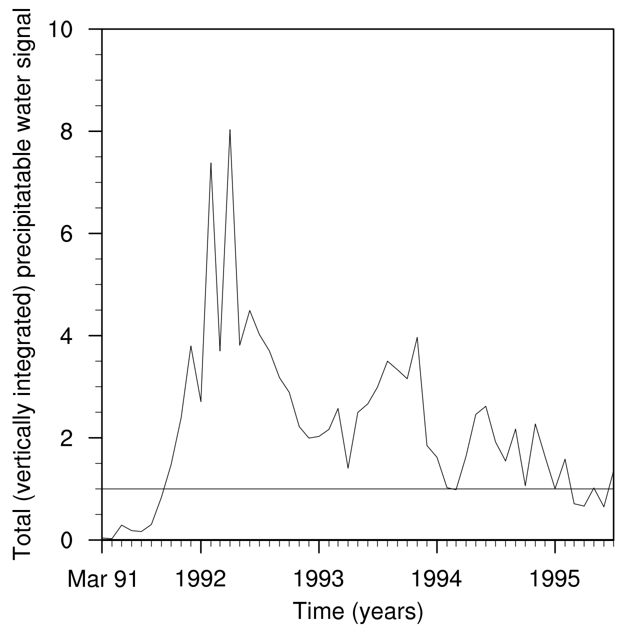

Figure 4-9. Model total precipitable water signal to noise ratio from March 1991 to July 1995. The response is strongest in 1992, remaining significant at 2σ until the end of 1993.

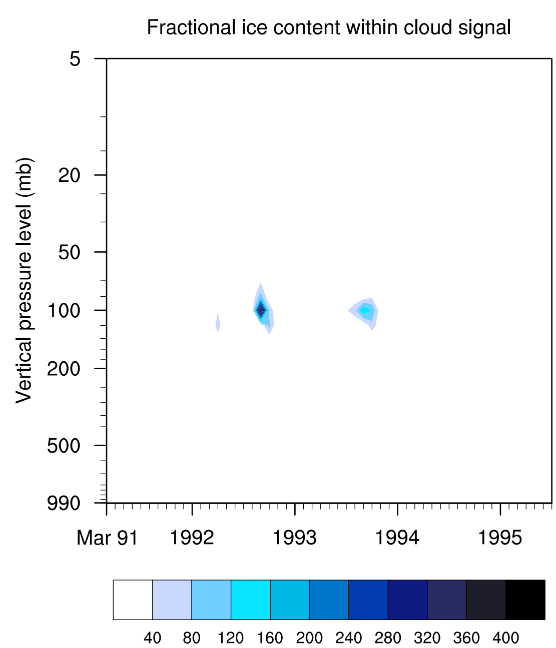

Figure 4-10. Cloud fractional ice content signal to noise ratio from March 1991 to July 1995 for each vertical pressure level in the atmosphere. The response remains predictable for 8 months at model levels around 85mb and 5 months around 350 mb.

The cloud fractional ice content (Figure 4-10) includes some sharp peaks, so values over 30 are set to 30 in order to show the lower signal amounts as well as the location of the maxima. The increase in cloud fractional ice content around 350mb is probably more physical than the modeled stratospheric decrease in fractional ice content due to a greater number of data points for that region of the atmosphere. The 350mb increase reaches a maximum of eight times the noise, centered about the equator.

4.5.2 Land and surface responses

The known response of decrease in sea surface temperatures is replicated in the model. Figure 4-11 shows that additionally, the cyclical increases in natural variability are damped by the eruption in the model. The time evolution of the first EOF in Figure 4-12 appears correlated to forcing, and the associated spatial pattern is centered over the Niño 4.5 region (Figure 4-13). To extract the effect of the eruption on the El Niño, the ENSO index is regressed from the sea surface temperatures, and the residuals are analyzed. The residuals do not show a measurable response to the eruption.

The surface temperature in BTRANS decreases in the forced ensemble relative to the control ensemble, shown in Figure 4-14, as expected from observations. This response was not significantly different from the control ensemble in the previous data ocean model configuration. The BTRANS response peaks sharply in November and December 1991 due to very low variability in the control ensemble for those months. The signal continues to be predictable for six months. The decrease in surface temperature is especially centered over continental land masses (not shown).

The fraction of surface area covered by sea ice in the model also increases predictably in response to the eruption for this model configuration. Cooler surface air temperatures lead to greater sea ice area coverage, seen in Figure 4-15. This effect is expected, and through the sea ice albedo feedback, can lead to climate regime changes for large enough eruptions (Rampino and Self 1992).

The atmospheric pressure at the Earth's surface shows a response to the eruption peaking at about eight times the spread of the control ensemble. This is a physical response to the temperature increase that was not seen for the previous model configuration. The decrease in surface pressure continues to be predictable for eight months after the eruption (Figure 4-16).

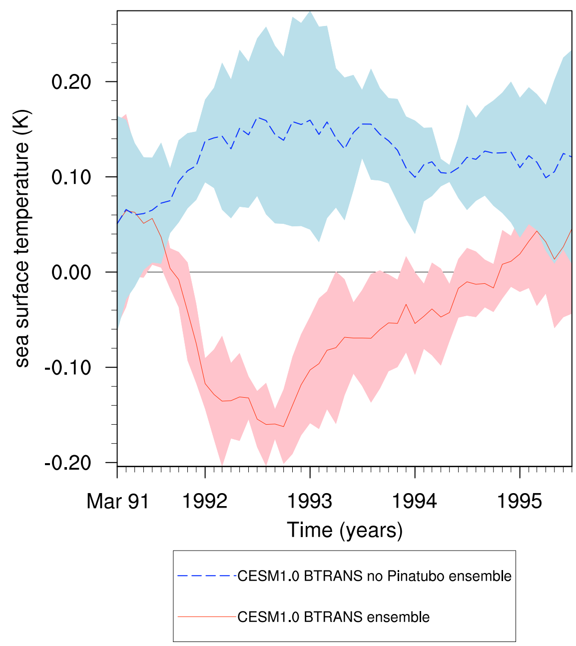

Figure 4-11. Sea surface temperature anomaly for forced (red) and unforced (blue) ensembles. The sea surface temperatures respond to the volcanic forcing in two ways: the sea surface temperatures decrease globally, and the ensemble variability (shading) is diminished, especially the cyclical increases in variability.

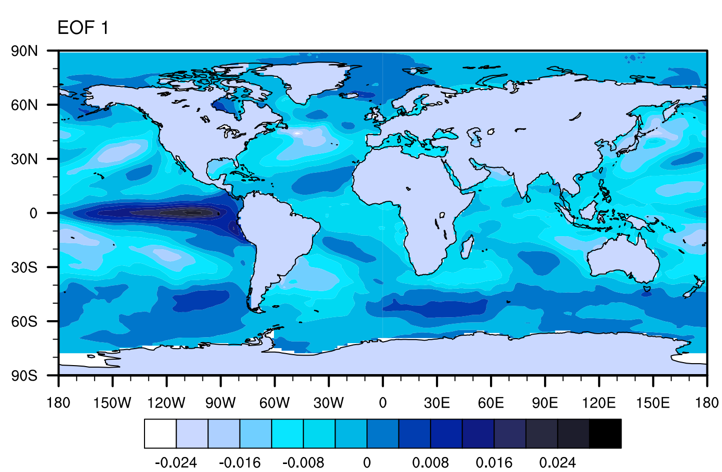

Figure 4-12. EOF 1 spatial pattern of the forced ensemble sea surface temperature anomalies. The peak of this EOF is centered over the Nino 4.5 region in the Pacific ocean.

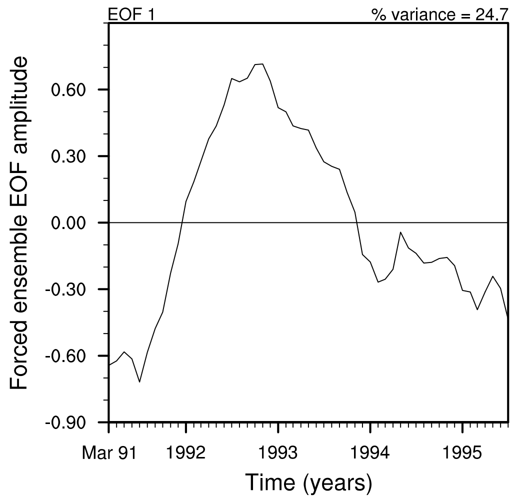

Figure 4-13. PC1 time series of the forced ensemble sea surface temperature anomalies, associated with EOF1 in Figure 4-12. The largest portion of the SST anomaly variance (EOF1 at 24.7% variance) appears correlated to the eruption.

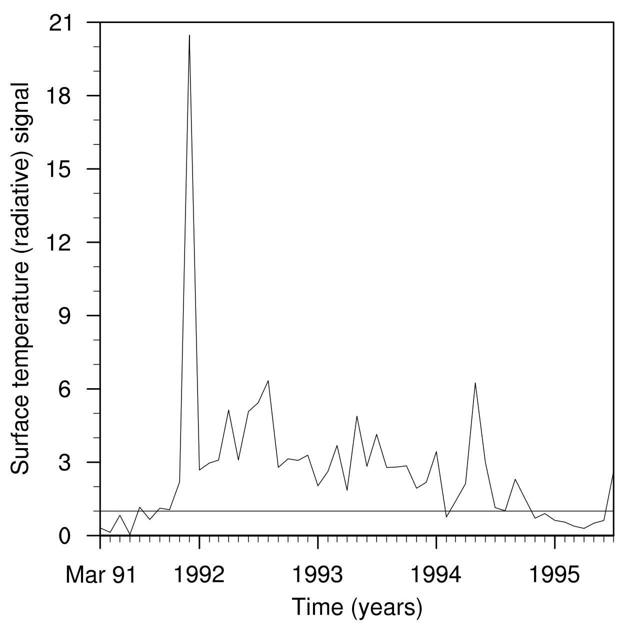

Figure 4-14. Model radiative surface temperature signal to noise ratio from March 1991 to July 1995.

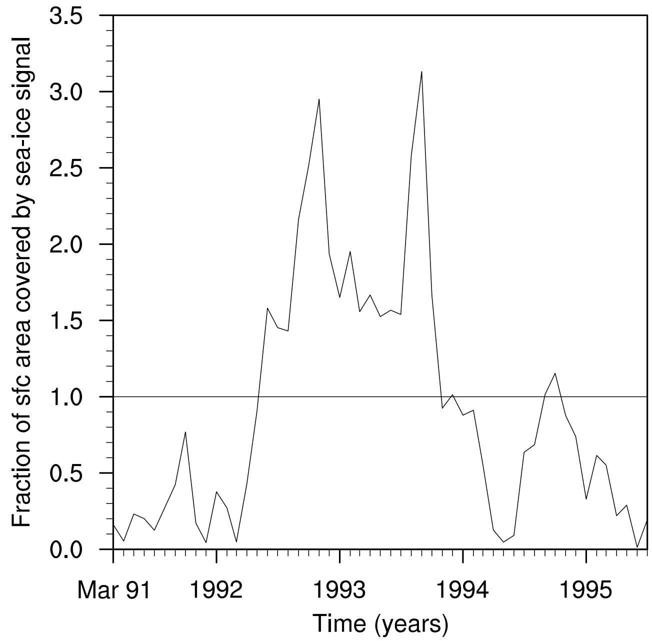

Figure 4-15. Model sea ice area fraction signal to noise ratio from March 1991 to July 1995. The increase in sea ice compared to the control ensemble is reflected in the signal, which peaks in Northern Hemisphere winter 1993 and 1994.

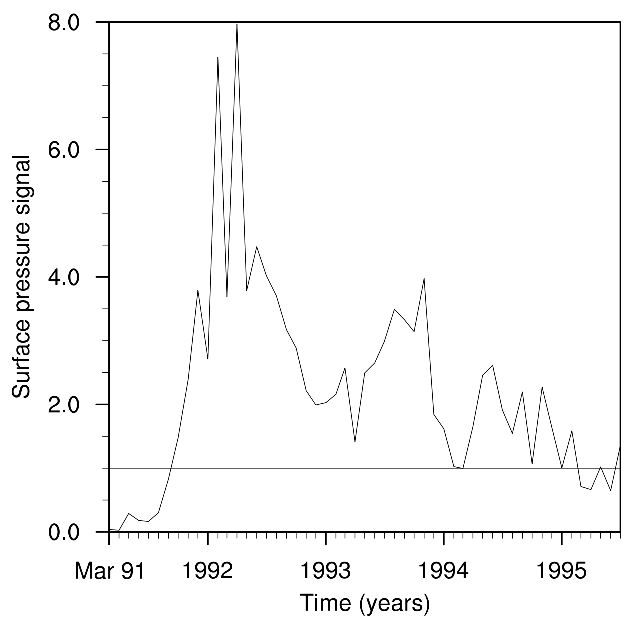

Figure 4-16. Model surface pressure signal to noise ratio from March 1991 to July 1995.

The snow cover and snow depth variables in BTRANS show an increase following the eruption (Figure 4-17 and Figure 4-18), but there is no increase in the snowfall rate variable (not shown). This coincides with the cooler surface air temperatures and larger proportion of diffuse sunlight after the eruption. This implies that the snow does not accumulate due to increased precipitation, but rather due to decreased melting from a greater fraction of diffuse sunlight and cooler surface temperatures. A predictable decrease in runoff, particularly rural runoff, seen in Figure 4-19, in the months after the eruption agrees with this conclusion. Later, the runoff continues to vary inversely with the snow cover, with its signal to noise ratio reaching a second maximum as the runoff increases from the melt of accumulated snow. As conditions return to normal, the snow cover signal drops to within the control noise. The regions most influenced by this process are shown in Figure 4-20. The response occurs mostly in mountainous or high and low latitude areas.

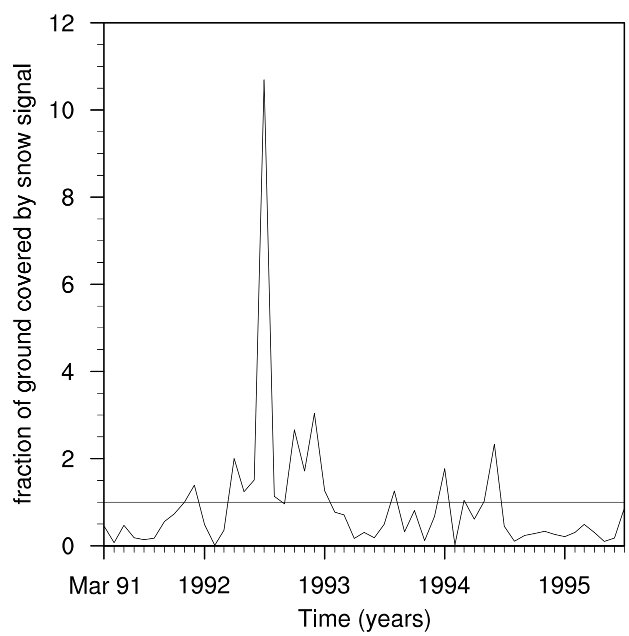

Figure 4-17. Signal to noise ratio over time for fraction of ground covered by snow. The fraction increases in 1992, especially in the cooler-than-normal summer.

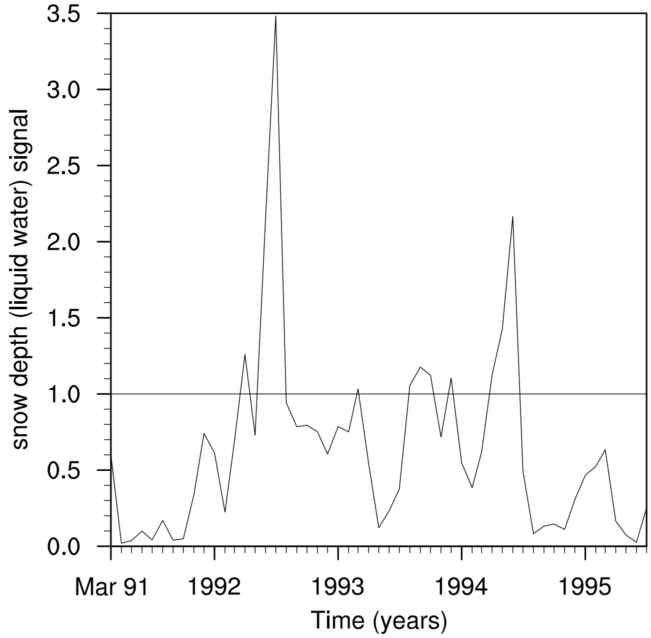

Figure 4-18. Signal to noise ratio over time for snow depth. The snow depth increases in the forced ensemble in summer 1992, and decreases in early summer 1994.

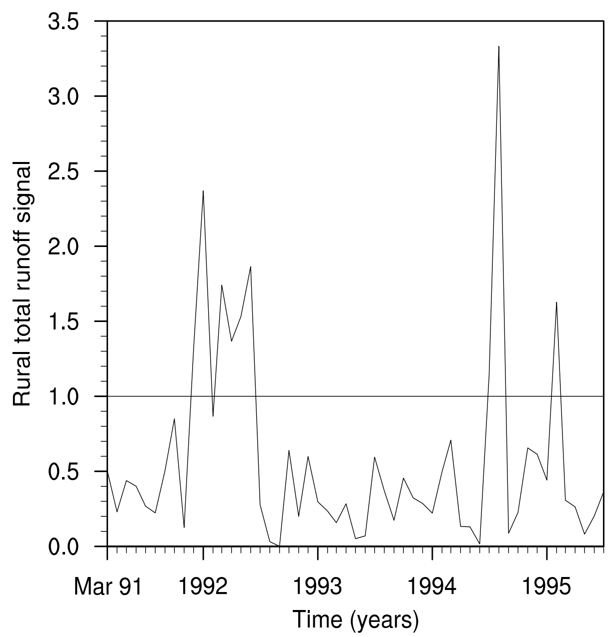

Figure 4-19. Signal to noise ratio over time for rural total runoff. The runoff decreases in winter 1991 through spring 1992, and increases sharply for July 1994.

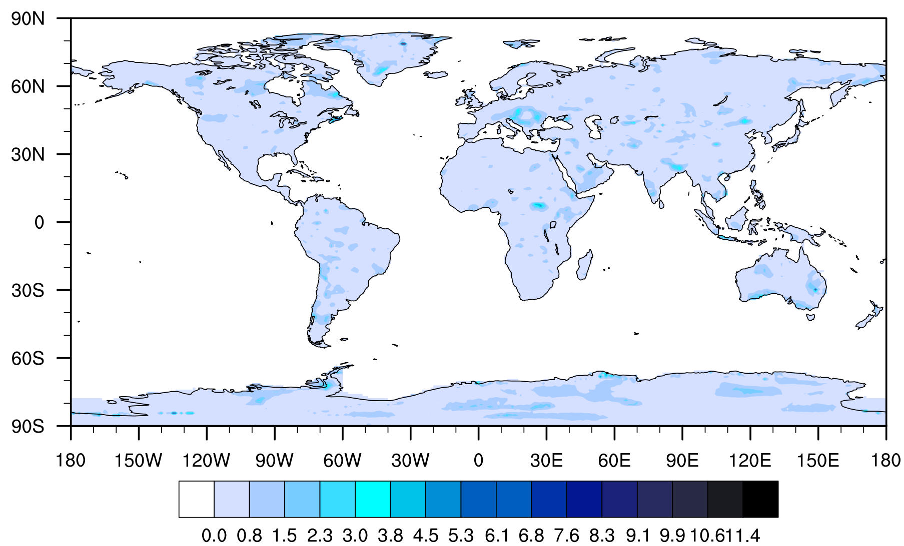

Figure 4-20. Total runoff signal to noise ratio time average spatial pattern.

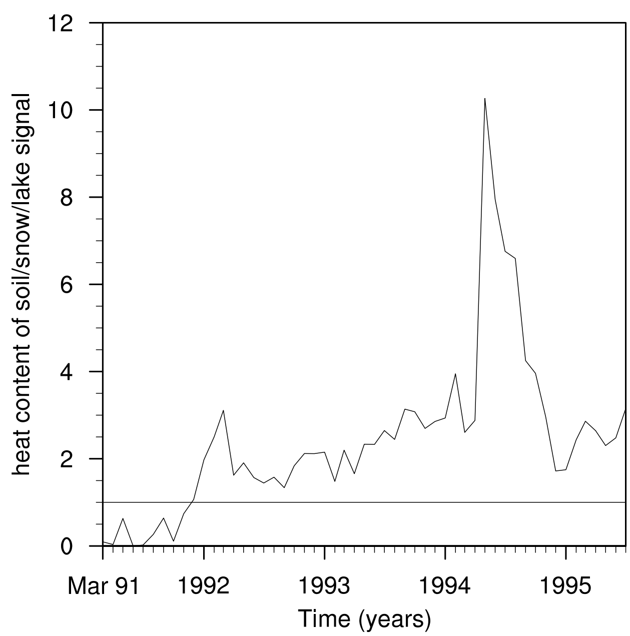

Figure 4-21. Model heat content signal to noise ratio over time for soil, snow, and lake. The signal strengthens after 1992 until reaching a peak in August 1994. The signal remains above two standard deviations of the control ensemble at the end of the simulation.

The volcanic aerosols block light and heat from reaching the ground, creating a loss of heat content in the land model relative to the unperturbed scenarios. The difference relative to the heat content in the model without the eruption builds over time, with most of the grid cell heat content loss in soil, snow, and lakes, shown in Figure 4-21. The signal becomes especially significant in the middle of 1994, when the control ensemble standard deviation narrows about the mean for a few months. The signal to noise ratio duration above three standard deviations for the heat content in soil, snow, and lakes is 7 months.

The responses of the volatile organic compounds monoterpene and isoprene to volcanic aerosols in the model are shown in Figure 4-22 and Figure 4-23. Wilton et al. (2011) predict changes in isoprene emissions from vegetation following Pinatubo-like changes in radiation in a theoretical model. This response is found to be predictable in CESM for the active ocean model configuration. Since the carbon-nitrogen cycle is not active in the simulation, this is an effect of changes in surface temperature and radiation. Both compounds decrease in concentration following the eruption. Examination of the overall volatile organic compound flux shows the spatial pattern of the predictability (Figure 4-24). The decrease in VOC flux occurs predominantly in the tropics, especially over northern South America and the Congo. The types of vegetation in those regions may be more susceptible to temperature changes.

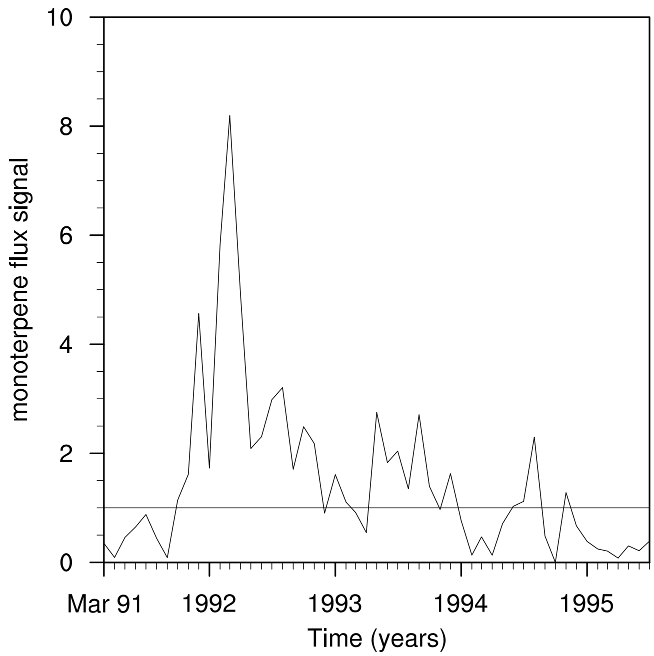

Figure 4-22. Model monoterpene flux signal to noise ratio over time. The response to the eruption is short-lived but prominent, peaking in Northern Hemisphere spring 1992 at eight times the noise.

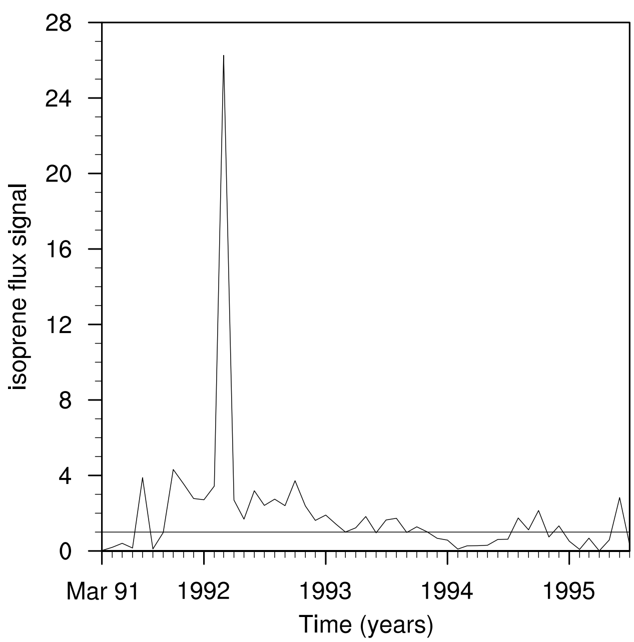

Figure 4-23. Model isoprene flux signal to noise ratio over time. The signal peaks sharply in March 1992 and remains above two times the noise through the rest of the year.

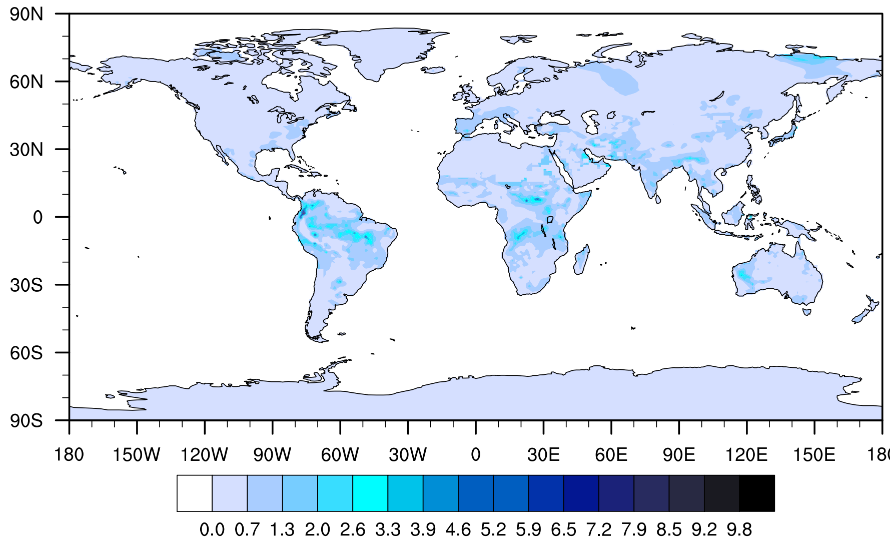

Figure 4-24. Total volatile organic compound flux signal to noise ratio spatial pattern averaged over time.

4.6 Conclusion

Predictability signals for atmospheric variables in the fully coupled Community Earth System Model with T85 atmospheric and 1^{o} land, ocean, and sea ice resolution are evaluated in response to the eruption of Mount Pinatubo. Comparisons with a previous study (Gaddis, Drake et al. 2013) using CESM with the same resolution but with data ocean and sea ice are made. The systematic framework for predictability signal ranking set up in the previous work allows for the discovery of new predictability signals and confirmation of known ones.

Absolute responses to forcing and the duration of stratospheric responses are similar for both model configurations. However, the predictability differs between configurations: additional predictability signals may be measured with an active ocean model. The previous configuration made the control and forced ensembles very similar near the land and ocean surface, so that predictability is underestimated at those points.

Expected tropospheric signals that were not predictable with the atmosphere-land model become significantly predictable with the active ocean configuration. The fully coupled simulations show significant tropospheric and surface signals, including surface pressure and sea ice responses. Additionally, cloud and hydrology related variables show significant responses. The stratospheric temperature, pressure, and zonal wind responses are as expected.

The stratospheric relative and specific humidity responses in the model are attributed to tropical tropopause water vapor flux, rather than injection by the volcanic eruption. This is reinforced by the spatial and temporal pattern of the signal to noise ratio in both specific humidity and tropopause temperature. This response is confirmed to be a predictable and long-lasting result of the eruption, as previously noted in the data ocean configuration (Gaddis, Drake et al. 2013).

Land variable predictability was also analyzed for the fully coupled simulations. Isoprene, monoterpene, and other volatile organic compounds generate a short-lived signal in the model that may be used to further analyze biogeochemical interactions in Earth system models. For the next large volcanic eruption, observational studies of these compounds should be a focus. A possible source of decadal predictability for the land surface is the soil, snow, and lake heat content, which contains a long-lived response. The predictability signals of the variables indicate that snow depth and extent increase in response to cooler surface temperatures in the forced simulations, with runoff decreasing initially and increasing with snow melt a few years later. Attribution studies should be performed to confirm this relationship.

For the fully coupled model, the standard deviation of variables in the forced ensemble is lower than the unforced. The data ocean configuration did not show a trend in standard deviation for the atmospheric variables between the ensembles with and without volcanic forcing. The change in standard deviation in the active ocean configuration implies that the response to the volcanic aerosols in the model is similar regardless of the initial model state, and that the response to the eruption dominates the natural variability. The climate state of unforced systems is more uncertain; forced systems are more predictable since they must respond to the forcing. This reinforces that signal to noise ratio measurements of predictability should use the unforced variability as the measure of the noise in the system. This way the signal to noise ratio measures if a response is predictably different from the ensemble of possible natural states of the system.

Acknowledgements: Gaddis is funded by the Institute for a Secure and Sustainable Environment at the University of Tennessee, Knoxville. Evans is funded through the U.S. Dept. of Energy Office of Biological and Environmental Research (BER) project #3ERKPE746, "Ultra High Resolution Global Climate Simulation to Explore and Quantify Predictive Skill for Climate Means, Variability and Extremes." An award of computer time was provided by the Innovative and Novel Computational Impact on Theory and Experiment (INCITE) program. This research used resources of the Oak Ridge Leadership Computing Facility located in the Oak Ridge National Laboratory, which is supported by the Office of Science of the Department of Energy under Contract DE-AC05-00OR22725.

Chapter 5

PAPER 3: EFFECT OF MODEL RESOLUTION ON ATMOSPHERE RESPONSE TO THE ERUPTION OF MOUNT PINATUBO

A version of this chapter will be submitted to Journal of Climate:

Abigail L. Gaddis, Katherine J. Evans, John B. Drake. “Effect of Model Resolution on Atmosphere Response to the Eruption of Mount Pinatubo.” *Journal of Climate* (2013) in prep.

Drake contributed to concepts and provided direction. Evans made long-term simulations with volcanic aerosols and provided expertise in configuration of experimental high resolution simulations on the Titan supercomputer. Gaddis developed hypotheses, created simulations without the volcano, examined results, and wrote the paper.

5.1 Abstract

Regional patterns of response to forcing are important for policymakers in addressing climate change and mitigation strategies such as geoengineering aerosol forcings. Volcanic eruptions provide a test bed for climate modeling, revealing model representation of dynamical responses to forcing. In this study, the Mount Pinatubo eruption is simulated at very high resolution (T341, ~1/3^{o}) using the Community Earth System Model. The predictability of responses to the eruption are calculated and compared with previous studies of the same model at lower resolution for two configurations. All three configurations are compared with observations to evaluate model skill. The Northern Hemisphere winter warming response to the eruption improves in spatial distribution and strength at higher resolution. Stratospheric humidity increases predictably in all three model configurations, with spatial analysis showing the that response is centered over the tropical tropopause.

5.2 Introduction

Communicating regional and decadal effects of climate change is a key motivation for climate modeling. In addition to improving the accuracy of the model, increasing resolution allows models to more accurately depict regional climate. This is important for making climate change impacts relevant to policymakers and stakeholders.

Increasing resolution in climate models improves simulations in several ways. First, resolving sub-grid scale processes allows physics to replace parameterizations. Synoptic weather systems, tropical instability waves, and cloud microphysics are examples of phenomena parameterized in global climate models due to resolution limitations (Stowasser, Hamilton et al. 2006; Hurrell, Meehl et al. 2009). The best solution is to resolve the dynamics of these processes explicitly by decreasing the grid cell size of the model. As with any numerical method, increasing resolution also increases discretization accuracy in climate modeling. Further, many climate processes involve interactions between dynamics on different spatial and temporal scales. Improvements to sub-scale processes with higher resolution are expected to improve the dynamical representation of larger-scale processes (Hurrell et al. 2009).

Previous studies have quantified improvements to climate models with increasing horizontal resolution. The representation of moisture-related variables improves with smaller simulation mesh step size. A study of precipitation over the United States using the CCM3 model found incremental improvements to the representation of precipitation, from both a seasonal mean and a daily statistics standpoint, as resolution increased (Iorio 2004). Similarly, Collier and Zhang find that a finer horizontal mesh yields a more accurate representation of tropospheric moisture convection, although they note that even at their higher resolution it is still relatively poorly simulated (Collier 2007). Increasing the veracity of orographic features can effect weather and climate, for instance, shifting the polar jet poleward to a more realistic location (Pope and Stratton 2002). Boville noted that eddy fluxes, kinetic energies, and winds improved at higher resolution (Boville 1991). The representation of atmospheric rivers is also enhanced in a high-resolution climate model ensemble (Jiang and Deng 2011).

The Mount Pinatubo eruption and resulting atmospheric responses are often used as a test bed for models, since the eruption provided a global perturbation to the radiation budget (Lacis, Hansen et al. 1992; Robock 2000). Stratospheric warming and tropospheric cooling in response to volcanic sulfate aerosols created further secondary atmospheric dynamic effects (McCormick, Thomason et al. 1995). Since the eruption occurred June 15, 1991, there are many observational records to compare with model output.

Some recent studies have highlighted common global climate model shortcomings in simulations of the Pinatubo eruption. A multimodel ensemble (CMIP5) study showed that global climate models fail to capture the dynamical response in Northern Hemisphere winters, including the positive phase of the North Atlantic Oscillation and the resulting winter warming (Driscoll, Bozzo et al. 2012). It has been proposed that this is a result of a model polar vortex that is unrealistically strong, resisting perturbation from the volcano (Stenchikov 2006). Further, the models tend to overestimate the tropospheric cooling (Driscoll, Bozzo et al. 2012). Global climate models are inaccurate in reproducing volcanic effects on Asian monsoon, and this may be due to general model difficulties with precipitation, e.g. (Stephens, L'Ecuyer et al. 2010; Timmreck 2012).

However, the CMIP5 study uses models with horizontal resolutions of about 1^{o} or lower (Driscoll, Bozzo et al. 2012). Given the relationship between horizontal resolution and many variables that are not well simulated for the eruption, this study performs higher resolution ($\sim 1/4^{o}$) simulations of the Mount Pinatubo eruption. Slight parameterization changes to the default model physics are made to take advantage of the higher resolution. The radiative forcing caused by the eruption of Mount Pinatubo is used as a test bed for the Community Earth System Model. Higher resolution simulations are compared to lower resolution simulations to evaluate the role of resolution in predictability. To determine predictive skill gains, model responses are compared with observations. Spatial analysis of anomalies and predictability are performed to identify regions of predictability and compare spatial distribution of response to volcanic forcing.

5.3 Methodology

5.3.1 Data

The Community Earth System Model (CESM) is a coupled Earth system global climate model (Gent, Danabasoglu et al. 2011). CESM version 1 was used for the simulations with a configuration of active land and atmosphere models, and data ocean and sea ice models. Results from two lower resolution model configurations are compared with a higher resolution configuration. The F component set consists of an active atmosphere, active land model, data ocean, and prescribed sea ice. The B configuration is comprised of all active land, sea ice, land ice, ocean, and atmosphere fully coupled models.

Specifically, the atmospheric model used for all simulations is the Community Atmosphere Model version 4 with both an Eulerian spectral T85 and T341 grid. These resolutions correspond to approximately 1.4^{o} and 0.3^{o}. The physics and vertical resolution is the same for both horizontal resolutions, except for modifications to parameterizations to accommodate high resolution. The land model is the Community Land Model version 4 (CAM4) on a 0.9^{o} latitude by 1.25^{o} longitude spaced grid. For the F simulations, the data ocean uses sea surface temperature climatology from the Hadley Centre on a 1^{o} grid (Rayner, Brohan et al. 2006), and the sea ice component is active, but ice extent is prescribed, matching the configuration and settings used in Evans et al (2013). In contrast, the B configuration is a fully coupled with all active components, including the POP2 ocean model, CICE sea ice model, and the stub land ice model SGLC. The carbon cycle and active chemistry are inactive in all configurations.

Inputs of volcanic aerosols to CAM4 consist of a dataset of monthly mean masses in kg/m^3 on a meridional and vertical grid based on Ammann et al (Ammann 2003). The aerosols are included as a single species composed of 75% sulfuric acid and 25% water. The data assumes the aerosols have a log normal size distribution and average effective radius of .426 μm. The CAM4 contains the direct and semi-direct aerosol effects, but does not include the first or second indirect effect.

Hindcasts of climate from 1975-2005 are simulated with historical sea surface temperature observations. Possible climate states of the system are created by slightly perturbing the initial conditions. Initial atmospheric temperature values are randomly perturbed by a small amount to create a total of five thirty-year ensemble members. These simulations include inputs of observed levels of volcanic aerosols. A control ensemble without volcanic forcing was created by setting the volcanic aerosol input to zero in five branch simulations after May 1991. All simulations were performed on the Titan supercomputer at Oak Ridge National Laboratory.

A positive El Niño phase immediately preceded the Mount Pinatubo eruption, complicating the attribution of responses to the eruption (Robock 2000). To determine the response to the eruption, the effects of ENSO must be differentiated from the volcanic forcing. In this model configuration, the data sea surface temperatures force the El Niño-Southern Oscillation conditions to be the same for all ensemble members in both the forced and unforced ensembles. Therefore, in signal to noise ratio calculations, the sole response measured is to the Mount Pinatubo eruption forcing of the atmosphere.

Additionally, to evaluate model skill, comparisons to observations are performed with certain model variables. Two reanalysis datasets are used for assessment: the ECMWF 40-year reanalysis data, known as ERA-40 (Uppala 2005), and the joint product from the National Centers for Environmental Prediction (NCEP) and the National Center for Atmospheric Research (NCAR), or NCEP reanalysis (Kalnay 1996).

5.3.2 Analysis methods

Predictability studies often use ensembles of forced and unforced model states to distinguish internal climate variability from a deterministic response or pattern (Hansen, Sato et al. 1997; Boer 2004; Van den Dool 2006; Von Storch 2008; Boer 2009). One measurement of this predictability is the signal to noise ratio, or, SNR (Von Storch 2008; Boer 2009; Meehl, Goddard et al. 2009). For this study, the definition of the signal to noise ratio chosen is the difference of the forced and unforced ensemble means divided by the noise. The noise is measured as the standard deviation of the ensemble about its ensemble mean. The ensemble standard deviation chosen to represent the noise is from the ensemble with Pinatubo aerosols removed, since it indicates the unforced variability between possible system states.

Observations are compared with the ensemble average values of certain variables. Climatological anomalies for each variable in space and time are calculated. The global average SNR is calculated using the latitudinally weighted global average of the ensemble average for each variable. The signal to noise ratio is also calculated at each grid point to create a map of predictability. The empirical orthogonal functions of the anomalies are also taken to confirm these spatial patterns and trace their evolution over time. Atmospheric signal to noise ratio and signal duration from two configurations in previous works are compared with the results from the new model configuration.

Three model configurations are compared with observations: an atmosphere-land configuration at T85 and T341 resolutions, and a fully coupled atmosphere-ocean-land-sea ice configuration at T85 resolution. The two ensembles of simulations for each configuration provide a variety of states of the system in both forced and unforced modes. In this way, anomalies due to variation within the system can be differentiated from predictable responses to the eruption. The signal to noise ratio quantifies the predictable differences between the forced and unforced ensembles statistically. Regions of higher predictability are located through mapping the signal to noise ratio and the empirical orthogonal functions. The predictable responses of the system are compared for the three configurations to determine the effect of resolution on predictability, as well as to predict the results of a higher resolution fully coupled model. The responses are compared to observed quantities to show accuracy improvements from higher resolution.

5.4 Results

Global surface temperatures cooled on average in response to the radiative forcing of Mount Pinatubo. This cooling is reflected in the global ensemble averages and standard deviations of the three model configurations. These are plotted along with reanalysis data in Figure 5-1. The T85 B fully coupled ensemble performed most poorly at replicating the temporal response. The response occurs earlier than in the SST-forced F configurations at either resolution, and the response is too strong. However, this is likely because ENSO was allowed to vary in the B ensemble, while in the reanalysis data and F configurations, a positive El Niño phase began before the eruption. The response of the B component set is not modulated by ENSO, on average. All three of the model anomalies return to zero more quickly than the reanalysis data. This implies that the duration of predictability signals related to surface temperature is probably underestimated by the model.

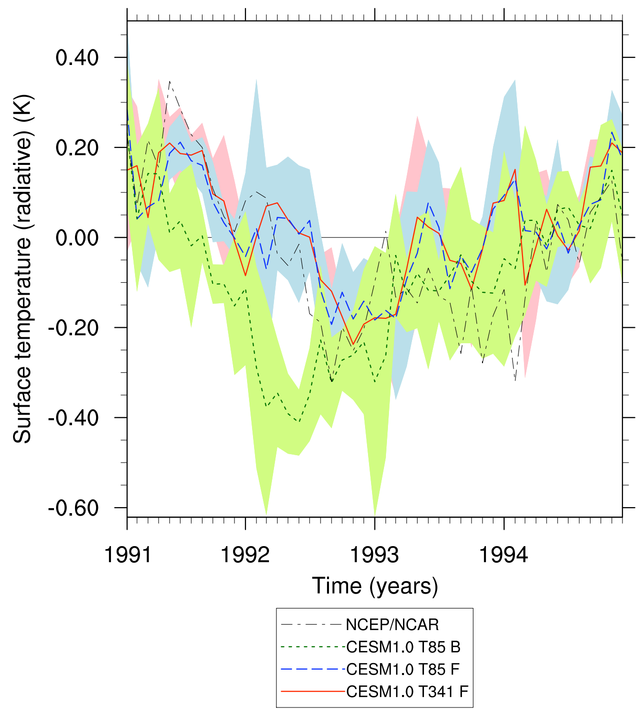

Figure 5-1. Comparison of global average surface temperature anomaly observations and CESM simulations at T85 and T341 resolution for the F configuration, and T85 for the fully coupled configuration. Colored lines are ensemble averages and shading is standard deviation of the ensemble about the average. NCEP/NCAR 2m air temperature is the black observation line.

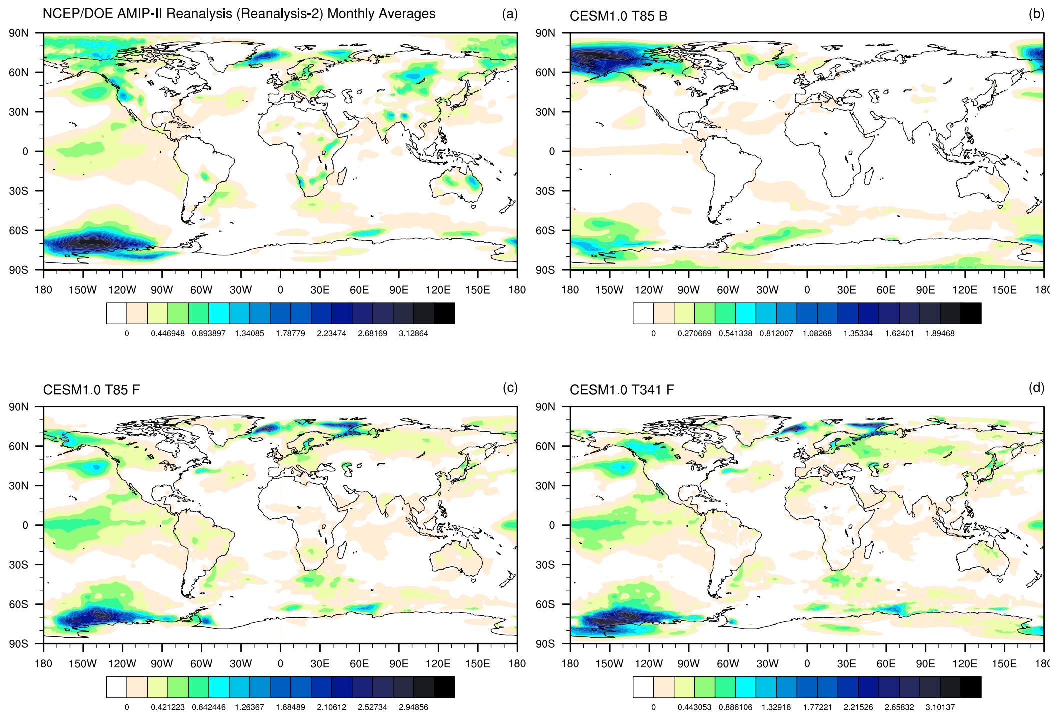

Figure 5-2. Average surface temperature anomaly from climatology, averaged over June 1991 - February 1994. (a) NCEP/NCAR Reanalysis, (b) T85 B configuration, (c) T85 F configuration, and (d) T341 F configuration.

Additionally, northern hemisphere winter warming is one of the most prominent dynamical processes to occur following the eruption (Timmreck 2012). The response is a byproduct of a positive North Atlantic Oscillation phase due to a perturbed polar vortex (Stenchikov 2006). A multimodel ensemble study including a similar version of this model, CCSM4, noted that the spatial distribution of the Northern Hemisphere winter warming is not well reproduced in the models (Driscoll, Bozzo et al. 2012). The highest resolution CESM ensemble captures the spatial pattern of the response after the eruption more accurately than the lower resolution of the same configuration, shown in Figure 5-2.

Between the two simulations with the same resolution, even though the F configuration is forced by data sea surface temperatures, the B configuration spatial response is more similar to the reanalysis data. For T85 F relative to the two other ensembles, continental reactions are missing, the 70S response is too weak, and the response over Alaska is too widespread and predominant. Overall, the maximum anomaly reached is about 1.9K while the reanalysis value of 3.1K is closest to the T341 ensemble anomaly.

Figure 5-3 shows the winter response averaged over the first winter after the eruption, December 1991, January 1992, and February 1992. Here the advantages of the fully coupled model and of the higher resolution are again revealed through the South African and Australian warming responses as well as better simulation of the European and North Asian winter warming signal. The maximum reanalysis anomaly corresponds more closely to the T85B and T341 simulations, with the T341 being closest. The improvement of the winter warming over Eurasia is notable, since has been described previously as a shortcoming of the CCSM model (Stenchikov 2006).

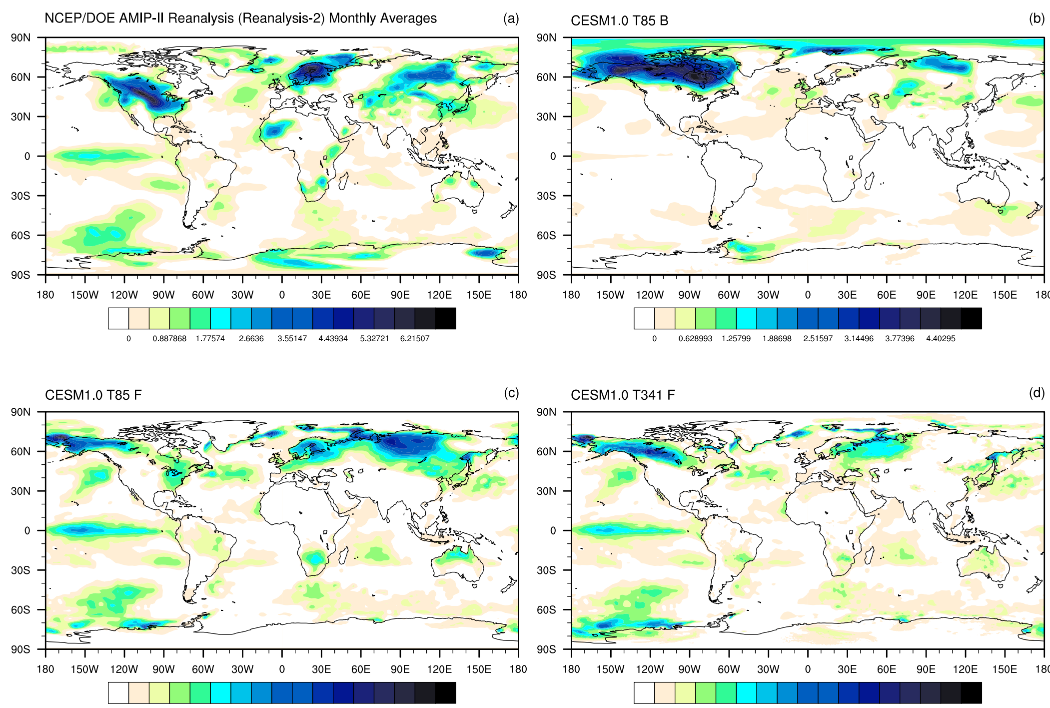

Figure 5-3. Winter average surface temperature anomaly from climatology, averaged over DJF winter 1991-92. (a) NCEP/NCAR Reanalysis, (b) T85 B configuration, (c) T85 F configuration, and (d) T341 F configuration.

Precipitation is known to be inaccurate in climate models; it is too frequent, not intense enough, and especially erroneous over the tropics (Dai 2006; Stephens, L'Ecuyer et al. 2010). Further, precipitation has been found to be sensitive to horizontal resolution

(Collier 2007). The spatial and global average characteristics of precipitation in the model are compared.

As shown in Figure 5-5, the stratospheric specific humidity responses to the eruption are found to be predictable. The high-resolution ensemble confirms that the tropopause warms predictably following the eruption, especially over the tropics (Figure 5-4). Upwelling water vapor then crosses the cold zone rather than freezing out. This results in a large relative humidity anomaly over the tropics, shown with EOF1 at 70mb (Figure 5-6). This pattern contains over 80% of the variance in the variable, and appears temporally correlated with the radiative forcing. This agrees with previous studies (Gaddis, Drake et al. 2013; Gaddis, Evans et al. 2013) attributing the anomaly to the increased tropopause flux mechanism.

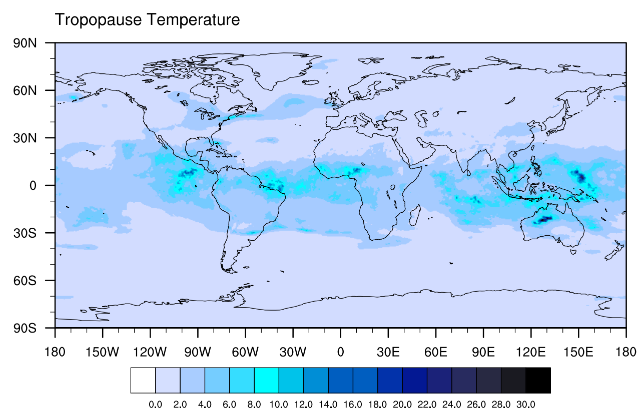

Figure 5-4. Tropopause temperature signal to noise ratio spatial average, June 1991-January 1994. The response is highly predictable over the tropics.

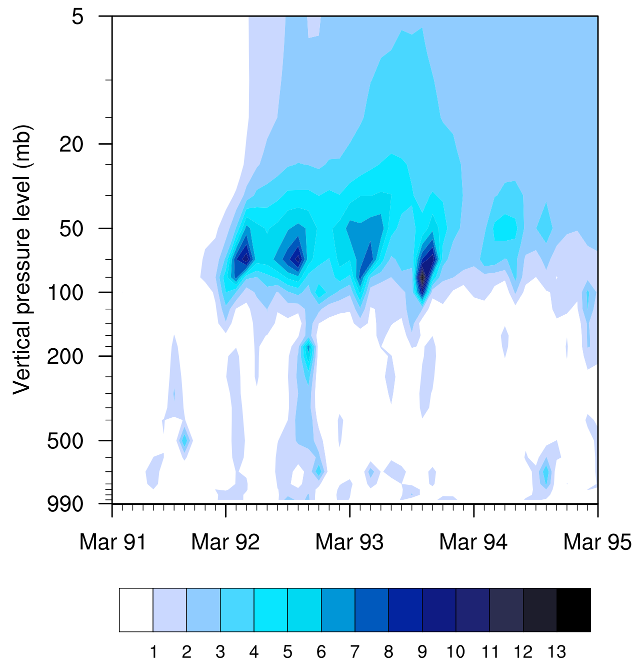

Figure 5-5. T341 signal to noise ratio of specific humidity. The ensemble difference reaches up to 13 times the noise in the control ensemble and remains significant for the remainder of the simulation.

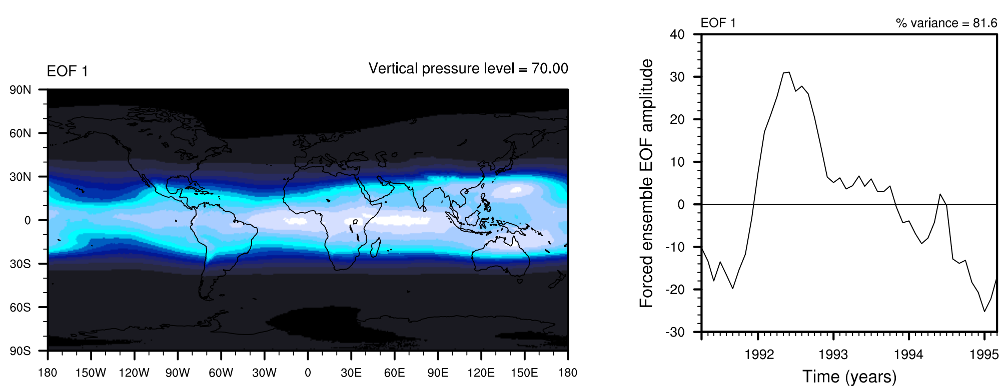

Figure 5-6. Relative humidity EOF1 and PC1 at 70mb, approximately the tropopause, over the tropics. The mode comprises 81.6% of the total variance, and its spatial pattern is centered strongly over the tropics. The temporal pattern of EOF1 is correlated to the eruption.

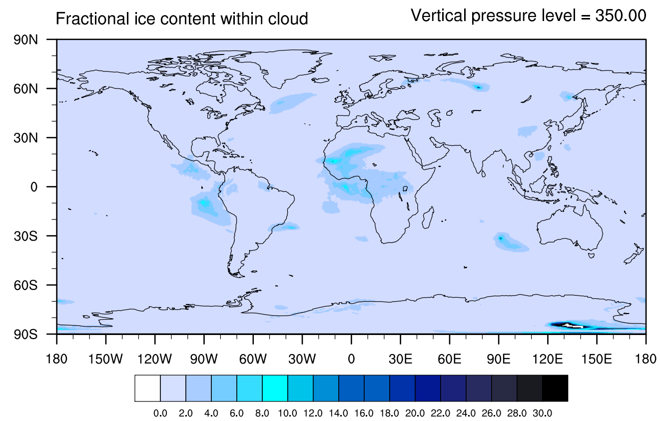

Figure 5-7. Fractional ice content within clouds signal to noise ratio spatial map at 350mb. Signal values above 30 were set to 30 to clarify the distribution of the response.

Various cloud ice related variables responded to the eruption predictably. Few clouds propagate higher in the atmosphere, especially into the stratosphere. Anomalies at these high levels are exaggerated by the lack of data points, see the Appendix I table of maximum signals by level for cloud-related variables ICLDIWP, ICIMR, CLDICE and FICE, for example. The 350mb FICE signal of Figure 5-7 shows the global map of its response to forcing. The signal appears mostly over western Africa and off the west coast of South America. It last for two months with a global average maximum of about three times the noise, although the spatial distribution shows that the local predictability can be very high.

The zonal wind is found to respond predictably in the high resolution ensemble, as in the other two configurations. Figure 5-8 shows the zonal mean of the zonal wind signal to noise ratio. The winter 1991 response to the eruption is strongest, strengthening the northern hemisphere polar night jet. The southern hemisphere polar night jet is also increased in June of 1992, and then again in the northern hemisphere in winter 1993. This confirms observations as well as previous modeling studies. Further signal to noise ratios by level in the atmosphere and signal durations for all significantly predictable model variables are reported in the Appendix (Table A-3, Table A-4, and Table A-5).

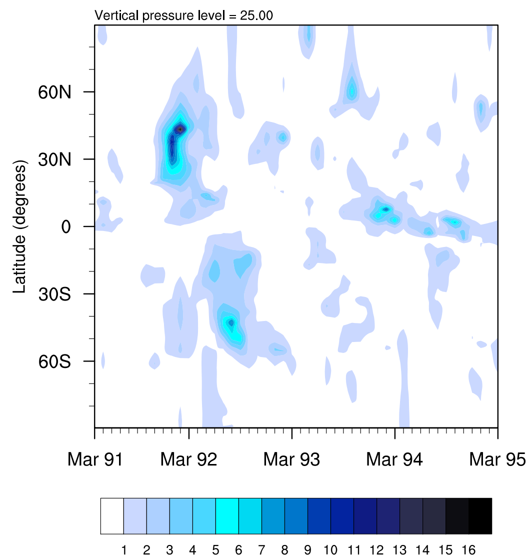

Figure 5-8. T341 signal to noise ratio spatial map of zonal wind at 25mb vertical pressure level.

5.5 Conclusion

Model variables with higher resolution show improvement in spatial distribution and strength of responses relative to observations. Notable improvements are made to the spatial distribution of winter warming following the eruption with high resolution. The spatial distribution of the predictability of the winter warming signal cannot be evaluated in this model configuration due to sea surface temperature ocean boundary conditions. A possible explanation for the increase in realism of the surface temperature is that finer representation of orography, known to shift polar jets, adds a greater realism to the polar vortex.

Investigation of the zonal wind shows that a polar night jet effect is again recorded in response to the eruption. Cloud ice content also responds predictably to the eruption. The statistical significance of these results at high levels in the stratosphere is debatable due to the small number of data points there, mostly over the poles. The specific humidity in the stratosphere also increases due to the eruption, as seen in previous works. The mechanism is likely increased tropopause water vapor flux due to warming.

The findings of this study motivate continuation of the pursuit of both high resolution and complex process modeling for climate and highlight the continued need for computing power. Given the improvements from both higher resolution and fully coupled configurations, a fully coupled ensemble at high resolution should capture the spatial distribution and duration of the response more accurately. Additionally, without the boundary conditions of sea surface temperatures, it would allow the further quantification of predictability for troposphere and hydrology signals in the model.

Acknowledgements: Gaddis is funded by the Institute for a Secure and Sustainable Environment at the University of Tennessee, Knoxville. Evans is funded through the U.S. Dept. of Energy Office of Biological and Environmental Research (BER) project #3ERKPE746, "Ultra High Resolution Global Climate Simulation to Explore and Quantify Predictive Skill for Climate Means, Variability and Extremes." An award of computer time was provided by the Innovative and Novel Computational Impact on Theory and Experiment (INCITE) program. This research used resources of the Oak Ridge Leadership Computing Facility located in the Oak Ridge National Laboratory, which is supported by the Office of Science of the Department of Energy under Contract DE-AC05-00OR22725.

Chapter 6

CONCLUSION

In this work, the predictability and skill of various model variables are analyzed for three global climate model configurations. Forced and unforced ensembles of simulations allow responses to the volcanic forcing to be separated from internal climate variability. Predictability is measured using a unitless signal to noise ratio, and responses are examined spatially as well as temporally.

The first hypothesis of this study is that ranking the measured predictability allows for comparison of signals to find the most responsive and long-lived signals. Previously studied responses to the eruption were replicated in the model. The stratosphere warmed more than the troposphere cooled, as observed, and the tropical tropopause also warmed. The temperature changes resulted in changes to geopotential height. Consequently, temperature and pressure gradient changes led to zonal wind amplification. The oscillating polar night jet response between hemispheres is predictable in all model configurations.

The response of stratospheric specific humidity to the eruption has not previously been shown to be predictable, and the mechanism for water vapor entry into the stratosphere is debated (Timmreck 2012). The stratospheric water vapor increase is shown to be predictable in this work in all model configurations. The aridity of the stratosphere lengthens the time of significance of this response, so that it may be used as a long term predictability signal. This work supports the tropical tropopause flux mechanism for water vapor increase, because the tropopause is shown to be anomalously warm following the eruption. Additionally, the specific humidity anomaly at the tropopause is centered over tropics. Furthermore, in this simulation, no water vapor is injected into the stratosphere by the eruption.

Volatile organic compounds also react to the radiative forcing from the volcanic aerosols in the model. An observational response of isoprene in 1991 is recorded, but this effect had not been previously modeled. It is shown to be a predictable response to the eruption in CESM. Additionally, monoterpene decreases predictably also in response to the radiative forcing. This is expected because they are related to plant stress, which is lessened by the cooler surface temperatures following the eruption. However, these results were obtained without an active carbon-nitrogen cycle in the model. This temperature-related response may be mitigated by more complete biogeochemical treatment in the model.

A relationship between temperature and snow depth and extent is uncovered by this methodology. The cooler temperatures lead to higher snow depths and wider extents than the previous decadal average. Additionally, a runoff response appears inversely related to the snow depth and extent variables. When snow builds up due to cooler temperatures, runoff is lower than average. After a few years, temperatures resume normal behavior, and snow melts off, increasing runoff. These responses are predictable, but a statistical attribution study would make the relationships between these variables more clear.

The second hypothesis is that forcing would change the variability of the ensembles. This is supported in the fully coupled configuration: the standard deviation of the control ensemble is larger than that of the forced ensemble. This implies that the forcing constrains the possible paths in phase space, so that the values are more deterministic than those in the control. For both of the F configuration ensemble sets, the difference between the control and forced variability is smaller overall and less consistent in sign. This is likely due to the constraint imposed on the response by the data sea surface temperatures in that configuration. The data ocean acts as a forcing boundary condition on both the control and forced ensembles. This limits the available responses of the system.

Third, it is hypothesized that the volcanic eruption affects the El Niño – Southern Oscillation. This conclusion is not upheld by the simulation results. The active ocean configuration is the only one of the three configurations in which this hypothesis may be tested, and no statistically significant response to the eruption was found, although the first EOF of the sea surface temperature appeared to contain ENSO and the eruption. This could be due to the small sample size (5) of different ENSO states available, since certain states might respond to the eruption while others do not. A recent study found that only volcanic forcings larger than that of Mount Pinatubo begin to show an effect on the

ENSO state by increasing the likelihood of a positive phase (Emile-Geay, Seager et al. 2008).

Finally, the resolution is hypothesized to improve the overall predictability of variables as well as more precisely identifying regions of predictability. However, the global average predictability signal to noise ratios that are significant in T85 and T341 resolutions are similar. This is probably partly due to the configuration of the high-resolution simulations. The data sea surface temperature ocean acts as a boundary condition on the model, forcing the control ensemble into a response pattern similar to the ensemble with volcanic aerosols near the ocean and land surface. Because of this, predictability signals are not distinguishable for many variables. Some of these variables might show an increase in global average predictability. However, for variables such as temperature and pressure, the responses in T341 F are very similar to those in T85 F.

While the predictability signals in T341 F and T85 F are similar, the skill of the model in reproducing observations improves. The spatial representation of the Northern Hemisphere winter warming notably becomes more realistic in certain known problem areas such as Eurasia. The maximum responses in both the high resolution and fully coupled configurations are both more similar to the observations than the T85 F simulations.

In future studies, the utility of a fully coupled model in predictability studies cannot be overemphasized. The boundary condition of data sea surface temperatures obscures certain differences between control and forced ensembles. Variables especially effected include tropospheric and surface variables such as surface temperature and hydrological variables such as precipitation. Additionally, this configuration modifies the variability of both the control and forced ensembles. These are key properties of predictability calculations. However, absolute responses are closer to observations, and the predictability of stratospheric variables may still be calculated. The sea ice also responded to the eruption when it was not prescribed.

In general, for predictability studies searching for novel decadal responses, the more active modules and represented processes in the model, the better. An active carbon-nitrogen cycle in the land model would aid the search for decadal predictability in land variables. Stratospheric aerosols perturb more than just the radiative forcing; they also provide sites for heterogeneous chemical reactions. Carbon monoxide, methane, and ozone are all known to respond to the sulfuric volcanic aerosols (Dlugokencky, Dutton et al. 1996; Rozanov, Schlesinger et al. 2002; McFarlane 2008). Active chemistry in the model would allow the study of the predictability of these effects and their interaction with large-scale feedbacks. The response of cloud ice to volcanic aerosols is debated in the literature (Robock 2000). It appears to induce a predictable response in upper atmospheric levels in all model configurations of this study. A cloud-resolving model could determine if these are true responses to the eruption or anomalies due to the few clouds at high levels. Additionally, this work could be expanded to further explore regional predictability with high-resolution simulations using variable mesh size capabilities in new spectral element dynamic modules of the atmospheric model.

Both the high resolution and fully coupled models show skill improvements. This implies that a high-resolution fully coupled set of simulations could generate further accuracy gains. Continued funding for flagship computation facilities is necessary to improve model accuracy. The findings of this study motivate the continued drive to higher model resolutions and increased model complexity.

LIST OF REFERENCES

Ammann, C. M., Meehl, Gerald A., Washington, Warren M., and Zender, Charles S. (2003). "A monthly and latitudinally varying volcanic forcing dataset in simulations of 20th century climate." Geophysical Research Letters **30**(12).

Bender, F. A. M., A. M. L. Ekman, et al. (2010). "Response to the eruption of Mount Pinatubo in relation to climate sensitivity in the CMIP3 models." Climate Dynamics **35**(5): 875-886.

Boer, G. J. (2004). "Long time-scale potential predictability in an ensemble of coupled climate models." Climate Dynamics **23**(1): 29-44.

Boer, G. J. (2009). "Changes in Interannual Variability and Decadal Potential Predictability under Global Warming." Journal of Climate **22**(11): 3098-3109.

Boer, G. J., M. Stowasser, et al. (2007). "Inferring climate sensitivity from volcanic events." Climate Dynamics **28**(5): 481-502.

Boer, G. J. and B. Yu (2003). "Climate sensitivity and climate state." Climate Dynamics **21**(2): 167-176.

Boer, G. J. and B. Yu (2003). "Climate sensitivity and response." Climate Dynamics **20**(4): 415-429.

Borzelli, G. (1999). "Empirical Orthogonal Function Analysis of SST Image Series: A Physical Interpretation." Journal of Atmospheric and Oceanic Technology **16**: 682-690.

Boville, B. A. (1991). "SENSITIVITY OF SIMULATED CLIMATE TO MODEL RESOLUTION." Journal of Climate **4**(5): 469-485.

Brasseur, G. and C. Granier (1992). "MOUNT-PINATUBO AEROSOLS, CHLOROFLUOROCARBONS, AND OZONE DEPLETION." Science **257**(5074): 1239-1242.

Bretherton, C. S. (1992). "An Intercomparison of Methods for Finding Coupled Patterns in Climate Data." Journal of Climate **5**: 541-560.

Brovkin, V., S. J. Lorenz, et al. (2010). "Sensitivity of a coupled climate-carbon cycle model to large volcanic eruptions during the last millennium." Tellus Series B-Chemical and Physical Meteorology **62**(5): 674-681.

Caron, L. P., C. G. Jones, et al. (2011). "Impact of resolution and downscaling technique in simulating recent Atlantic tropical cylone activity." Climate Dynamics **37**(5-6): 869-892.

Church, J. A., N. J. White, et al. (2005). "Significant decadal-scale impact of volcanic eruptions on sea level and ocean heat content." Nature **438**(7064): 74-77.

Collier, C. a. Z., G. (2007). "Effects of increased horizontal resolution on simulation of the north american monsoon in the NCAR CAM3." Journal of Climate **20**: 1843-1861.

Considine, D. B., J. E. Rosenfield, et al. (2001). "An interactive model study of the influence of the Mount Pinatubo aerosol on stratospheric methane and water trends." Journal of Geophysical Research-Atmospheres **106**(D21): 27711-27727.

Dai, A. (2006). "Precipitation characteristics in eighteen coupled climate models." Journal of Climate **19**(18): 4605-4630.

DelSole, T. and M. K. Tippett (2007). "Predictability: Recent insights from information theory." Reviews of Geophysics **45**(4).

Deremble, B., F. D'Andrea, et al. (2009). "Fixed points, stable manifolds, weather regimes, and their predictability." Chaos **19**(4): 20.

Dlugokencky, E. J., E. G. Dutton, et al. (1996). "Changes in CH4 and CO growth rates after the eruption of Mt Pinatubo and their link with changes in tropical tropospheric UV flux." Geophysical Research Letters **23**(20): 2761-2764.

Driscoll, S., A. Bozzo, et al. (2012). "Coupled Model Intercomparison Project 5 (CMIP5) simulations of climate following volcanic eruptions." Journal of Geophysical Research-Atmospheres **117**: 25.

Emile-Geay, J., R. Seager, et al. (2008). "Volcanoes and ENSO over the past millennium." Journal of Climate **21**(13): 3134-3148.

Evans, K. J., J. M. McClean, M. Maltrud, S. Mahajan, M. Branstetter, J. M. and D. C. B. J. J. H. Caron, and R. B. Neale (2013). "A spectral transform dynamical core option within the atmospheric component of the Community Earth System Model." Journal of Climate **In prep.**

Farrell, B. F. and P. J. Ioannou (2005). "Distributed forcing of forecast and assimilation error systems." Journal of the Atmospheric Sciences **62**(2): 460-475.

Flato, G. M. (2011). "Earth system models: an overview." Wiley Interdisciplinary Reviews-Climate Change **2**(6): 783-800.

Frumkin, A. and V. Misra (2013). "Predictability of dry season reforecasts over the tropical and the sub-tropical South American region." International Journal of Climatology **33**(5): 1237-1247.

Gaddis, A. L., J. B. Drake, et al. (2013). "Evaluating Climate Predictability Signals in Response to Forcing: Mount Pinatubo as a Case Study." In Prep.

Gaddis, A. L., K. J. Evans, et al. (2013). "Effect of Active Ocean Model on Land and Atmosphere Predictability in Response to the Eruption of Mount Pinatubo." In Prep.

Gent, P. R., G. Danabasoglu, et al. (2011). "The Community Climate System Model Version 4." Journal of Climate **24**(19): 4973-4991.

Gillett, N. P., A. J. Weaver, et al. (2004). "Detection of volcanic influence on global precipitation." Geophysical Research Letters **31**(12): 4.

Grainger, R. G., A. Lambert, et al. (1993). "INFRARED-ABSORPTION BY VOLCANIC STRATOSPHERIC AEROSOLS OBSERVED BY ISAMS." Geophysical Research Letters **20**(12): 1283-1286.

Gu, G. J. and R. F. Adler (2011). "Precipitation and Temperature Variations on the Interannual Time Scale: Assessing the Impact of ENSO and Volcanic Eruptions." Journal of Climate **24**(9): 2258-2270.

Gu, L. H., D. D. Baldocchi, et al. (2003). "Response of a deciduous forest to the Mount Pinatubo eruption: Enhanced photosynthesis." Science **299**(5615): 2035-2038.

Hannachi, A. (2007). "Empirical Orthogonal Functions and Related Techniques in Atmospheric Science: A review." International Journal of Climatology **27**: 1119-1152.

Hansen, J., A. Lacis, et al. (1992). "POTENTIAL CLIMATE IMPACT OF MOUNT-PINATUBO ERUPTION." Geophysical Research Letters **19**(2): 215-218.

Hansen, J., M. Sato, et al. (1997). "Radiative forcing and climate response." Journal of Geophysical Research-Atmospheres **102**(D6): 6831-6864.

Hansen, J., M. Sato, et al. (1997). "Forcings and chaos in interannual to decadal climate change." Journal of Geophysical Research-Atmospheres **102**(D22): 25679-25720.

Hurrell, J., G. A. Meehl, et al. (2009). "A unified modeling approach to climate system prediction." Bulletin of the American Meteorological Society **90**(12): 1819-1832.

Iorio, J. P., Duffy, P.B., Govindasamy B., Thompson, S.L., Khairoutdinov, M., Randall, D. (2004). "Effects of model resolution and subgrid-scale physics on the simulation of precipitation in the continental United States." Climate Dynamics **23**: 243-258.

IPCC (2007). Climate Change 2007: The Physical Science Basis. . Contribution of Working Group I to the Fourth Assessment Report of the Intergovernmental Panel on Climate Change. S. Solomon, D. Qin, M. Manning, Z. Chen, M. Marquis, K.B. Averyt, M. Tignor and H.L. Miller. Cambridge, UK and New York, NY, USA., Cambridge University Press**:** 996.

Jiang, T. Y. and Y. Deng (2011). "Downstream modulation of North Pacific atmospheric river activity by East Asian cold surges." Geophysical Research Letters **38**: 6.

Jones, C. D. and P. M. Cox (2001). "Modeling the volcanic signal in the atmospheric CO2 record." Global Biogeochemical Cycles **15**(2): 453-465.

Joshi, M. M. and G. S. Jones (2009). "The climatic effects of the direct injection of water vapour into the stratosphere by large volcanic eruptions." Atmospheric Chemistry and Physics **9**(16): 6109-6118.

Kalnay, E., et al. (1996). The NCEP/NCAR 40-year reanalysis project. Bull. Amer. Meteor. Soc. **77:** 437-470.

Kiehl, J. T. and K. E. Trenberth (1997). "Earth's annual global mean energy budget." Bulletin of the American Meteorological Society **78**(2): 197-208.

Koenigk, T., C. K. Beatty, et al. (2012). "Potential decadal predictability and its sensitivity to sea ice albedo parameterization in a global coupled model." Climate Dynamics **38**(11-12): 2389-2408.

Lacis, A., J. Hansen, et al. (1992). "CLIMATE FORCING BY STRATOSPHERIC AEROSOLS." Geophysical Research Letters **19**(15): 1607-1610.

Latif, M., D. Anderson, et al. (1998). "A review of the predictability and prediction of ENSO." Journal of Geophysical Research-Oceans **103**(C7): 14375-14393.

Lorenz, E. N. (1963). "Deterministic nonperiodic flow." Journal of the Atmospheric Sciences **20**(2): 130-141.

Lorenz, E. N. (1969). "Atmospheric predictability as revealed by naturally occurring analogues." Journal of the Atmospheric Sciences **26**(4): 636-&.

Lucarini, V. and S. Sarno (2011). "A statistical mechanical approach for the computation of the climatic response to general forcings." Nonlinear Processes in Geophysics **18**(1): 7-28.

Lucht, W., I. C. Prentice, et al. (2002). "Climatic control of the high-latitude vegetation greening trend and Pinatubo effect." Science **296**(5573): 1687-1689.

McClean, J. L., D.C. Bader, F.O. Bryant, M.E. Maltrud, J. M. Dennis, A. A. Mirin, P.W. Jones, Y.Y. Kim, D. P. Ivanova, M. Vertenstein, J. S. Boyle, R. L. Jacob, N.

Norton, A. Craig, P. H. Worley (2011). "A Prototype two-decade fully-coupled fine-resolution CCSM simulation." Ocean Modelling **39**: 10-30.

McCormick, M. P., L. W. Thomason, et al. (1995). "Atmospheric effects of the Mt-Pinatubo eruption." Nature **373**(6513): 399-404.

McFarlane, N. (2008). "Connections between stratospheric ozone and climate: Radiative forcing, climate variability, and change." Atmosphere-Ocean **46**(1): 139-158.

Meehl, G. A., L. Goddard, et al. (2009). "Decadal Prediction: Can It Be Skillful?" Bulletin of the American Meteorological Society **90**(10): 1467-+.

Mote, P. W., K. H. Rosenlof, et al. (1996). "An atmospheric tape recorder: The imprint of tropical tropopause temperatures on stratospheric water vapor." Journal of Geophysical Research-Atmospheres **101**(D2): 3989-4006.

Pope, V. D. and R. A. Stratton (2002). "The processes governing horizontal resolution sensitivity in a climate model." Climate Dynamics **19**(3-4): 211-236.

Rampino, M. R. and S. Self (1984). "SULFUR-RICH VOLCANIC-ERUPTIONS AND STRATOSPHERIC AEROSOLS." Nature **310**(5979): 677-679.

Rampino, M. R. and S. Self (1992). "VOLCANIC WINTER AND ACCELERATED GLACIATION FOLLOWING THE TOBA SUPER-ERUPTION." Nature **359**(6390): 50-52.

Randel, W. J., F. Wu, et al. (2004). "Interannual changes of stratospheric water vapor and correlations with tropical tropopause temperatures." Journal of the Atmospheric Sciences **61**(17): 2133-2148.

Rayner, N. A., P. Brohan, et al. (2006). "Improved analyses of changes and uncertainties in sea surface temperature measured in situ sice the mid-nineteenth century: The HadSST2 dataset." Journal of Climate **19**(3): 446-469.

Robock, A. (2000). "Volcanic eruptions and climate." Reviews of Geophysics **38**(2): 191-219.

Robock, A. and J. P. Mao (1992). "Winter warming from large volcanic eruptions." Geophysical Research Letters **19**(24): 2405-2408.

Roderick, M. L., G. D. Farquhar, et al. (2001). "On the direct effect of clouds and atmospheric particles on the productivity and structure of vegetation." Oecologia **129**(1): 21-30.

Rozanov, E. V., M. E. Schlesinger, et al. (2002). "Climate/chemistry effects of the Pinatubo volcanic eruption simulated by the UIUC stratosphere/troposphere GCM with interactive photochemistry." Journal of Geophysical Research-Atmospheres **107**(D21).

Santer, B. D., T. M. L. Wigley, et al. (2001). "Accounting for the effects of volcanoes and ENSO in comparisons of modeled and observed temperature trends." Journal of Geophysical Research-Atmospheres **106**(D22): 28033-28059.

Sato, M., J. E. Hansen, et al. (1993). "STRATOSPHERIC AEROSOL OPTICAL DEPTHS, 1850-1990." Journal of Geophysical Research-Atmospheres **98**(D12): 22987-22994.

Schlink, U. (2009). "Non-negative Matrix Factorization for the identification of patterns of atmospheric pressure and geopotential for the Northern Hemisphere." International Journal of Climatology **30**: 909-925.

Schneider, D. P., C. M. Ammann, et al. (2009). "Climate response to large, high-latitude and low-latitude volcanic eruptions in the Community Climate System Model." Journal of Geophysical Research-Atmospheres **114**.

Sellers, P. J., R. E. Dickinson, et al. (1997). "Modeling the exchanges of energy, water, and carbon between continents and the atmosphere." Science **275**(5299): 502-509.

Simmons, A. J., P. D. Jones, et al. (2004). "Comparison of trends and low-frequency variability in CRU, ERA-40, and NCEP/NCAR analyses of surface air temperature." Journal of Geophysical Research-Atmospheres **109**(D24): 18.

Stenchikov, G. (2006). "Arctic Oscillation response to volcanic eruptions in the IPCC AR4 climate models." Journal of Geophysical Research **111**.

Stenchikov, G., T. L. Delworth, et al. (2009). "Volcanic signals in oceans." Journal of Geophysical Research-Atmospheres **114**: 13.

Stenke, A. and V. Grewe (2005). "Simulation of stratospheric water vapor trends: impact on stratospheric ozone chemistry." Atmospheric Chemistry and Physics **5**: 1257-1272.

Stephens, G. L., T. L'Ecuyer, et al. (2010). "Dreary state of precipitation in global models." Journal of Geophysical Research-Atmospheres **115**: 13.

Stowasser, M., K. Hamilton, et al. (2006). "Local and global climate feedbacks in models with differing climate sensitivities." Journal of Climate **19**(2): 193-209.

Taylor, K. E., R. J. Stouffer, et al. (2012). "AN OVERVIEW OF CMIP5 AND THE EXPERIMENT DESIGN." Bulletin of the American Meteorological Society **93**(4): 485-498.

Telford, P. J., J. Lathiere, et al. (2010). "Effects of climate-induced changes in isoprene emissions after the eruption of Mount Pinatubo." Atmospheric Chemistry and Physics **10**(15): 7117-7125.

Timmreck, C. (2012). "Modeling the climatic effects of large explosive volcanic eruptions." Wiley Interdisciplinary Reviews-Climate Change **3**(6): 545-564.

Trenberth, K. E. and A. Dai (2007). "Effects of Mount Pinatubo volcanic eruption on the hydrological cycle as an analog of geoengineering." Geophysical Research Letters **34**(15): 5.

Uppala, S., et al. (2005). The ERA-40 re-analysis. Quart. J. R. Meteorol. Soc. **131:** 2961-3012.

Van den Dool, H. M. (2006). "Seasonal-to-Decadal Predictability and Prediction of North American Climate -- The Atlantic Influence." Journal of Climate -- Special Selection **19**: 6005-6024.

Varghese, S., B. Langmann, et al. (2011). "Effect of horizontal resolution on meteorology and air-quality prediction with a regional scale model." Atmospheric Research **101**(3): 574-594.

Von Storch, J.-S. (2008). "Toward Climate Prediction: Interannual Potential Predictability due to an Increase in CO2 Concentration as Diagnosed from an Ensemble of AO GCM Integrations." Journal of Climate **21**: 4607-4628.

Wang, T., O. H. Ottera, et al. (2012). "The response of the North Pacific Decadal Variability to strong tropical volcanic eruptions." Climate Dynamics **39**(12): 2917-2936.

Wilton, D. J., C. N. Hewitt, et al. (2011). "Simulated effects of changes in direct and diffuse radiation on canopy scale isoprene emissions from vegetation following volcanic eruptions." Atmospheric Chemistry and Physics **11**(22): 11723-11731.

Zanchettin, D., C. Timmreck, et al. (2012). "Bi-decadal variability excited in the coupled ocean-atmosphere system by strong tropical volcanic eruptions." Climate Dynamics **39**(1-2): 419-444.

APPENDICES

Appendix A DATA TABLES

Table A-1. Maximum value of signal to noise ratio for T85 B atmospheric variables with a vertical component by vertical level

Signal and Standard Deviation Information

Variable	Max Signal	Duration	STD BTRANS	STD noPin
CLDHGH	3.3	1	0.0043	0.0043
CLDLOW	5.7	1	0.0045	0.0048
CLDTOT	4.8	1	0.0048	0.0046
FLDS	6.9	9	0.82	1
FLDSC	7.9	9	0.8	1
FLNS	9.6	1	0.47	0.52
FLNSC	3.6	1	0.39	0.44
FLNT	9.2	3	0.51	0.56
FLNTC	10	16	0.35	0.4
FLUT	9.1	3	0.51	0.56
FLUTC	10	16	0.35	0.4
FREQZM	8.2	1	0.007	0.0077
FSDS	14	12	0.81	0.73
FSDSC	60	29	0.15	0.19
FSNS	11	12	0.77	0.66
FSNSC	77	22	0.27	0.28
FSNT	15	17	0.69	0.59
FSNTC	75	27	0.25	0.28
FSNTOA	15	17	0.69	0.59
FSNTOAC	75	27	0.25	0.28
FSUTOA	15	17	0.69	0.59
ICEFRAC	3.1	1	0.0013	0.0015
LHFLX	4.6	1	1.3	1.4
LWCF	4.5	3	0.37	0.36
OCNFRAC	3.1	1	0.0013	0.0015
PCONVB	4.8	2	7.8	8.3
PRECL	4.9	1	4.2e-10	4.2e-10
PRECSC	3.6	1	2.3e-11	2.1e-11
PRECSH	4.4	1	8.5e-11	9.8e-11
PS	8	8	2.6	3.1
PSL	3.4	1	4.4	4.2
QFLX	4.6	1	5.1e-07	5.5e-07
QREFHT	12	9	7.9e-05	9.7e-05
SRFRAD	18	16	0.99	1
SST	16	12	0.049	0.067
SWCF	12	10	0.64	0.55
TGCLDIWP	4.6	1	0.29	0.32
TMQ	8	8	0.26	0.32
TREFHT	11	3	0.14	0.16
TREFMNAV	9.5	4	0.14	0.16
TREFMXAV	9.4	7	0.14	0.16
TROP_P	17	5	1.1e+02	1.1e+02
TROP_T	13	6	0.18	0.18
TROP_Z	12	7	52	60
TS	20	6	0.14	0.16
TSMN	7.8	7	0.18	0.2
TSMX	7.3	8	0.14	0.18

Table A-2. Maximum value of signal to noise ratio for T85 B land variables

Signal and Standard Deviation Information

Variable	Max Signal	Duration	STD BTRANS	STD noPin
BIOGENCO	5.2	1	0.47	0.61
EFLX_LH_TOT_R	4.5	0	0.0073	0.0075
ELAI	9	1	0.88	0.97
ERRSEB	5.9	1	0.0016	0.0014
ERRSOI	3.3	0	3.9e-17	3.8e-17
ESAI	7.2	1	1.1e-16	1.1e-16
FCOV	6.4	1	4.6e-12	4.7e-12
FGR12	4.4	0	9.6e-18	9.9e-18
FGR_U	5.1	1	0.0015	0.0015
FIRE	3	0	0.23	0.28
FLDS	5.1	1	0.0041	0.0045
FSA	3.9	0	0.57	0.68
FSA_R	4.6	0	0.31	0.3
FSDS	6.6	1	0.29	0.26
FSDSND	4.1	0	0.34	0.32
FSDSNDLN	6.1	1	0.94	0.89
FSDSNI	3.3	0	1.1	1.2
FSDSVD	3.2	0	1.2	1.4
FSDSVDLN	9.4	3	1.5	1.7
FSDSVI	12	1	1.7	1.9
FSH	3.1	0	0.041	0.05
FSH_NODYNLNDUSE	6.8	1	1.5	1.5
FSNO	3.3	0	0.00073	0.00091
FSR	6.9	1	1.6	1.7
FSRND	7.5	1	1.7	1.8
FSRNDLN	13	8	1	1.1
FSRNI	9	2	3.3	3.5
FSRVD	35	19	0.24	0.25
FSRVDLN	27	12	0.91	0.97
FSRVI	18	10	2.9	3.2
GC_HEAT1	32	18	0.28	0.3
GC_ICE1	5.1	1	0.8	0.95
HC	4.1	0	0.53	0.65
HCSOI	5.1	1	0.8	0.95
ISOPRENE	4.5	0	0.88	1
LAISUN	3.2	0	1.8	1.8
MONOTERP	4.1	0	0.05	0.053
ORVOC	11	1	0.0074	0.0076
OVOC	5.6	1	0.61	0.63
Q2M	8.7	4	0.34	0.38
QBOT	8.2	1	1	1.1
QINTR	26	17	0.11	0.12
SABV	13	2	0.27	0.28
SNOBCMSL	11	1	0.8	0.81
SNOOCMSL	8	4	0.22	0.22
TBOT	12	4	3.8	4.2
TBUILD	6.6	1	1.7	2
TG	3.5	0	1.2	1.5
TG_R	3.7	0	0.02	0.021
TG_U	10	4	3.9	4.3
THBOT	12	4	3.6	4
TREFMNAV	26	1	18	20
TREFMNAV_R	4.1	0	0.0011	0.00099
TREFMNAV_U	17	1	0.0005	0.00046
TREFMXAV	8.2	2	1.2	1.3
TREFMXAV_R	5.2	1	1.6	2
TREFMXAV_U	5.2	1	1.6	2
TSA	3.2	0	56	51
TSA_R	3.3	0	0.02	0.018
TSA_U	7	1	0.00014	0.00016
TSOI_10CM	8.1	1	0.00013	0.00015
TV	4	0	9.8e-07	1.2e-06
VOCFLXT	18	1	1.7e-07	2e-07
ZBOT	3.2	0	5.6e-07	6.4e-07

Table A-3. Maximum value of signal to noise ratio for T341 F atmospheric variables with a vertical component by vertical level

Maximum signal by vertical level

Variable	Pressure level (mb) 5	10	15	25	35	50	70	85	100	120	140	160	180	200	250	300	350	400	500	600	700	800	850	900	950
CLDICE	168	16	14			50	6	2	2	2	3	5	5	5	4	3	3	3	2	3	2	2	2	2	3
CLDLIQ	319	29	9	10	12	8	8	19	25	49	133			7	2	3	3	3	3	2	3	3	3	3	3
CLOUD						6	5	3	3	5	3	4	15	7	2	3	3	3	3	2	4	4	4	2	2
CMFDQ						6	4	2	3	2	2	5	3	3	3	2	3	3	2	3	2	2	5	3	2
CMFDQR							7	3	3	2	4	3	3	4	2	2	3	4	3	3	3	3	5	2	2
CMFDT						2	6	4	5	2	7	3	2	3	2	3	4	3	2	3	2	4	5	2	2
CONCLD						4	3	2	2	2	3	6	4	3	3	6	3	2	2	2	2	3	5	3	2
DCQ	9	9	13	9	6	4	3	2	2	2	3	3	4	4	3	4	4	6	2	3	4	2	3	4	2
DTCOND	9			257	12	2	6	4	4	2	3	3	3	8	2	2	3	3	3	3	5	5	4	2	3
DTH	3	3	3	4	4	8	5	3	3	2	2	3	3	3	2	3	3	2	4	3	4	2	6	2	3
DTV	35	33	46	76	64	81	4	4	3	5	3	5	2	2	3	2	2	4	3	2	3	2	4	4	3
FICE	4	5	9	19	12	22	79	324		12	22	4	5	10	3	3	3	4	3	2	2	1	2	1	1
GCLDLWP	169	16	14			59	6	2	2	2	3	5	5	4	5	3	3	3	2	2	3	3	3	3	3
ICIMR	152	17	14			152	10	3	4	4	13	5	4	3	2	5	3	4	4	4	3	2	3	3	2
ICLDIWP	152	17	14			170	10	3	4	4	12	5	4	3	2	3	2	2	2	5	3	2	2	2	2
ICLDTWP	152	17	14			170	10	3	4	4	12	5	4	3	2	3	3	3	2	4	4	6	4	3	1
ICWMR	319	29	9	10	12	8	8	20	25	49	134			12	2	3	3	4	5	2	7	2	2	2	1
Q	3	3	3	4	5	7	10	13	9	3	3	3	7	6	3	3	2	3	4	2	4	3	2	2	3
QC							7	3	3	2	4	3	2	3	2	2	2	2	4	4	3	3	5	2	3
QRL	8	18	13	49	111	78	11	3	3	2	6	6	6	6	4	4	3	4	3	4	6	2	3	3	2
QRS	26	34	48	126	333		179	32	10	4	6	13	7	12	6	6	6	8	5	16	10	27	9	8	4
RELHUM	3	3	3	5	8	17	7	16	6	2	3	3	4	2	2	2	5	3	7	3	4	3	2	2	2
T	52	32	41	47	104	112	65	11	10	3	4	3	2	3	10	10	6	5	4	4	5	5	4	6	5
U	3	3	4	4	4	3	2	2	3	2	2	2	2	3	2	2	2	2	2	5	5	3	3	3	3
UU	7	6	6	5	4	5	3	2	3	4	3	2	2	2	2	2	2	1	2	2	3	3	3	3	2
V	3	3	4	3	3	4	1	2	4	2	3	3	3	3	4	2	4	3	3	2	2	4	4	3	2
VD01	4	6	5	8	9	5	4	2	3	2	2	3	3	2	5	3	4	3	4	5	2	2	4	2	3
VQ	3	4	5	4	4	3	2	2	5	2	3	3	3	3	3	3	4	5	3	2	2	6	4	3	4
VT	3	3	3	3	2	2	2	2	4	2	3	3	4	3	4	2	4	2	3	2	2	5	4	3	2
VU	2	3	3	2	3	2	2	2	5	3	2	2	2	3	2	2	2	2	2	2	2	2	2	4	4
VV	5	4	4	4	4	2	2	2	2	2	2	3	2	3	3	2	2	2	2	2	2	2	3	3	2
Z3	65	48	41	34	28	16	4	2	3	5	7	8	8	8	7	6	6	6	6	7	8	9	10	8	4

Table A-4. Duration in months of signal to noise ratio for T341 F atmospheric variables with a vertical component by vertical level

Signal duration by vertical level

Variable	Pressure (mb)																									
	5	10	15	25	35	50	70	85	100	120	140	160	180	200	250	300	350	400	500	600	700	800	850	900	950	993
CLDICE	1	1	1	1	1	3	1	0	0	0	0	1	1	1	1	0	0	0	0	0	0	0	0	0	1	0
CLDLIQ	1	1	1	1	1	1	1	1	1	1	2	2	2	2	0	0	0	0	0	0	1	0	1	1	1	0
CLOUD	0	0	0	0	0	1	1	0	1	1	0	1	1	1	0	1	0	1	0	0	1	1	1	0	0	0
CMFDQ	0	0	0	0	0	1	1	0	0	0	0	1	0	0	0	0	0	0	0	0	0	0	1	1	0	0
CMFDQR	0	0	0	0	0	0	2	0	0	0	1	0	1	1	0	0	1	1	0	0	1	1	1	0	0	0
CMFDT	0	0	0	0	0	0	1	1	1	0	2	1	0	1	0	0	1	0	0	0	0	1	1	0	0	0
CONCLD	0	0	0	0	0	1	0	0	0	0	1	1	1	0	1	1	1	0	0	0	0	0	1	1	0	0
DCQ	1	1	1	1	1	1	0	0	0	0	0	0	1	1	1	1	1	1	0	1	1	0	1	1	0	0
DTCOND	1	1	1	1	1	0	1	1	1	0	1	0	1	2	0	0	0	0	1	1	1	1	1	0	0	0
DTH	1	0	1	1	1	1	1	1	1	0	0	0	0	1	0	0	0	0	1	0	1	0	1	0	0	0
DTV	16	25	27	34	32	25	1	1	1	1	0	1	0	0	1	0	0	1	0	0	0	0	1	1	0	0
FICE	3	2	3	2	3	3	8	5	5	3	2	2	1	1	0	2	2	2	1	0	0	0	0	0	0	0
GCLDLWP	1	1	1	1	1	3	1	0	0	0	0	1	1	1	1	1	1	0	0	0	1	1	0	0	1	0
ICIMR	1	1	1	1	1	3	1	0	1	1	1	1	1	0	0	1	0	1	1	1	0	0	0	0	0	0
ICLDIWP	1	1	1	1	1	3	1	0	1	1	1	1	1	0	0	1	0	0	0	1	1	0	0	0	0	0
ICLDTWP	1	1	1	1	1	3	1	0	1	1	1	1	1	0	0	0	0	0	0	1	1	1	1	0	0	0
ICWMR	1	1	1	1	1	1	1	1	1	1	2	2	2	2	0	1	1	1	1	0	1	0	0	0	0	0
Q	0	6	7	13	20	22	16	11	2	1	0	0	1	1	1	0	0	0	1	0	1	1	0	0	0	0
QC	0	0	0	0	0	0	2	0	0	0	1	0	0	1	0	0	0	0	1	1	0	1	1	0	0	0
QRL	8	15	16	24	29	28	6	1	0	0	1	2	2	1	1	1	1	1	0	2	1	0	0	0	0	0
QRS	16	23	23	26	33	41	29	12	3	1	1	3	5	4	3	3	4	5	6	6	7	4	8	5	2	0
RELHUM	1	0	1	2	5	24	12	11	3	0	0	0	1	0	0	0	1	0	1	1	1	1	0	0	0	0
T	10	22	23	26	29	30	26	23	4	0	1	0	0	0	1	2	2	2	2	2	2	1	1	2	1	0
U	0	2	3	2	2	1	0	0	1	0	0	0	0	0	0	0	0	0	0	1	1	1	1	1	0	0
UU	3	3	2	4	4	1	0	0	0	1	0	0	0	0	0	0	0	0	0	0	0	0	1	0	0	0
V	0	0	1	0	0	1	0	0	1	0	0	1	1	1	1	0	1	0	0	0	0	1	1	0	0	0
VD01	8	4	6	8	8	2	2	0	0	0	0	0	0	0	1	1	1	0	1	1	0	0	1	0	1	0
VQ	0	1	1	1	1	0	0	0	1	0	0	0	1	0	0	1	1	1	0	0	0	1	1	0	1	0
VT	0	1	1	0	0	0	0	0	1	0	0	1	1	1	1	0	1	0	0	0	0	1	1	0	0	0
VU	0	0	1	0	1	0	0	0	1	0	0	0	0	0	0	0	0	0	0	0	0	0	0	1	1	0
VV	1	1	2	1	1	0	0	0	0	0	0	1	0	0	0	0	0	0	0	0	0	0	0	0	0	0
Z3	23	23	23	23	23	11	2	0	0	2	2	2	2	2	2	2	2	2	1	1	1	1	1	1	1	0

Table A-5. Maximum value of signal to noise ratio for T341 F atmospheric variables with one level

Signal and Standard Deviation Information

Variable	Max Signal	Duration	STD Pin	STD noPin	STD % diff
CLDMED	7	1	0.0018	0.0019	6.9
FLDS	6.6	1	0.54	0.62	13
FLDSC	3.6	1	0.48	0.55	15
FLNS	7.3	1	0.41	0.46	12
FLNSC	3.3	1	0.32	0.34	6.1
FLNT	7.7	1	0.44	0.5	13
FLNTC	11	6	0.34	0.37	10
FLUT	7.8	1	0.44	0.5	13
FLUTC	10	6	0.34	0.37	10
FSDS	25	15	0.56	0.61	8.8
FSDSC	86	30	0.11	0.11	-1.2
FSNS	21	16	0.52	0.58	12
FSNSC	87	23	0.19	0.22	17
FSNT	22	18	0.45	0.51	13
FSNTC	2.1e+02	23	0.19	0.21	12
FSNTOA	22	18	0.45	0.51	13
FSNTOAC	2.1e+02	23	0.19	0.21	12
FSUTOA	22	18	0.45	0.51	13
LWCF	13	2	0.26	0.26	0.63
ODV_SSLTA	3.3	1	0.00014	0.00016	13
ODV_SSLTC	3	1	9.8e-05	0.00011	14
ODV_VOLC_MMR	2.3e+04	43	7.8e-05	1.5e-05	-81
PRECL	4.1	1	5.1e-10	5.1e-10	-0.4
PRECSH	3.1	1	9.7e-12	9.1e-12	-6.1
QREFHT	4.2	1	4.2e-05	4.4e-05	6.6
RHREFHT	3.7	1	0.25	0.26	2.8
SRFRAD	35	15	0.6	0.72	21
SWCF	7.4	3	0.43	0.48	11
TAUX	4.1	1	0.003	0.003	-0.39
TAUY	3.4	1	0.0016	0.0014	-11
TGCLDLWP	3	1	1.7	1.7	-1.9
TREFHT	3.4	1	0.11	0.14	28
TREFMXAV	3.7	1	0.11	0.14	28
TROP_P	13	7	83	88	5.8
TROP_T	11	7	0.23	0.23	2.7
TROP_Z	19	10	45	47	3.6
U10	4.4	1	0.1	0.096	-5.2

Appendix B VARIABLE NAMES

Table B-1. Model atmospheric variable names and abbreviations

Abbreviation	Full Name
AEROD_v	Total Aerosol Optical Depth in visible band
CLDHGH	Vertically-integrated high cloud
CLDICE	Grid box averaged cloud ice amount
CLDLIQ	Grid box averaged cloud liquid amount
CLDLOW	Vertically-integrated low cloud
CLDMED	Vertically-integrated mid-level cloud
CLDTOT	Vertically-integrated total cloud
CLOUD	Cloud fraction
CMFDQ	QV tendency - shallow convection
CMFDQR	Q tendency - shallow convection rainout
CMFDT	T tendency - shallow convection
CMFMC	Moist shallow convection mass flux
CMFMCDZM	Convection mass flux from ZM deep
CONCLD	Convective cloud cover
DCQ	Q tendency due to moist processes
DTCOND	T tendency - moist processes
DTH	T horizontal diffusive heating
DTV	T vertical diffusion
FICE	Fractional ice content within cloud
FLDS	Downwelling longwave flux at surface
FLDSC	Clearsky downwelling longwave flux at surface
FLNS	Net longwave flux at surface
FLNSC	Clearsky net longwave flux at surface
FLNT	Net longwave flux at top of model
FLNTC	Clearsky net longwave flux at top of model
FLUT	Upwelling longwave flux at top of model
FLUTC	Clearsky upwelling longwave flux at top of model
FREQSH	Fractional occurance of shallow convection
FREQZM	Fractional occurance of ZM convection
FSDS	Downwelling solar flux at surface
FSDSC	Clearsky downwelling solar flux at surface
FSDTOA	Downwelling solar flux at top of atmosphere
FSNS	Net solar flux at surface
FSNSC	Clearsky net solar flux at surface
FSNT	Net solar flux at top of model
FSNTC	Clearsky net solar flux at top of model
FSNTOA	Net solar flux at top of atmosphere
FSNTOAC	Clearsky net solar flux at top of atmosphere

Table B-1. Continued.

Abbreviation	Full Name
FSUTOA	Upwelling solar flux at top of atmosphere
GCLDLWP	Grid-box cloud water path
ICEFRAC	Fraction of sfc area covered by sea-ice
ICIMR	Prognostic in-cloud ice mixing ratio
ICLDIWP	In-cloud ice water path
ICLDTWP	In-cloud cloud total water path (liquid and ice)
ICWMR	Prognostic in-cloud water mixing ratio
LANDFRAC	Fraction of sfc area covered by land
LHFLX	Surface latent heat flux
LWCF	Longwave cloud forcing
OCNFRAC	Fraction of sfc area covered by ocean
OMEGA	Vertical velocity (pressure)
OMEGAT	Vertical heat flux
PBLH	PBL height
PCONVB	convection base pressure
PCONVT	convection top pressure
PHIS	Surface geopotential
PRECC	Convective precipitation rate (liq + ice)
PRECCDZM	Convective precipitation rate from ZM deep
PRECL	Large-scale (stable) precipitation rate (liq + ice)
PRECSC	Convective snow rate (water equivalent)
PRECSH	Shallow Convection precipitation rate
PRECSL	Large-scale (stable) snow rate (water equivalent)
PRECT	Total (convective and large-scale) precipitation rate (liq + ice)
PS	Surface pressure
PSL	Sea level pressure
Q	Specific humidity
QC	Q tendency - shallow convection LW export
QFLX	Surface water flux
QREFHT	Reference height humidity
QRL	Longwave heating rate
QRS	Solar heating rate
RELHUM	Relative humidity
RHREFHT	Reference height relative humidity
SFCLDICE	CLDICE surface flux
SFCLDLIQ	CLDLIQ surface flux
SHFLX	Surface sensible heat flux
SNOWHICE	Water equivalent snow depth
SNOWHLND	Water equivalent snow depth
SOLIN	Solar insolation
SRFRAD	Net radiative flux at surface
SST	sea surface temperature
SWCF	Shortwave cloud forcing
T	Temperature
TAUX	Zonal surface stress

Table B-1. Continued.

Abbreviation	Full Name
TAUY	Meridional surface stress
TGCLDIWP	Total grid-box cloud ice water path
TGCLDLWP	Total grid-box cloud liquid water path
TMQ	Total (vertically integrated) precipitatable water
TREFHT	Reference height temperature
TREFMNAV	Average of TREFHT daily minimum
TREFMXAV	Average of TREFHT daily maximum
TROP_P	Tropopause Pressure
TROP_T	Tropopause Temperature
TROP_Z	Tropopause Height
TS	Surface temperature (radiative)
TSMN	Minimum surface temperature over output period
TSMX	Maximum surface temperature over output period
U	Zonal wind
U10	10m wind speed
UU	Zonal velocity squared
V	Meridional wind
VD01	Vertical diffusion of Q
VQ	Meridional water transport
VT	Meridional heat transport
VU	Meridional flux of zonal momentum
VV	Meridional velocity squared
Z3	Geopotential Height (above sea level)

Table B-2. Model land variable names and abbreviations

Abbreviation	Full Name
FCTR	canopy transpiration
FGEV	ground evaporation
FGR	heat flux into soil/snow including snow melt
FGR12	heat flux between soil layers 1 and 2
FGR_R	Rural heat flux into soil/snow including snow melt
FGR_U	Urban heat flux into soil/snow including snow melt
FIRA	net infrared (longwave) radiation
FIRA_R	Rural net infrared (longwave) radiation
FIRA_U	Urban net infrared (longwave) radiation
FIRE	emitted infrared (longwave) radiation
FLDS	atmospheric longwave radiation
FLUXFM2A	heat flux for rain to snow conversion
FLUXFMLND	heat flux from rain to snow conversion
FPSN	photosynthesis
FSA	absorbed solar radiation
FSAT	fractional area with water table at surface
FSA_R	Rural absorbed solar radiation
FSA_U	Urban absorbed solar radiation
FSDS	atmospheric incident solar radiation
FSDSND	direct nir incident solar radiation
FSDSNDLN	direct nir incident solar radiation at local noon
FSDSNI	diffuse nir incident solar radiation
FSDSVD	direct vis incident solar radiation
FSDSVDLN	direct vis incident solar radiation at local noon
FSDSVI	diffuse vis incident solar radiation
FSH	sensible heat
FSH_G	sensible heat from ground
FSH_NODYNLNDUSE	sensible heat
FSH_R	Rural sensible heat
FSH_U	Urban sensible heat
FSH_V	sensible heat from veg
FSM	snow melt heat flux
FSM_R	Rural snow melt heat flux
FSM_U	Urban snow melt heat flux
FSNO	fraction of ground covered by snow
FSR	reflected solar radiation
FSRND	direct nir reflected solar radiation
FSRNDLN	direct nir reflected solar radiation at local noon
FSRNI	diffuse nir reflected solar radiation
FSRVD	direct vis reflected solar radiation
FSRVDLN	direct vis reflected solar radiation at local noon
FSRVI	diffuse vis reflected solar radiation
GC_HEAT1	initial gridcell total heat content
GC_ICE1	initial gridcell total ice content

Table B-2. Continued.

Abbreviation	Full Name
GC_LIQ1	initial gridcell total liq content
H2OCAN	intercepted water
H2OSNO	snow depth (liquid water)
H2OSNO_TOP	mass of snow in top snow layer
H2OSOI	volumetric soil water
HC	heat content of soil/snow/lake
HCSOI	soil heat content
ISOPRENE	isoprene flux
LAISHA	shaded projected leaf area index
LAISUN	sunlit projected leaf area index
MONOTERP	monoterpene flux
OCDEP	total OC deposition (dry+wet) from atmosphere
ORVOC	other reactive VOC flux
OVOC	other VOC flux
PBOT	atmospheric pressure
PCO2	atmospheric partial pressure of CO2
Q2M	2m specific humidity
QBOT	atmospheric specific humidity
QCHANR	RTM river flow: LIQ
QCHANR_ICE	RTM river flow: ICE
QCHARGE	aquifer recharge rate
QCHOCNR	RTM river discharge into ocean: LIQ
QCHOCNR_ICE	RTM river discharge into ocean: ICE
QDRAI	sub-surface drainage
QDRIP	throughfall
QFLX_ICE_DYNBAL	ice dynamic land cover change conversion runoff flux
QFLX_LIQ_DYNBAL	liq dynamic land cover change conversion runoff flux
QINFL	infiltration
QINTR	interception
QMELT	snow melt
QOVER	surface runoff
QRGWL	surface runoff at glaciers (liquid only)
QRUNOFF	total liquid runoff (does not include QSNWCPICE)
QRUNOFF_NODYNLNDUSE	total liquid runoff (does not include QSNWCPICE)
QRUNOFF_R	Rural total runoff
QRUNOFF_U	Urban total runoff
QSNWCPICE	excess snowfall due to snow capping
QSOIL	ground evaporation
QVEGE	canopy evaporation
QVEGT	canopy transpiration
RAIN	atmospheric rain
RAINATM	atmospheric rain forcing
RAINFM2A	land rain on atm grid
RH2M	2m relative humidity
SABG	solar rad absorbed by ground

Table B-2. Continued.

Abbreviation	Full Name
SABV	solar rad absorbed by veg
SNOBCMCL	mass of BC in snow column
SNOBCMSL	mass of BC in top snow layer
SNODSTMCL	mass of dust in snow column
SNODSTMSL	mass of dust in top snow layer
SNOOCMCL	mass of OC in snow column
SNOOCMSL	mass of OC in top snow layer
SNOW	atmospheric snow
SNOWATM	atmospheric snow forcing
SNOWDP	snow height
SNOWFM2A	land snow on atm grid
SNOWICE	snow ice
SNOWLIQ	snow liquid water
SOILICE	soil ice
SOILLIQ	soil liquid water
SOILWATER_10CM	soil liquid water + ice in top 10cm of soil
TAUX	zonal surface stress
TAUY	meridional surface stress
TBOT	atmospheric air temperature
TBUILD	internal urban building temperature
TG	ground temperature
TG_R	Rural ground temperature
TG_U	Urban ground temperature
THBOT	atmospheric air potential temperature
TLAI	total projected leaf area index
TLAKE	lake temperature
TREFMNAV	daily minimum of average 2-m temperature
TREFMXAV	daily maximum of average 2-m temperature
TSA	2m air temperature
TSAI	total projected stem area index
TSA_R	Rural 2m air temperature
TSA_U	Urban 2m air temperature
TSOI	soil temperature
TSOI_10CM	soil temperature in top 10cm of soil
TV	vegetation temperature
U10	10-m wind
URBAN_AC	urban air conditioning flux
URBAN_HEAT	urban heating flux
VOCFLXT	total VOC flux into atmosphere
VOLR	RTM storage: LIQ
WA	water in the unconfined aquifer
WIND	atmospheric wind velocity magnitude
WT	total water storage (unsaturated soil water + groundwater)
ZBOT	atmospheric reference height
ZWT	water table depth

VITA

Abigail Gaddis was born on October 1, 1984 in Shreveport, Louisiana. She acquired her Bachelor's of Science in Physics from Furman University, where she graduated cum laude in 2007. She then went to the University of Tennessee, Knoxville, receiving a M.S. in Physics in 2009. She pursued her doctoral research at the University of Tennessee in the Civil and Environmental Engineering Department, receiving her PhD in 2013.